Correlations in Particle Production in Nuclear Collisions at LHC Energies

The Henryk Niewodniczański Institute of Nuclear Physics

Polish Academy of Sciences

Iwona Sputowska

June 2016, Krakow

Mojej Rodzinie

Abstract

New data on forward-backward charged particle correlations and multiplicity fluctuations in Pb+Pb collisions at $\sqrt{s_{NN}} = 2.76$ TeV measured by the ALICE detector at CERN are presented. The analysis focuses on the dependence of (a) the correlation coefficient b_{corr}, (b) the intensive quantity ω and (c) the strongly-intensive quantity Σ as a function of (1) the pseudorapidity gap (2) the centrality of the collision and (3) the width of the centrality bin. The considered observables are studied for Pb+Pb data with two different centrality estimators. The centrality selection methods are based on charged particle multiplicity measurement by the ALICE VZERO detector and on determination of energy carried by spectator systems by the Zero Degree Calorimeter.

A strong dependence of the measured magnitude of forward-backward correlation (b_{corr}), and of the size of multiplicity fluctuations (ω), is observed as a function of the applied centrality estimator and as a function of the size of centrality window. A dominant effect on the correlation strength and multiplicity fluctuations from geometrical fluctuations is apparent for wide centrality class windows. This effect decreases significantly with narrowing the size of centrality class bin.

The presented work verifies that the Σ observable exhibits the properties of strongly intensive quantity in terms of Independent Source Model for Pb+Pb collisions at ALICE energies. Thus the usage of the strongly intensive quantity Σ makes measurement independent on "trivial" effects like the number of nucleons participating in the collision and its fluctuations.

The results on centrality selected Pb+Pb collisions (from peripheral to central) are compared to elementary p+p collisions at the same collision energy, showing the role of the system size w.r.t. short-range and long-range correlations present in the process. A comparison of the obtained results to Monte Carlo simulations shows that the detailed nature of the interplay between short-range and long range correlations requires a further effort in phenomenological understanding.

Contents

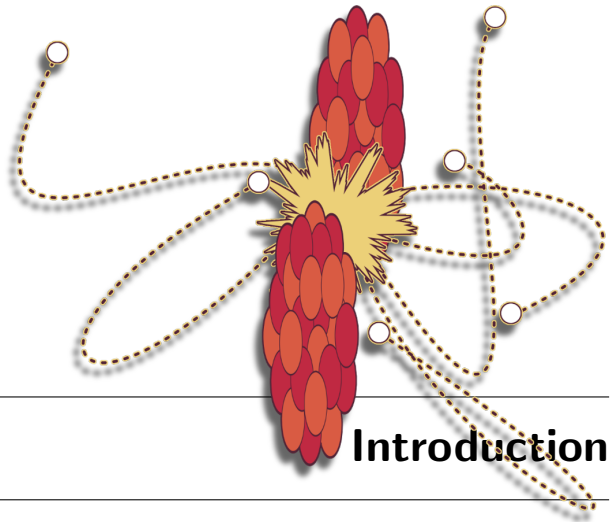

CHAPTER 1

Introduction

1.1 Ultra-relativistic Heavy Ion Collisions

The term **ultra-relativistic heavy ion collisions** refers to collisions of atomic nuclei with large nucleon number (like e.g. Pb, Au) at energy of the order of a few GeV per nucleon or higher. Theoretical predictions suggest that high energy nucleus-nucleus reactions can lead to the formation of an extremely hot and dense state of nuclear matter called Quark-Gluon Plasma (QGP). It is believed that the quark-gluon plasma was the substance filling the early Universe just a few microseconds after the Big Bang; nowadays it might be present in the core of neutron stars. Ultra-relativistic heavy ion collisions become therefore a unique tool in experimental physics to investigate the properties of such extreme states of strongly interacting matter under (more or less) controlled conditions. This brings the opportunity to deepen the knowledge and provide new information on one of the four fundamental forces in nature – **the strong interaction**.

The quantum field theory describing the strong force is called **Quantum Chromodynamics (QCD)**. It is a non-Abelian gauge theory with symmetry group SU(3). QCD postulates that all hadrons (mesons and baryons) are made of fundamental particles: **quarks** and **qluons**. Gluons are Quantum chromodynamic's gauge bosons – the carriers of the strong force. Quarks, which are fermions, interact via exchange of gluons. Both quarks and gluons carry the **charge of strong interaction**, called **color**. From QCD arise two important hypotheses on the properties of nuclear matter: **color confinement** and **asymptotic freedom**. According to the confinement hypothesis, color charged particles cannot be isolated as separate objects [1]. From the perspective of experimental physics this implies that it is impossible to observe free quarks because they are bound in color singlet (color neutral) hadrons. On the other hand, one can speak about asymptotic freedom in QCD, when, for very high energy and short distance reactions, the interaction strength between quarks becomes weak enough for quarks to behave like free particles.

Quantum Chromodynamics is a difficult theory in terms of direct calculations, mainly due to the fact that any attempts to obtain quantitative results outside of the perturbative regime of QCD are difficult if not impossible to perform. Perturbative QCD techniques apply only to processes with large four-momentum transfer, where the strong coupling constant (the determinant of the interaction strength) is small. The fact is that a significant part of heavy ion physics phenomena occurs with small four-momentum transfer (which corresponds to large values of strong coupling). Therefore in the large part, the qualitative and quantitative theoretical description of physical processes in high energy nucleus-nucleus reactions needs to be delivered by a non-perturbative QCD approach,

mostly based on phenomenological models.

There is a diverse set of theoretical frameworks developed to describe various stages of the heavy ion collision. Some of those theoretical approaches include e.g. the theory of Color Glass Condensate, specified for initial pre-collision conditions of exotic nuclear matter in Lorentz contracted nuclei about to collide, the transition from hadronic matter to QGP, "lattice" QCD thermodynamics characterizing static QCD matter, transport theory, relativistic hydrodynamics dedicated to study the QGP equilibrium state, and many others.

It is a prediction of lattice QCD that in heavy ion collisions a phase transition from the hadronic matter to the deconfined phase described by quark and gluon degrees of freedom (the quark-gluon plasma) should occur. According to lattice calculations the temperature and energy density of this hadron-quark transition can be achieved in ultra-relativistic heavy ion collisions.

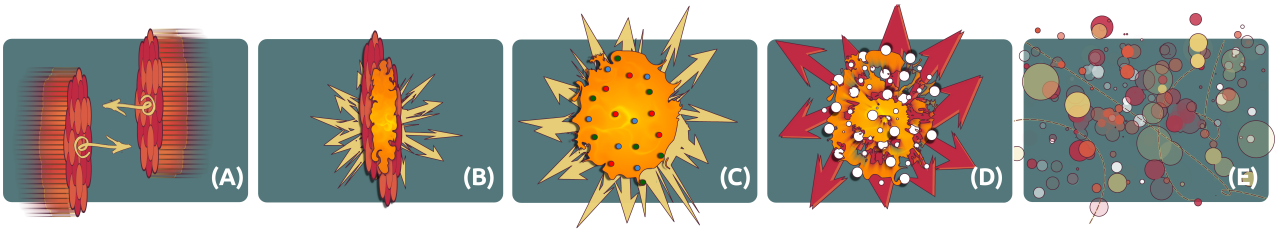

Figure 1.1: The figure shows the main stages of heavy ion collisions. In the picture were distinguished phases such as: the pre-collision state (a) where two Lorentz contracted nuclei are about to collide, the non-equilibrium stage (b), the QGP and equilibrium state (c) which can be described by relativistic hydrodynamics, the hadronization phase (d), the hadronization freeze-out stage (e) during which particle abundances (chemical freeze-out) and their kinematics (kinetic/thermal freeze out) become fixed.

Experimental programs dedicated to studies of nucleus-nucleus collisions in a wide range of nuclear masses and at different energy scales have been carried out for more then three decades in several research centers. These experiments obtained a lot of information on the borderline between nuclear and particle physics and provided reference data to the results obtained nowadays. At CERN (European Organization for Nuclear Research) the era of ultra-relativistic heavy ion collisions began with the launch of Pb+Pb reactions at 158 GeV at SPS (Super Proton Synchrotron). In 2000, the next heavy ion program was started at the Relativistic Heavy Ion Collider (RHIC) at the Brookhaven National Laboratory (BNL). It was dedicated to study of Au+Au collisions at center of mass energy of 200 GeV per nucleon pair. Results from SPS and RHIC provided indirect evidence that a new state of nuclear matter - the quark-gluon plasma - was indeed produced in ultra-relativistic heavy ion collisions. From the data collected at RHIC the current "standard model" of heavy ion interactions emerged, which characterizes the properties of hot and dense QCD matter and the stages (Figure 1.1) of the high energy nuclear collision.

In 2009 data taking has begun at the world's largest and highest energy particle accelerator, the Large Hadron Collider (LHC) at CERN. LHC is designed to study proton-proton, proton-lead and lead-lead collisions. There are several independent detector experiments at the LHC, specialized in studies of processes occurring at relativistic energies: ATLAS, CMS, ALICE and LHCb. The analysis presented here uses the data collected at **A L**arge

Ion **C**ollider **E**xperiment (**ALICE**), which is the unique dedicated detector experiment assigned to study ultra-relativistic Pb+Pb collisions. The main goals of the LHC heavy ion program are: to search for signals of new physics, to obtain precise characteristics of QGP medium produced in lead beam collisions, to test whether the "standard" heavy ion collision model still describes the phenomena in heavy ion reactions at LHC center-of-mass energy, to compare the data measured at lower energies with those obtained at LHC.

When the quark-gluon plasma is created in ultra-relativistic nuclear reactions, it cannot be directly detected because the hot and dense but rapidly expanding state of quark matter quickly "freezes" into hadrons. Therefore, the properties of QCD matter formed in collisions of heavy ions are concluded based on lepton, photon and/or hadron signals. It is crucial, from the point of view of complementary interplay between theory and experiment, to find reliable observables that can give insight into the dynamics of the collision and provide informations about the features of the created QCD matter. Theoretical studies indicate that such relevant information on the early stages of heavy ion reactions can be inferred from the analysis of long-range multiplicity correlations.

1.2 Definition of selected variables and characteristics used in heavy ion physics

The main aim of this thesis is to explore the relations between the number of charged particles produced in different regions of kinematic phase-space in Pb+Pb collisions. In order to clarify the terminology, this section provides definitions of observables used in this thesis to classify and analyze processes and phenomena occurring during heavy ion collisions, in particular charged particle correlations.

1.2.1 (Pseudo)rapidity

Particles produced in nucleus-nucleus collisions are characterized by their momenta $\overrightarrow{\mathrm{p}}$ (particle three-momentum) and energies E which are measured with detectors. In high energy physics, commonly used variables to describe particles kinematics are rapidity (y) and pseudorapidity (η). The rapidity of a particle with longitudinal momentum $\mathrm{p_L}$ (component of $\overrightarrow{\mathrm{p}}$ parallel to the beam axis) and energy E is defined by formula:

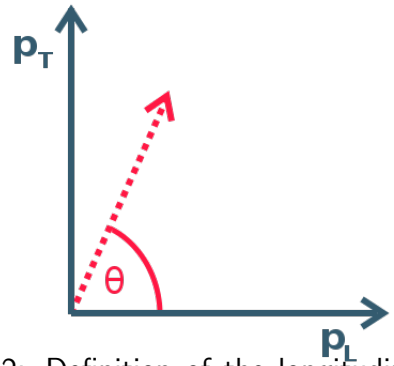

Figure 1.2: Definition of the longitudinal momentum $\mathrm{p_L}$, transverse momentum $\mathrm{p_T}$ (momentum component perpendicular to the collision axis) and the pole angle θ.

$$\mathrm{y} \equiv \frac{1}{2}\ln\left(\frac{\mathrm{E}+\mathrm{p_L}}{\mathrm{E}-\mathrm{p_L}}\right) \tag{1.1}$$

The advantage of using the rapidity is that it transforms additively under the Lorentz boost along z-axis. In collider experiments, for various practical reasons, it is easier to use so-called pseudorapidity, which depends only on the value of the angle θ (the

angle between beam axis and $\overrightarrow{p}$), rather then rapidity. The pseudorapidity is defined for a particle moving at an angle θ relative to the beam axis, or it can be written in an equivalent form as a function of particle momentum ($\overrightarrow{p}$):

$$\eta \equiv -\ln\left[\tan\left(\frac{\theta}{2}\right)\right] \equiv \frac{1}{2}\ln\left(\frac{|\overrightarrow{p}| + p_L}{|\overrightarrow{p}| - p_L}\right) \tag{1.2}$$

The region $y \approx \eta \approx 0$ in phase-space in the center-of-mass frame is referred to as the *midrapidity* region.

1.2.2 Centrality of heavy ion collision

One of the fundamental properties describing the initial stage of ultra-relativistic heavy ion interactions is their geometry at the moment of the collision. The elementary characteristics classifying heavy-ion collision events in relation to the geometry of their reaction is the **impact parameter** ($\vec{b}$)[1] – defined as a vector in the plane perpendicular (XY) to the beam axis (Z-axis). Its length ($|\vec{b}|$) is determined by the distance between the geometrical centers of two colliding nuclei at the moment of their interaction and its direction defines the respective positions of the nuclear centers (Fig. 1.2.2).

The geometrical description of nuclear collisions is provided by the "Glauber" model. It is a phenomenological model, which is based on the assumption that the ultra-relativistic heavy-ion interactions can be represented as a superposition of elementary nucleon-nucleon reactions. In terms of the Glauber model the geometry of nucleus-nucleus collisions can be described by the number of **participant nucleons** (N_{part}) and **spectator nucleons** (N_{spec}). The participant nucleon is a nucleon in one of the interacting ions that undergoes at least one binary collision with the nucleon from the opposite nucleus. The spectators are the nucleons that do not take direct part in the interaction during the event. On the basis of the Glauber model the number of participants and the number of spectators can be directly related to the impact parameter of the heavy ion reaction.

In the present experiments, the geometry of heavy ion collisions is characterized by the percentage fraction of the total nuclear cross section (σ_{AA}), namely with centrality (Centrality(b)). Centrality of a collision with an impact parameter varying within the range $[0, b]$ is defined by the Eq. 1.3.

$$\text{Centrality}(b) = \frac{\int_0^b d\sigma/db'db'}{\int_0^\infty d\sigma/db'db'} = \frac{1}{\sigma_{AA}}\int_0^b \frac{d\sigma}{db'}db' \tag{1.3}$$

The difficulty in the determination of the initial geometry of the nucleus-nucleus reaction lies in the fact that the impact parameter or the number of participants are not directly measurable in heavy ion collision experiments. However, the centrality (geometry) of the events can be determined based on observables that monotonically depend on those geometrical quantities. In Pb+Pb collisions in the ALICE experiment, centrality is estimated based on two observables: the charged particle multiplicity (N_{ch}), or the energy carried by spectator nucleons, namely zero-degree energy E_{ZDC}.

[1] In most of the scientific literature, it is widely accepted to label both the correlation coefficient and the impact parameter with the letter b. In order to distinguish between those two quantities, in the present dissertation the correlation coefficient is marked with b_{corr} while the impact parameter with a single letter b.

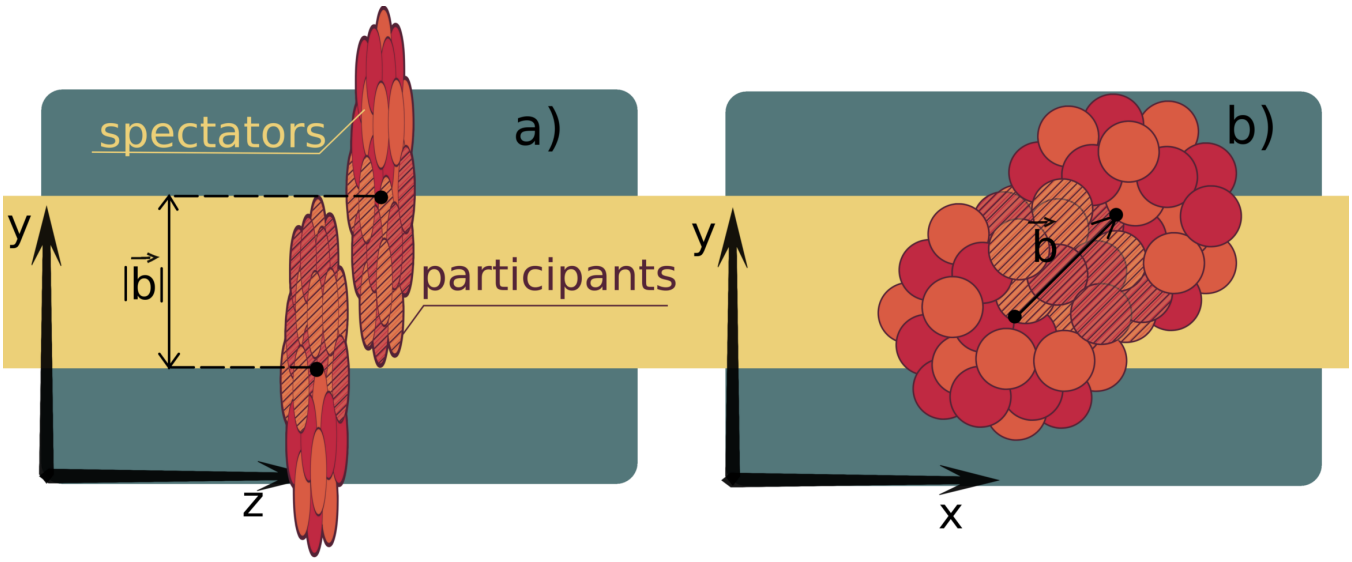

Figure 1.3: Figures a) and b) show the geometry of the collision of two symmetric nuclei. Labels in figure a): the Z axis is the axis parallel to the direction of impact. Nuclei are shown in the YZ plane, the collision occurs in the Z-direction of impact parameter $\vec{b}$. Labels in the figure b): collision is shown in transverse plane (XY). The impact parameter $\vec{b}$ is a vector connecting the centers of the nuclei. Nucleons participants were marked with dashed area.

1.2.3 Charged particle multiplicity distributions

The number of charged particles produced in heavy ion collisions is one of the basic observables to study the reaction process. Their event-by-event measurement determines **the multiplicity distribution of charged particles**, defined as:

$$P(n_{ch}) = \frac{1}{N_{Ev}} \frac{dN}{dn_{ch}} \tag{1.4}$$

where N_{Ev} is the number of events in a given selected sample, while n_{ch} is the number of produced charged particles. Multiplicity distributions are one of the main sources of information about the particle production mechanism in studied collision processes, like Pb+Pb reactions. The basic properties of these distributions can be provided by the measurement of their statistical moments and studies of relations between them.

The charged-particle multiplicity distribution can be analyzed in total pseudorapidity phase-space or in specific kinematic regions like, e.g., pseudorapidity bins (η_1, η_2). This latter possibility is being used in the present analysis. In this thesis the chosen characteristics of charged particle production in lead-lead collisions were always studied for a pair of multiplicity distributions determined in two separate intervals in pseudorapidity phase-space, symmetrically located around midrapidity ($\eta = 0$) in the forward ($\eta > 0$) and the backward ($\eta < 0$) hemisphere of the nucleus-nucleus reaction. Henceforth the quantities measured in the backward pseudorapidity phase-space will be marked with the letter B and in forward with the letter F. This is illustrated in Figure 1.4.

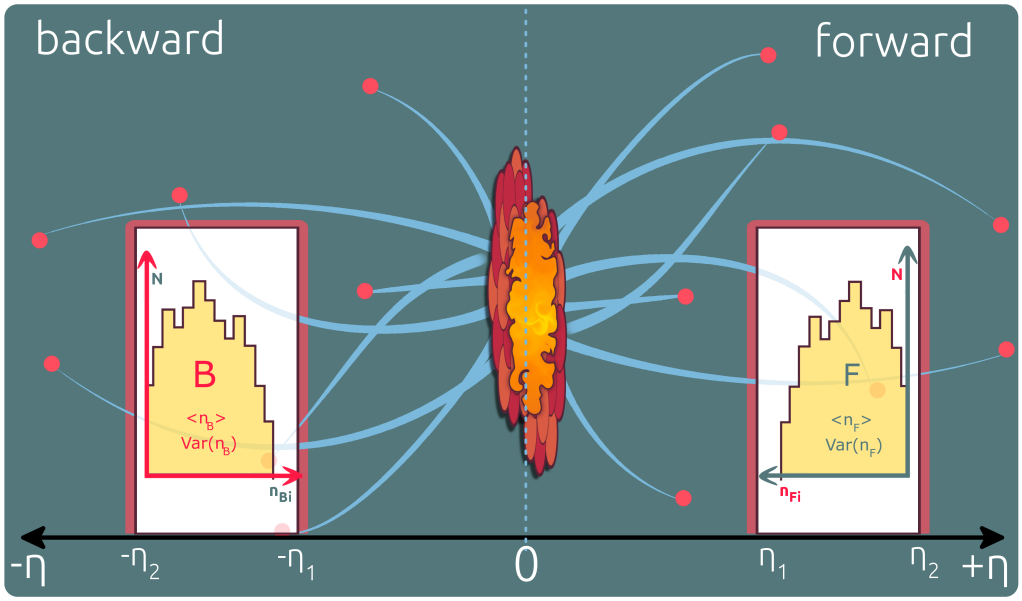

Figure 1.4: Illustration of the pair of pseudorapidity intervals symmetrically located around $\eta = 0$ in forward and backward hemisphere of symmetric nucleus-nucleus collision.

Selected properties of charged particle multiplicity distributions

Below the author has specified key characteristics of charged particle multiplicity distributions, which are important in the context of this study. Let N_{Ev} be the total number of events and n_i denote the number of charged particles measured in each i-th event. The single charged particle multiplicity distribution can be described by following lower-order sample moments:

- **Mean**:

$$< n >= \frac{1}{N_{Ev}} \sum_{i=1}^{N_{Ev}} n_i \tag{1.5}$$

- **Second moment** about zero (second raw moment):

$$< n^2 >= \frac{1}{N_{Ev}} \sum_{i=1}^{N_{Ev}} n_i^2 \tag{1.6}$$

- **Variance**:

$$\mathrm{Var}(n) = \underbrace{\frac{1}{N_{Ev}} \sum_{i=1}^{N_{Ev}} n_i^2}_{\text{second raw moment}} - \underbrace{\left(\frac{1}{N_{Ev}} \sum_{i=1}^{N_{Ev}} n_i \right)^2}_{\text{mean}} = \underbrace{< n^2 >}_{\text{second raw moment}} - \underbrace{< n >^2}_{\text{mean}} \tag{1.7}$$

For every pair of charged-particle multiplicity distributions symmetrically positioned around $\eta = 0$, one in forward and the other in backward pseudorapidity region, one can define two variable (n_{Bi}, n_{Fi}) characteristics such as:

- **Cross moment** of second order:

$$< n_B n_F >= \frac{1}{N_{Ev}} \sum_{i=1}^{N_{Ev}} n_{Bi} n_{Fi} \tag{1.8}$$

- **Covariance**:

$$\begin{aligned} Cov(n_B, n_F) = & \underbrace{\frac{1}{N_{Ev}} \sum_{i=1}^{N_{Ev}} n_{Bi} n_{Fi}}_{\text{second cross moment}} - \underbrace{\frac{1}{N_{Ev}} \sum_{i=1}^{N_{Ev}} n_{Bi} \frac{1}{N_{Ev}} \sum_{i=1}^{N_{Ev}} n_{Fi}}_{\text{product of mean values of the two distributions}} \\ = & < n_B n_F > - < n_B >< n_F > \end{aligned} \tag{1.9}$$

Particularly interesting in terms of understanding the heavy ion early reaction dynamics is the analysis of the **forward-backward correlation coefficient** and the **intensive and strongly intensive quantities, namely** ω, Σ:

- **Forward-backward correlation coefficient**:

$$b_{corr} = \frac{Cov(n_B, n_F)}{\sqrt{Var(n_B) Var(n_F)}} \tag{1.10}$$

- **Intensive quantity** ω – scaled variance:

$$\omega = \frac{Var(n)}{\langle n \rangle} \tag{1.11}$$

- **Strongly intensive quantity** Σ:

$$\Sigma = \frac{(< n_F > \omega_B + < n_B > \omega_F - 2Cov(n_B, n_F))}{< n_B > + < n_F >} \tag{1.12}$$

The forward-backward correlation coefficient b_{corr}, intensive quantity ω and strongly intensive quantity Σ are the subject of the analysis carried out in this thesis. These quantities are described in the following sections in greater detail.

1.3 Forward-backward multiplicity correlation

The forward-backward correlation observable describes the linear dependence between the number of particles produced in the nuclear collision within two selected intervals in pseudorapidity phase-space, symmetrically located around mid-rapidity $\eta = 0$, one in the forward and the other in the backward hemisphere of the reaction (Figure 1.4). The quantitative measure of forward-backward correlation strength is the linear **correlation coefficient** b_{corr}. Customary the forward-backward correlations are studied as a function of the distance between the forward and the backward interval, $\Delta\eta$.

1.3.1 Correlation strength

In the formalism adopted in a large part of studies of the forward-backward multiplicity correlation coefficient, b_{corr} is usually defined as the slope parameter between average multiplicity measured in the backward ($\langle n_B \rangle$) and multiplicity measured in the forward bin (n_F) in pseudorapidity (Eq. 1.13).

$$\langle n_B \rangle = a + b_{corr} n_F \tag{1.13}$$

In an alternative way, the correlation coefficient b_{corr} can be expressed as the covariance of two multiplicity distributions produced in forward and backward pseudorapidity bins, divided by the product of their standard deviations:

$$b_{corr} = \frac{Cov(n_B, n_F)}{\sqrt{Var(n_B)Var(n_F)}} \tag{1.14}$$

It can be shown that for symmetric collisions, like the Pb+Pb reaction analyzed in this dissertation, the two definitions of the forward-backward correlation coefficient are equivalent [14].

The correlation coefficient is a normalized observable, convenient for comparison studies between various types of nuclear reactions. The correlation coefficient may reach values from the range $|b_{corr}| \leq 1$. If $b_{corr} = 1$, it indicates exact positive linear relationship between particles produced in forward and backward rapidity intervals. Next, $b_{corr} = -1$ states on a total negative linear interdependence, that is if n_B increases then n_F decreases and vice versa. When the correlation coefficient is equal to zero, there is no linear dependence between number of particles in forward and backward bins.

1.3.2 Brief overview of forward-backward correlation studies

Studies of multiplicity correlations have a long history in particle physics. Forward-backward correlations have been examined in many different ways, i.e. between the number of particles measured in narrow pseudorapidity intervals up to wide η windows covering whole event hemispheres available in experiment, for all charged particles produced in the collision as well as between particles of opposite $(+-)$ or the same charge $(++, --)$. There have been studies on correlations between multiplicity distributions not only as a function of pseudorapidity gap but also as a function of both pseudorapidity gap $\Delta\eta$ and azimuthal angle $\Delta\phi$.

Over the years the strength of forward-backward correlations has been measured in a wide range of energy and for various types of reactions, including: $e^+ + e^-$ [2, 3, 4], lepton-proton ($\mu^+ + p$, $\nu + p$, $\bar{\nu} + p$) ([6] and references therein), hadron-hadron ($\pi^+ + p$, $K^+ + p$, $\bar{p} + p$, $p + p$)[6, 7, 8, 9], and nucleus-nucleus interactions. In the $e^+ + e^-$ annihilation, weak or no signal of multiplicity correlation was observed; the same applies to the mentioned lepton-proton experiments. In contrast in hadron-hadron, hadron-nucleus and nucleus-nucleus experiments non-zero positive values of the correlation coefficient b_{corr} have been found.

The first evidence of strong, positive forward-backward correlations came from hadron-hadron interactions studied at the CERN Intersecting Storage Rings (ISR) and the Super Proton Synchrotron running as proton-antiproton collider (S$\bar{p}$pS). Results obtained at

CERN ISR for p + p at $\sqrt{s} = 23 - 63$ GeV and at CERN S$\bar{p}$pS for $\bar{p}$ + p at $\sqrt{s} = 200 - 900$ GeV indicated that the forward-backward correlation strength increases with energy and that the correlations span not only over a short range in η space, but also may extend over long distances in rapidity (or pseudorapidity) [7, 8]. Later studies of forward-backward correlations in $\bar{p}$ + p collisions at Tevatron energies ($\sqrt{s} = 300 - 1800$ GeV) in Fermilab remain in agreement with ISR and S$\bar{p}$pS results. The data from Tevatron shows the presence of a positive linear relationship between particles produced in forward and backward bins at a distance above 5 units in pseudorapidity [9].

Forward-backward correlations were measured in Pb+Pb collisions at beam energies of 158A GeV and ^{16}O + AgBr and ^{32}S + AgBr reactions at up to 200A GeV, at SPS at CERN [10, 11]. Much attention was paid to the forward-backward correlation measurement by the STAR experiment at RHIC for both p+p and Au+Au collisions at $\sqrt{s} = 200$ GeV [12, 43, 14, 15, 16]. STAR observed a growth of the values of the correlation coefficient in a wide range of pseudorapidity with the transition from elementary to heavy ion reactions. Studies of Au + Au collisions at RHIC show also a rise of the correlation strength with the centrality of the collision and a decrease of correlation magnitude with increasing separation in pseudorapidity between forward and backward intervals, which was expected due to the drop of "short-range" component of correlations.

At the LHC energies, multiplicity correlations can be studied in p + p, p + Pb and Pb+Pb reactions. Multiplicity correlations in p+p collisions were examined in the ALICE experiment at $\sqrt{s_{NN}}$ =0.9, 2.76 and 7 TeV as function of: (a) the distance between forward and backward interval $\Delta\eta$, (b) the width of these intervals and (c) the pseudorapidity gap ($\Delta\eta$) and separation in azimuthal angle ($\Delta\phi$). An increase of the forward-backward correlation strength is observed with increase of the energy of the p+p collisions. ALICE p+p reaction studies imply that this behavior cannot be explained only by the growth of mean multiplicity [20, 19]. ALICE results for proton-proton collisions are an important source of references for studies on forward-backward correlation in Pb+Pb reactions presented in this thesis.

1.3.3 Short-range and long-range correlations

Correlations between particles can be subdivided into **short-range (SRC)** and **long-range (LRC)**. This division has emerged due to the prediction that LRC and SRC have two different origins.

Short-range correlations are correlations between particles for which the distance in rapidity does not exceed one unit ($|\Delta\eta| < 1$). SRC emerge from short-range order effects, such as hadron resonance decay, particle clusters and jets. For instance, particles coming from a single resonance decay are characterized by a small difference in pseudorapidity and give a contribution to measured SRC.

Contrary to SRC, the correlation present between particles for which difference in their pseudorapidity extends over more then one unit ($|\Delta\eta| > 1$) are called long-range correlations. LRC have been observed in hadronic and nuclear collisions. The existence of long-range correlation was expected on the basis of unitary constraints which break the short range order [25]. There are some speculations based on phenomenological models which attempt to understand the origin of LRC and predict their features starting from elementary hadron-hadron up to heavy ions collisions. Models, such as the Color Glass Condensate model, the Dual Parton Model (DPM) or string percolation models, relate

the presence of long-range correlations in nucleus-nucleus reactions with multiparton interactions [26, 29, 28]. For example, a consequence of multipartonic inelastic collisions in DPM and string percolation models are fluctuations of the number of strings (chains) which give rise to long-range correlations [26]. In a scenario were strings fragment independently, fluctuations of the number of strings should increase with energy and system size (from hadron-hadron to nucleus-nucleus collisions), and so does the value of the correlation coefficient. However, the string percolation model predicts that in heavy ion collisions strings may interact, overlapping and forming clusters. Therefore the number of strings is reduced to the number of clusters, which should result in suppression of LRC [27, 28] in comparison to a model of superposition of independent strings. According to the Color Glass Condensate model [29] only particles (i.e. gluons) produced in early stage of collisions can be correlated in long rapidity ranges. The presence of those early long-range correlations manifests later as LRC measured between the final-state multiplicities of the produced particles. Moreover in paper [30] it is argued that on the basis of the CGC model a growth of LRC with the centrality of the collision is expected.

Whatever the mechanism behind the long-range correlation is, it is believed that the observed multiplicity LRC in heavy ion reactions originate only in the early stages of collisions before elements of the newly created, small system of QCD matter become separated by rapid longitudinal expansion. Thus, long-range correlations should be insensitive to the processes occurring in later phases of the collisions. Proper analysis and interpretation of long-range correlations may give a chance to increase our understanding about the early dynamics of heavy ion reactions. The extraction of long-range component from measured data can be done by selecting a sufficiently large gap ($\Delta\eta$) between intervals for which particle interdependence is examined.

Any interpretation of b_{corr} in terms of "new physics" must be approached with caution. One needs to remember that long-range correlations may be a tool to probe initial dynamics of the heavy ion collisions, however a proper understanding of the measured observables in terms of effects which may distort the carried physical information is required. For instance, studies [31, 32] show that the value of the multiplicity correlation coefficient is strongly sensitive to event-by-event fluctuations of the geometry of the reaction. Therefore, before any attempt to analyze the result in the context of new dynamical phenomena it becomes necessary to determine the input coming from geometry, both for nucleus-nucleus and hadron-hadron collisions.

Recent results of theoretical research suggest a new approach to the topic of long-range correlation, pointing at the possibility of using them as a source signature for particle production in nuclear collisions [33, 34]. Those studies strongly suggest the analysis of LRC in several rapidity intervals. The proposed method focuses on the determination of the relations between moments of multiplicity distributions. The discriminative power of this method increases with the number of bins between which the dependence of multiplicity distributions is examined and can in principle serve to establish the number of sources from which measured particles are produced.

Questions

- What is the forward-backward correlation strength between particles produced in Pb+Pb collisions at the LHC energy, $\sqrt{s_{NN}} = 2.76$ TeV? How does the measured value of correlation coefficient relate to results obtained at RHIC?

- How does the strength of correlation determined in elementary p+p reactions at $\sqrt{s} = 2.76$ TeV change compared to that measured in Pb+Pb collisions at the same energies?

- What is the input coming from the short-range and the long-range component? How does the measured value of correlation coefficient depend on pseudorapidity, centrality class and centrality class width? Does the correlation coefficient depend on the way centrality is estimated in the experiment?

- How large is the contribution coming from geometrical fluctuations to the measured value b_{corr} ? Can it be completely eliminated?

1.4 Intensive and strongly intensive quantities

The size of the system created during heavy ion collisions fluctuates from event to event. Although the multiplicity correlation coefficient b_{corr} may carry information about the early dynamics of nucleus-nucleus interactions, this latter variable might be affected by trivial effects like dependence on number of nucleons participating in the collision and on its fluctuations.

In the studies of nucleus-nucleus event-by-event fluctuations one can distinguish following types of observables: (a) **extensive quantities** which are proportional to system size and (b) **intensive quantities** that do not depend on system volume. The definitions of extensive and intensive quantities originated from the statistical mechanics classification of variables within grand canonical ensemble. A compendium of information about extensive and intensive quantities in the context of event-by-event fluctuations can be found in works of M. I. Gorenstein and M. Gazdzicki [35, 36]. Also in paper [35] authors introduced families of variables that do not depend on system volume nor on its fluctuations, called **strongly intensive quantities**. The definitions extensive, intensive and strongly intensive quantities are derived within grand canonical ensemble or based on the Independent Source Model (ISM). The **Independent Source Model (ISM)**, is a simple superposition model of statistically identical sources between which there are no correlations. The example of ISM is the Wounded Nucleon Model [37].

Some basic properties of extensive, intensive and strongly intensive quantities in the context of ISM

In Independent Source Model the extensive quantities A and B are proportional to number of sources N_S which fluctuate from event to event. Thus their average can be expressed as:

$$\langle A \rangle = \langle a \rangle \langle N_S \rangle \tag{1.15}$$

$$\langle B \rangle = \langle b \rangle \langle N_S \rangle \tag{1.16}$$

where the $\langle a \rangle$, $\langle b \rangle$ are mean values of the distributions $P(a, b)$ for a single source.

The measure of the event-by-event fluctuations of extensive quantities A and B is the scaled variance of their distribution, namely variance normalized to the mean value, ω_{A} and ω_{B}, respectively.

$$\omega_{\mathrm{A}} = \frac{\langle \mathrm{A}^2 \rangle - \langle \mathrm{A} \rangle^2}{\langle \mathrm{A} \rangle} \tag{1.17}$$

$$\omega_{\mathrm{B}} = \frac{\langle \mathrm{B}^2 \rangle - \langle \mathrm{B} \rangle^2}{\langle \mathrm{B} \rangle} \tag{1.18}$$

In Independent Source Model the scaled variance $\omega_{\mathrm{A}}(\omega_{\mathrm{B}})$ reduces to a form where it is expressed with two terms: (1) the scaled variance of the quantity A(B) per source $\omega_{\mathrm{a}}(\omega_{\mathrm{b}})$ and (2) fluctuations of the number of sources ω_{S} (the author has skipped the derivation of the formulas, for details see [35]):

$$\omega_{\mathrm{A}} = \frac{\langle \mathrm{A}^2 \rangle - \langle \mathrm{A} \rangle^2}{\langle \mathrm{A} \rangle} = \omega_{\mathrm{a}} + \langle \mathrm{a} \rangle \omega_{\mathrm{S}} \tag{1.19}$$

$$\omega_{\mathrm{B}} = \frac{\langle \mathrm{B}^2 \rangle - \langle \mathrm{B} \rangle^2}{\langle \mathrm{B} \rangle} = \omega_{\mathrm{b}} + \langle \mathrm{b} \rangle \omega_{\mathrm{S}} \tag{1.20}$$

What follows from Eq. 1.19–1.20 is that the scaled variance does not depend on system size, but it depends on the system size fluctuations (ω_{S}); thus it is an intensive quantity.

When it comes to strongly intensive quantities, a trivial example of a family of these variables can be defined by the ratio of the averages of extensive variables $\langle \mathrm{A} \rangle$ and $\langle \mathrm{B} \rangle$. From the definition 1.15-1.16 one can see that this ratio does not depend on system size $\mathrm{N_S}$ nor on its fluctuations ω_{S}. In paper [35] authors introduce two families of strongly intensive quantities that depend only on the first and second moments, namely the Σ^{AB} family and the Δ^{AB} family.

$$\Delta^{\mathrm{AB}} = \langle \mathrm{C}_{\Delta}^{-1} \rangle [\langle \mathrm{B} \rangle \omega_{\mathrm{A}} - \langle \mathrm{A} \rangle \omega_{\mathrm{B}}] \tag{1.21}$$

$$\Sigma^{\mathrm{AB}} = \langle \mathrm{C}_{\Sigma}^{-1} \rangle [\langle \mathrm{B} \rangle \omega_{\mathrm{A}} + \langle \mathrm{A} \rangle \omega_{\mathrm{B}} - 2(\langle \mathrm{AB} \rangle - \langle \mathrm{A} \rangle \langle \mathrm{B} \rangle)] \tag{1.22}$$

In Eq. 1.21-1.22, the terms $\langle \mathrm{C}_{\Delta} \rangle$, $\langle \mathrm{C}_{\Sigma} \rangle$ are normalization factors proportional to the mean value of any extensive quantity (A or B), the complete procedure of normalization of strongly intensive quantities is given in [36]. Strongly intensive quantities Σ^{AB} and Δ^{AB} do not depend on system size and system size fluctuations (proven in [35]), not only for Independent Source Model but also in terms of statistical model based on grand canonical ensemble of states, where the number of states can be associated with number of events.

This thesis focuses on the studies of the intensive quantity omega $\omega_{\mathrm{A}}(\omega_{\mathrm{B}})$ and the strongly intensive quantity sigma Σ^{AB}. Those observables can be determined for any measured extensive quantities A and B (e.g. transverse momentum of particle and/or particle multiplicity). For this analysis they will be multiplicities of charged particles in backward $\mathrm{n_B}$ and forward $\mathrm{n_F}$ pseudorapidity intervals.

Intensive quantity ω

The scaled variance of the multiplicity distribution, namely variance normalized to the mean, measured in the backward and forward pseudorapidity interval is defined as:

$$\omega_{=} \frac{\mathrm{Var(n)}}{\langle \mathrm{n} \rangle} = \frac{\langle \mathrm{n}^2 \rangle - \langle \mathrm{n} \rangle^2}{\langle \mathrm{n} \rangle} \tag{1.23}$$

As it follows from the discussion made above (Eq. 1.19–1.20) scaled variance of multiplicity distribution in terms of Independent Source Model depends on the scaled variance of multiplicity from an individual source, which in this case can be associated with i.e. a wounded nucleon, and scaled variance of the number of sources (number of wounded nucleons). Hence, ω should be sensitive to fluctuations of the geometry of the collisions, in particular to the width of centrality interval and on the centrality estimator in the experiment.

The emphasis in this thesis was put on the analysis of the intensive quantity ω in terms of system size fluctuations in heavy ion collisions. In the Independent Source Model the scaled variance of multiplicity distribution is more evidently related to the system volume fluctuations (Eq. 1.19 and Eq. 1.20) than the forward-backward correlation coefficient b_{corr}. Understanding the contribution coming from geometrical fluctuations to the measured observables, like ω and b_{corr}, is very important in the context of extracting new information about the dynamics of the reaction and searching for signals of possible "new physics". Another inspiration for the presented study on intensive quantity ω at LHC energies were results from the NA49 experiment [39, 40]. The NA49 Collaboration measured the scaled variance as a function of centrality and size of centrality bins in Pb+Pb collisions at $\sqrt{s_{NN}} = 17.3$ GeV. For the latter NA49 data, a saturation of the value of ω with narrowing of the centrality interval was observed interpreted in the connection to the reduction of geometrical fluctuations. Moreover, a surprising non-monotonic dependence of scaled variance on centrality of the collision was observed, which could not be described using available models. It seems indeed interesting to investigate whether possible hints for such a behavior can be observed at the LHC.

Questions

- How large are the multiplicity fluctuations in Pb+Pb collisions at the energy $\sqrt{s_{NN}} = 2.76$ TeV? Do the values of scaled variance determined for these collisions differ from results obtained at the lower energy $\sqrt{s_{NN}} = 17.3$ GeV?

- How does the value of multiplicity fluctuations change between elementary p+p reactions at $\sqrt{s} = 2.76$ TeV and Pb+Pb collisions at the same energy?

- How does the measured value of scaled variance depend on pseudorapidity, centrality class and centrality class width? Do the multiplicity fluctuations depend on the way centrality is estimated in the experiment?

- How large is the contribution coming from geometrical fluctuations to the measured value of ω? Can it be reduced by, e.g., narrowing the size of centrality intervals? Will values of multiplicity fluctuations saturate as a function of centrality bin width for narrow centrality windows as it was observed for NA49? Does the scaled variance (ω) determined in Pb+Pb collisions in ALICE experiment reproduce the non-monotonic behavior observed at the SPS?

- What is the behavior of scaled variance of multiplicity distribution as a function of pseudorapidity, centrality and centrality bin width? Does it depend on the way

centrality is estimated in experiment?

Strongly intensive quantity Σ

When the studied extensive quantities A and B are the particle multiplicities measured in forward and in backward pseudorapidity intervals, respectively, equation 1.22 takes the form:

$$\Sigma^{n_B n_F} = \frac{1}{\langle n_B \rangle + \langle n_F \rangle}[\langle n_F \rangle \omega_B + \langle n_B \rangle \omega_F - 2\underbrace{(\langle n_B n_F \rangle - \langle n_B \rangle \langle n_F \rangle)}_{\mathrm{Cov}(n_B, n_F)}] \tag{1.24}$$

Here the strongly intensive quantity was normalized in such way ($\langle C^{-1} \rangle = \langle n_B \rangle + \langle n_F \rangle$) that $\Sigma^{n_B n_F} = 1$ when there are no correlations between particles ($\omega_B = \omega_F = 1$ and $\mathrm{Cov}(n_B, n_F) = 0$). Moreover, when the multiplicities of charged particles measured in forward and backward interval, n_F and n_B, do not fluctuate then $\Sigma^{n_B n_F} = 0$. The strongly intensive quantity $\Sigma^{n_B n_F}$ can be characterized by the following properties:

(a) it is symmetric, namely $\Sigma^{n_F n_B} = \Sigma^{n_B n_F}$;

(b) for symmetric type of collision, like Pb+Pb, for which $\mathrm{Var}_F = \mathrm{Var}_B$ and $\langle n_F \rangle = \langle n_B \rangle$ equation 1.24 reduces to form:

$$\Sigma^{n_B n_F} = \omega(1 - b_{corr}) \tag{1.25}$$

(c) defined in terms of the Independent Source Model, $\Sigma^{n_B n_F}$ does not depend on the average number of sources $\langle N_S \rangle$ nor on its fluctuations ω_S.

In this thesis the strongly intensive quantity sigma $\Sigma^{n_B n_F}$ is defined only for charged particle multiplicities measured for a pair pseudorapidity intervals symmetrically located around midrapidity. Therefore in the further text sigma will be labeled as Σ, without superscript.

Questions

- What is the value of strongly intensive quantity Σ for Pb+Pb collisions at energy $\sqrt{s_{NN}} = 2.76$ TeV?
- How does the Σ change with pseudorapidity and does it change with centrality or size of centrality bin? Are indeed values of Σ insensitive to geometrical fluctuations ?
- How values of Σ measured for Pb+Pb collisions correspond to values determined for elementary p+p reactions at the same energy, $\sqrt{s_{NN}} = 2.76$ TeV?

1.5 The Experimental Conditions

This section presents a general description of the experimental situation which builds the context of this analysis.

A **L**arge **I**on **C**ollider **E**xperiment (ALICE) is dedicated to search for signatures and study properties of hot and dense QCD mater produced in Pb+Pb collisions and plays a main part in the heavy-ion program at LHC. The ALICE detector is a 10,000-tons device designed to efficiently measure hadron, lepton (electron and muon) and photon signals in reactions with the highest particle multiplicities. In general ALICE is characterized with a high detector granularity and excellent acceptance in the region of low transverse momentum of particles (threshold $p_T^{min} = 0.15$ GeV/c). Beside lead-lead interactions, the detector measures also the more elementary p+p and p+Pb collisions under the same experimental conditions. This provides references for nucleus-nucleus reactions and carries a complementary and independent information for the results obtained by other LHC experiments.

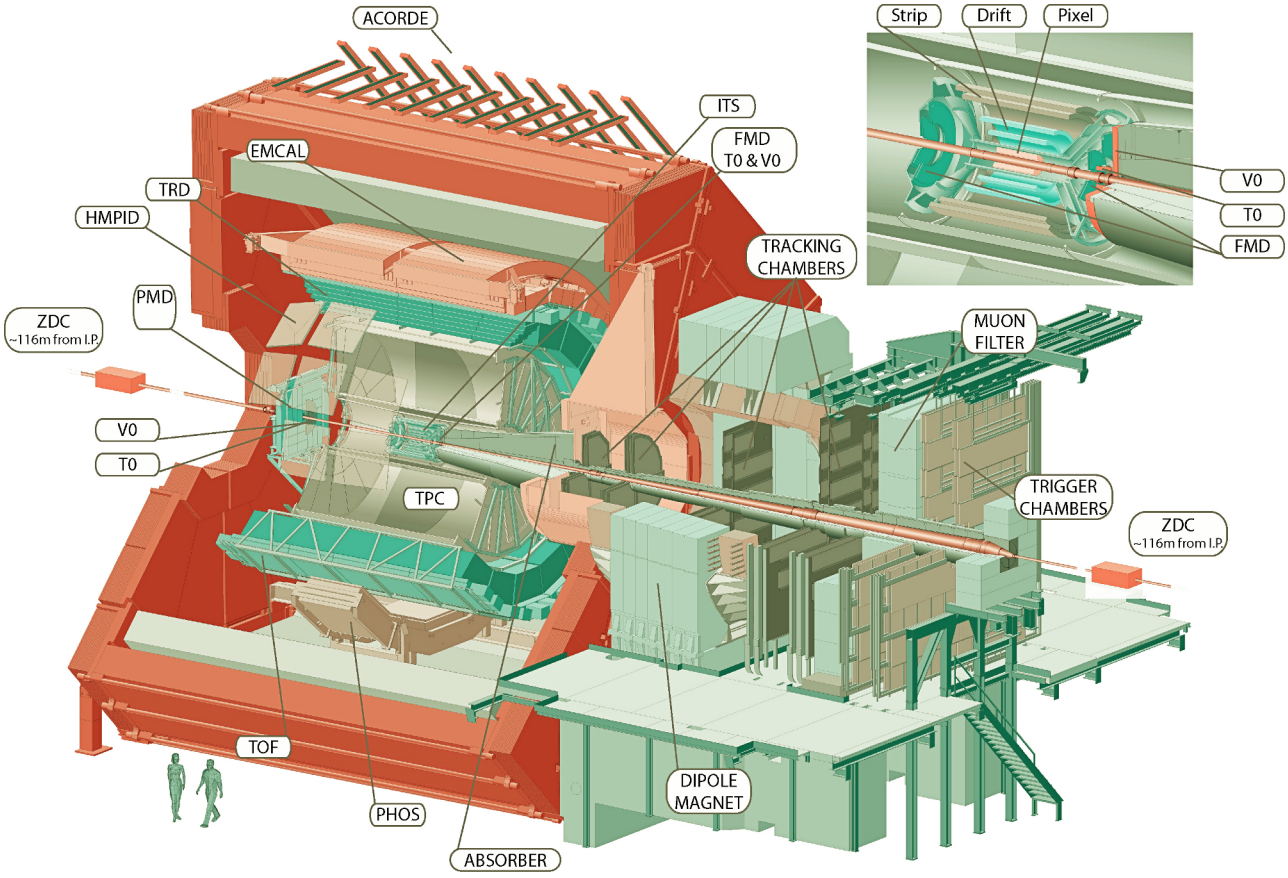

Figure 1.5: Set-up of ALICE detector. Figure comes from [22].

1.5.1 Set-up of ALICE detector

Schematics of the ALICE detector construction is shown in Figure 1.5. ALICE is a complex device consisting of seventeen cooperating sub-detectors which can be divided into four categories:

(a) **Central-barrel detectors** are a set of concentric systems surrounding the interaction point. The task of central-barrel detectors is to provide information about particle production in Pb+Pb, p+Pb and p+p collisions at midrapidity. They were designed: (a) to track charged particles, (b) precisely measure location of primary and secondary vertices, (c) determine particles energy and momenta and (d) identify hadrons, electrons and photons.

The central-barrel system consists of the following components: Inner Tracking System (ITS) made of six layers of silicon detectors, Time Projection Chamber (TPC), Transition Radiation Detector (TRD), Time Of Flight (TOF), Photon Spectrometer (PHOS), Electromagnetic Calorimeter (EMCal) and High Momentum Particle Identification Detector (HMPID). Central detectors are installed inside the L3 solenoid magnet which generates a magnetic field of B = 0.5 T. The presence of the magnetic field results in bending charged particle tracks providing momentum and charge determination based on the measurement of the curvature of the particle trajectory.

(b) **Forward detectors** are a set of smaller devices, such as: Photon Multiplicity Detector (PMD), Forward Multiplicity Detector (FMD), VZERO (V0), T0, Zero Degree Calorimeter (ZDC), located at a small angular distance relative to the beam axis (large η). Those detectors are designed to determine the global characteristics of the reaction (like centrality, reaction plane) and to provide event selection by working as trigger systems.

(c) **The muon spectrometer** is a detector of asymmetric geometry that covers μ^+, μ^- detection in pseudorapidity range $-4.0 < \eta < -2.5$. It was designed to study quarkonia (J/Ψ, $\Psi^{'}$,Υ, $\Upsilon^{'}$, $\Upsilon^{''}$) as well as low mass resonances (ρ, ω, ϕ) and open heavy flavor production in the dimuon decay channel. The muon arm is optimized to enable the measurement of low-p_T charmonium (J/Ψ) production and to provide mass resolution of 100 MeV/c^2, enough to resolve states of Υ meson family in a high-multiplicity environment.

The geometrical acceptance of the ALICE detector is shown in Figure 1.6. Taken all together the ALICE's sub-detectors cover a large interval in pseudorapidity.

1.5.2 The Time Projection Chamber

The TPC is the is the main tracking device in the ALICE experiment. From the perspective of the analysis presented in this thesis, the Time Projection Chamber is the most important detector which provided the information about the charged particle multiplicity for these studies. Briefly, the characteristics of this detector are outlined below.

ALICE TPC is able to measure charged particles in the pseudorapidity range of $|\eta| < 0.8$ with full acceptance and $|\eta| < 0.9$ with reduced acceptance (Fig. 1.6); it covers the full azimuthal angle $\phi = 2\pi$. The Time Projection Chamber is a large-volume gas detector of a cylindrical shape with an inner radius of 85 cm, outer radius 250 cm and a length of 500 cm along the beam direction. Until the end of 2010 during the period of Pb+Pb data taking the detector was filled with 90 m^3 of Ne (85.7%), CO_2 (9.5%) and N_2 (4.8%) at atmospheric pressure [24]. The active volume of the Time Projection Chamber is divided in half by a central electrode, charged to the potential -100 kV, which together with voltage dividing the field cage is designed to provide a uniform electrostatic field

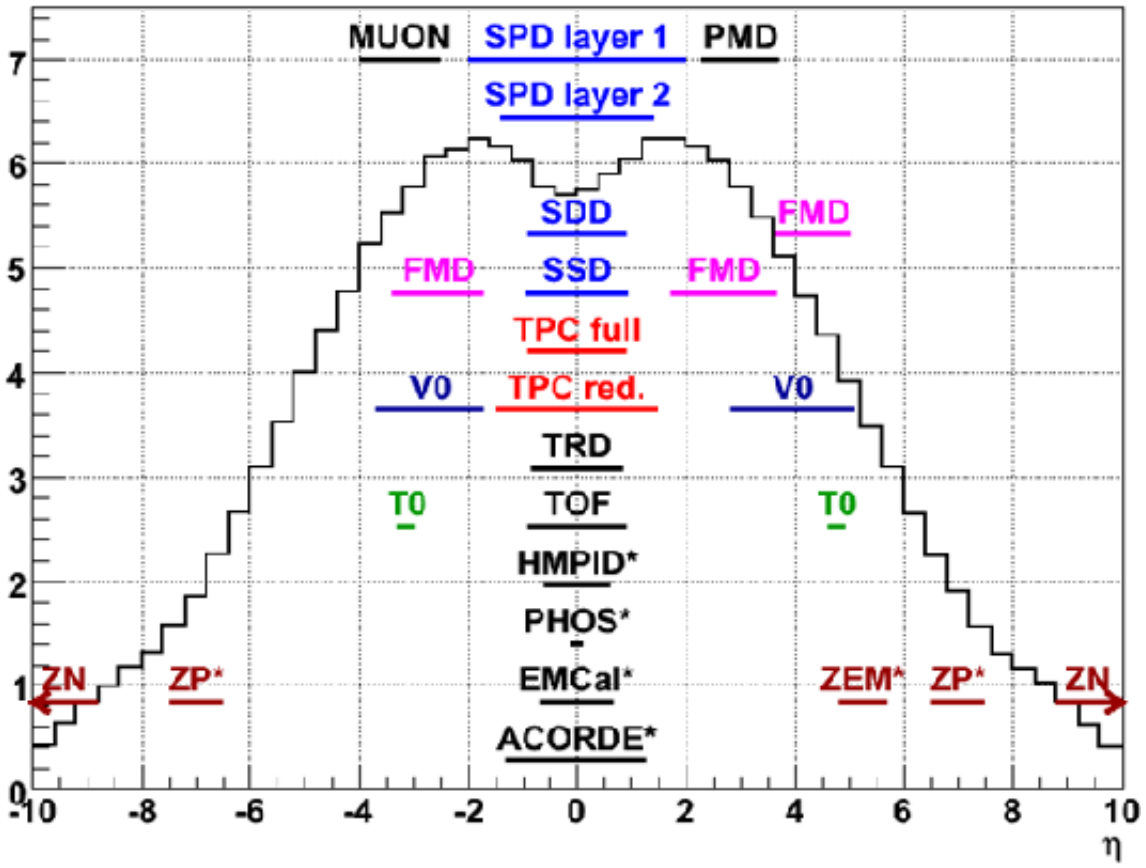

Figure 1.6: Coverage of ALICE sub-detectors in pseudorapidity (η). Figure comes from [23].

for electron drift towards the end plates. The TPC is placed in a magnetic field whose direction, along the Z-axis is parallel to the electric field vector to minimize electron diffusion processes. The two ends of the cylinder are closed with end-caps where sets of Multi-Wire Proportional Chambers (MWPCs) with cathode readout pads are installed. Due to the radial dependence of the track density the end-plates are radially divided into two sectors – the inner readout chambers (IROC) and the outer readout chambers (OROC).

The detection mechanism of the TPC is based on the fact that charged particles traversing the TPC leave a trace of ionization along their paths. In the uniform electric field the electrons drift towards anodes of the proportional chambers at end-plates, where due to the avalanche multiplication caused by the high local field near the wire, the original signal is amplified. From this a positive current is induced on the readout pads of the TPC detector.

In azimuth the TPC end-plates are divided into eighteen trapezoidal sectors, each sector consisting of 159 pad rows. The few million number of pads allows for a precise determination of particle tracks. The trajectory of the particle in transverse (XY) plane is localized by the space distribution of pad signals on end-plates. The Z-direction component is determined by measuring the time of the drift of electrons towards the MWPCs.

1.5.3 ALICE event reconstruction and tracking

A detailed description of all ALICE sub-detectors and their performance can be found in [21], [22]. This section focuses only on those aspects of the experimental measurements which are directly relevant to the analysis presented in this thesis.

The quantities analyzed here are the multiplicity distributions of charged particles produced in a centrality selected Pb+Pb collision. The measurement of the charged particle multiplicity is based on the information from charged particle tracks reconstructed in the ALICE detector.

Particles passing through ALICE interact with the sensitive medium of a detector resulting in the generation of digitized signals on detector's pads. This set of signals adjacent in time and/or space and carrying information about the passage of the same particle is called a "cluster". From the clusters particle tracks are reconstructed, from which information about charged particle multiplicity can be obtained.

Primary-vertex reconstruction

The initial event position of interaction point of the two nuclei, namely the primary event vertex, is determined along the beam axis (Z) and in the transverse plane (XY) based on the cluster signals from the Silicon Pixel Detector (SPD) made of the two innermost layers of the ITS. This initial position of the primary vertex is the input constraint for the tracking procedure described below. Vertex coordinates will be recalculated again, to obtain their final values, after all tracks are reconstructed and using measured track parameters.

Track reconstruction procedure

The reconstruction of charged particle trajectories is one of the most complex tasks in the ALICE experiment. It is a few stage process. Below the basic concept of reconstruction algorithm is given to provide the general idea about the procedure. The description is based on [22].

In a first step, raw detector data are reconstructed into clusters, separately for each detector.

Secondly, the primary vertex is initially determined based on the information provided from the first two layers of the ITS. The determination of particle trajectories starts in the TPC at the outer radius of the detector due to the lower particle densities in that region. Tracking begins with determination of track candidates (seeds). Seeding procedure is done twice; first, seeds are composed of two clusters pointing to the primary vertex, next with three clusters without vertex constraint. One cluster can be assigned to more than one seed. Therefore in order to avoid duplication in the reconstruction of tracks, a special algorithm is used to find pairs of tracks that share a given number of clusters and to reject the track which is characterized by lower quality parameters.

Tracks are prolongated inward, pad-row by pad-row, towards smaller radii of the TPC detector by including clusters in the immediate vicinity. The Time Projection Chamber consists of 159 pad rows, which is the maximum number of clusters a single track may consist of. For a track to be accepted, it should be built of at least 20 out of 159 possible clusters and can miss less than 50% of the clusters expected to be located on the reconstructed trajectory.

For the accepted tracks, the further tracking reconstruction procedure proceeds from TPC down to the outer layers of ITS. Tracks prolongated down from the TPC form seeds for the subsequent ITS track reconstruction algorithm. ITS seeds are prolongated into inwards layers of the detector, and at each new ITS layer the track is being updated by information on the position of all nearest clusters. The result of each update becomes a new ITS seed. Seeding in ITS is also done twice – with and without constraint to vertex position. Overall, for a single track in the TPC a tree of all possible track prolongations in ITS is assigned. Based on a selection algorithm, from each tree of possible ITS tracks one highest quality track candidate is chosen and included in further track reconstruction.

When the ITS tracking procedure is finished, selected tracks are propagated towards the initial primary vertex. Next, the tracking direction is reversed and propagates from the primary vertex to the outer TPC pad rows, particle trajectories are readjusted, based on the information on primary cluster parameters using the Kalman filtering method. At this stage particle tracks are prolongated to outer detectors, respectively, the TRD , TOF, HMPID and PHOS.

In the final step all the tracks are again refitted (by means of the Kalman filtering method) to clusters defined in the previous stage, backwards to the primary vertex.

The trajectory of each single particle is described with a five-parameter helix: the track's curvature (x, y, z), the position of the helix center and the dip angle. Let us note that the Kalman filtering method is used to reconstruct particle tracks, both within a single detector and as particles are passing between two detector systems (e.g., TPC-ITS).

Centrality determination

The important, also in context of this thesis, global characteristics of Pb+Pb event is the centrality of the reaction. Below the basic information about ALICE methods to determine centrality in Pb+Pb collisions is given. The description is based on [24, 22], where also can be found further details on the procedure of centrality measurement in the experiment.

In ALICE experiment, the determination of centrality of Pb+Pb reactions is provided on the basis of two types of observables that change monotonically with the geometry (impact parameter) of the reaction:

(a) **the charged particle multiplicity**, which increases with decreasing impact parameter of the collision;

(b) **the energy carried by the spectator system**, which increases with the increasing impact parameter;

Several sub-detectors with different rapidity coverage can be used to determine centrality. Detectors such as VZERO, SPD and TPC provide centrality estimation based on information on charged particle multiplicity, while the Zero Degree Calorimeter relies on energy carried by particles close to the beam direction (which are mostly spectator nucleons).

Technically, the centrality of the collision is defined as the percentage of the total nuclear interaction cross section (σ_{AA}) computed from lowest impact parameter b (Eq.1.26), which can be re-written as the fraction of the total nuclear cross section from the largest

charged particle multiplicity or from the lowest spectator energy deposition in ZDC detector.

$$\text{Centrality} = \frac{1}{\sigma_{AA}} \int_0^b \frac{d\sigma}{db'} db' \approx \frac{1}{\sigma_{AA}} \int_{N_{charged}}^{\infty} \frac{d\sigma}{dN'_{charged} dN'_{charged}} \approx \frac{1}{\sigma_{AA}} \int_0^{E_{ZDC}} \frac{d\sigma}{dE'_{ZDC}} dE'_{ZDC} \tag{1.26}$$

In order to estimate centrality of the nucleus-nucleus reaction it is fundamental to have knowledge of the nuclear cross section. Even though ALICE interaction triggers have high efficiency in selection of nuclear events, a large background coming from electromagnetic processes (i.e pair production, photo-nuclear interactions), arising from the presence of very strong electromagnetic fields generated during the collision, may still affect the event sample. These electromagnetic processes, as well as peripheral collisions, are characterized by low particle multiplicity. It is important to reject those events. The formula 1.26 can then be simplified by expressing the total nuclear cross section by the number of observed events (N_{events}) corrected for interaction trigger efficiency and for the contribution from electromagnetic processes.

$$\text{Centrality} \approx \frac{1}{N_{events}} \int_{N_{charged}}^{\infty} \frac{dn}{dN'_{charged}} dN'_{charged} \approx \frac{1}{N_{events}} \int_0^{E_{ZDC}} \frac{dn}{dE'_{ZDC}} dE'_{ZDC} \tag{1.27}$$

In this thesis the centrality of Pb+Pb collisions was estimated via charged particle multiplicity measured by VZERO detector and via energy of the spectator nucleons detected with ZDC. These two different centrality estimators can be characterized as follows:

(a) **VZERO centrality estimator**

VZERO is an ALICE plastic scintillator sub-detector located on both sides of interaction point near the beam pipe (Figure 1.5). It covers pseudorapidity ranges $2.8 < \eta < 5.1$ for VZERO-A (ATLAS side) and $-3.7 < \eta < -1.7$ for VZERO-C (CMS side). The detector measures the number of charged particles produced in collisions.

VZERO centrality estimation is based on the sum of amplitudes in the VZERO-A and VZERO-C side. Centrality classes corresponding to the percentage of total nuclear cross section are defined with cuts on the experimental VZERO amplitude distribution. Measured values of multiplicity can be related to the initial geometry of the collision, like the number of participants, impact parameter etc., by simulating and fitting predictions of the Glauber model to the experimental distribution.

(b) **ZDCvsZEM centrality estimator**

The Zero Degree Calorimeter (ZDC) sub-detector consists of two tungsten-quartz neutron calorimeters (ZN) and two brass-quartz proton (ZP) calorimeters located 112.5 m away on both sides of the interaction point. The ZDC measures the energy carried by nucleons that do not participate in the collision (spectators), which can be directly related to the number of participant nucleons.

The energy measured by ZDC is used to estimate the centrality of the collision only in the region of monotonic dependence between E_{ZDC} and the geometry of the collision, i.e. for Centrality $< 40\%$ (the details on this issue can be found in [24, 22],

as described therein). For more peripheral Pb+Pb reactions this monotonic relation is broken. For peripheral collisions a large number of spectator nucleons might bind into nuclear fragments, which, if characterized with proper charge-to-mass ratio, remain in the beam pipe. Their energy will not be detected in the calorimeter. The corresponding lack or very small energy deposition in ZDC during Pb+Pb reaction imitates the signal from central collisions in the ZDC. In order to distinguish between central and peripheral Pb+Pb interactions, the ZDC energy is correlated with another observable also proportional to the number of participants, which is the energy of the photons produced in pion decays and measured by two electromagnetic calorimeters (ZEM). These electromagnetic calorimeters are forward detectors covering pseudorapidity $4.8 < \eta < 5.7$, and located on both sides of the beam pipe. Centrality classes for ZDCvsZEM centrality estimator are determined with the proper cut on the two dimensional distribution of ZDC amplitude as a function of ZEM signal.

In this thesis the centrality of Pb+Pb collisions was determined with ZDCvsZEM centrality estimator in the range $0-40\%$ of total nuclear cross section and for VZERO centrality estimator in the range $0-80\%$ of the total nuclear cross section.

This ends this introductory description of the aims and basic experimental conditions of the study presented in this thesis. The remaining part of this paper is organized as follows. In Chapter 2 the data analysis procedures and methodology, applied corrections and contributions to systematic uncertainties are described. The discussion of the principal results obtained is given in Chapter 3. Main conclusions and a first outlook are presented in Chapter 4. Two technical Appendixes complete this work.

CHAPTER 2

The Analysis

The purpose of Chapter 2 is to provide a precise description of the procedure used in the data analysis, leading to obtain information about the forward-backward charged particle multiplicity correlations, the intensive quantity ω, and the strongly intensive quantity Σ in Pb+Pb collisions at the energy $\sqrt{s_{NN}} = 2.76$ TeV. In this chapter the author delivers the details of the analysis method, defines the data sample and analysis tools used for this study, gives the description of the event selection criteria, the applied analysis cuts and experimental data corrections, as well as of the process of statistical and systematical error estimation.

2.1 Data Sample and Analysis cuts

2.1.1 Pb+Pb Data Sample

The data sample analyzed in this thesis contains information about charged particles produced in minimum bias triggered Pb+Pb events. The data were measured with the ALICE detector at CERN at c.m.s. energy of 2.76 TeV per nucleon pair during a period of LHC Run I at the end of 2010.

The original data set consisted of events registered in 90 lead-lead beam runs. However initial run-by-run studies revealed some significant divergences between measured characteristics of charged particle multiplicity distributions in seven among ninety runs. All seven outlier runs were removed from the data sample in order to prevent the results from bias.

After this run pre-selection the data set undergoing further analysis was composed of 15545100 minimum bias Pb+Pb events which were collected in 83 lead beam runs.

2.1.2 Data Format

ALICE analysis framework provides two types of output data format to store final outcome of event reconstruction procedure (Chapter 1.5.3): the Event Summary Data (ESD) and the Analysis Object Data (AOD). The Event Summary Data files hold information about particles and global event properties reconstructed from raw data, while Analysis Object Data are a reduced size data format, which contains only selected information from ESDs. There can be a version of AOD corresponding to one set of ESDs, where each file version

is individually adjusted for a specific data analysis. This analysis was performed on the version 86 of Analysis Object Data files (AOD086).

2.1.3 Z-Vertex Cut

The interaction point, namely the place along the beam axis inside ALICE detector where two beams interact, is precisely determined in the ALICE experiment, however the position of individual Pb+Pb events may vary around that point. Figure 2.1 shows the distribution of the Z-component of vertex coordinates for the events in the studied lead-lead minimum bias data sample. For the present analysis were accepted only those

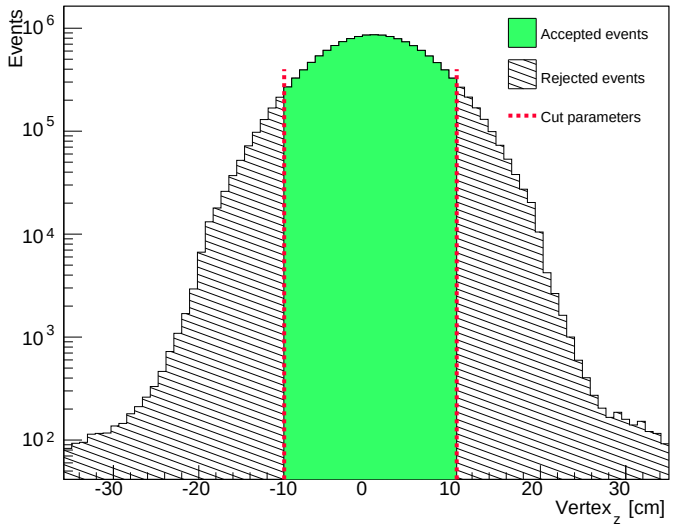

Figure 2.1: Histogram presents a distribution of primary vertex position along Z-axis for minimum bias Pb+Pb events. Pink dashed lines mark ranges of the cut applied on Z-Vertex, only events with vertex located within $|\mathrm{Vertex_z}| \leq 10$ cm (green area) from interaction point entered the analyzed data sample.

events that took place no further than 10 cm in z direction from the interaction point ($|\mathrm{Vertex_z}| \leq 10$ cm). This cut on the value of primary vertex Z-component is important for ensuring the high quality of event reconstruction in the detector, as well as the rejection of background events.

2.1.4 Centrality class selection

In this analysis the classification of Pb+Pb collisions in terms of event geometry was made by using information from two independent centrality estimators, namely VZERO detector and ZDCvsZEM (Section 1.5.3). Centrality determination via VZERO is based on sum of the amplitudes in the VZERO-A and VZERO-C side, which is proportional to the observable measured with this detector, i.e. charged particle multiplicity. Using the VZERO, the Pb+Pb events in this analysis were categorized by their geometry in the centrality range $0 - 80\%$. The estimator ZDCvsZEM provides centrality determination in range $0 - 40\%$, above the turning-point of ZDC (see [22, 24] for technical details).

The specification of centrality of lead-lead collision with calorimeters is built around the measurement of energy deposited by spectator nucleons, which in a very simplified picture is directly related to the number of participant nucleons.

For the purpose of this thesis the minimum bias lead-lead events measured in ALICE experiment were first divided into 10% main centrality classes, namely $0-10\%$, $10-20\%$, $20-30\%$, $30-40\%$, $40-50\%$, $50-60\%$, $60-70\%$ and $70-80\%$ for VZERO estimator and from $0-10\%$, $10-20\%$, $20-30\%$, up to $30-40\%$ for ZDCvsZEM. Centrality interval $0-10\%$ is equivalent to ten percent events with the highest multiplicity for VZERO or ten percent events with lowest spectator energy denoted with calorimeters and defines the sample of central Pb+Pb events while centrality class 70-80% corresponds to the peripheral collisions.

To study data both as a function of the centrality class and the width of centrality interval events within ten percent centrality bins were divided into ten centrality classes of span varying from 10% down to 1%. The ranges of smaller centrality intervals were selected such that the center of each 10% bin remained fixed while reducing the width of the bin. This is shown in Table 2.1.

	centrality classes (%)							
Width	central							peripheral
10%	0.0 - 10.0	10.0 - 20.0	20.0 - 30.0	30.0 - 40.0	40.0 - 50.0	50.0 - 60.0	60.0 - 70.0	70.0 - 80.0
1%	4.5 - 5.5	14.5 - 15.5	24.5 - 25.5	34.5 - 35.5	44.5 - 45.5	54.5 - 55.5	64.5 - 65.5	74.5 - 75.5
2%	4.0 - 6.0	14.0 - 16.0	24.0 - 26.0	34.0 - 36.0	44.0 - 46.0	54.0 - 56.0	64.0 - 66.0	74.0 - 76.0
3%	3.5 - 6.5	13.5 - 16.5	23.5 - 26.5	33.5 - 36.5	43.5 - 46.5	53.5 - 56.5	63.5 - 66.5	73.5 - 76.5
4%	3.0 - 7.0	13.0 - 17.0	23.0 - 27.0	33.0 - 37.0	43.0 - 47.0	53.0 - 57.0	63.0 - 67.0	73.0 - 77.0
5%	2.5 - 7.5	12.5 - 17.5	22.5 - 27.5	32.5 - 37.5	42.5 - 47.5	52.5 - 57.5	62.5 - 67.5	72.5 - 77.5
6%	2.0 - 8.0	12.0 - 18.0	22.0 - 28.0	32.0 - 38.0	42.0 - 48.0	52.0 - 58.0	62.0 - 68.0	72.0 - 78.0
7%	1.5 - 8.5	11.5 - 18.5	21.5 - 28.5	31.5 - 38.5	41.5 - 48.5	51.5 - 58.5	61.5 - 68.5	71.5 - 78.5
8%	1.0 - 9.0	11.0 - 19.0	21.0 - 29.0	31.0 - 39.0	41.0 - 49.0	51.0 - 59.0	61.0 - 69.0	71.0 - 79.0
9%	0.5 - 9.5	10.5 - 19.5	20.5 - 29.5	30.5 - 39.5	40.5 - 49.5	50.5 - 59.5	60.5 - 69.5	70.5 - 79.5

ZDCvsZEM estimator

VZERO estimator

Table 2.1: Table presents the set of centrality classes of Pb+Pb events analyzed in this thesis. Ranges of centrality classes covered with ZDCvsZEM and VZERO estimators are marked in the table.

2.1.5 Track Selection

The ALICE data set for each event carries the information about reconstructed **charged particle tracks**. Studied were only those charged particles whose tracks fulfilled specific selection criteria.

To the analysis were accepted particles whose transverse momentum (p_T) was greater than 0.2 GeV/c, tracks that originated from the primary vertex and also passed a set of, so-called, TPC-only cuts for AOD086 production. Selection of TPC-only cuts narrows information about charged particles paths to the track parameters measured only by Time

Projection Chamber. The detailed set of TPC-only track cuts for a single charged particle is specified below:

(a) the minimum number of clusters per track in TPC detector: **70**;

(b) the maximum $\chi^2/N_{TPCclusters}$: **4.0**;

(c) **NO acceptance** of kink daughter particles;

(d) the maximum Distance of Closest Approach to the primary Z-Vertex (DCA_{ZMax}): **3.2** cm;

(e) the maximum Distance of Closest Approach to XY-Vertex (DCA_{XYMax}): **2.4** cm;

(f) a two dimensional Distance of Closest Approach cut on track is applied. A track is accepted if

$$\sqrt{\left(\frac{DCA_{XY}}{DCA_{XYMax}}\right)^2 + \left(\frac{DCA_{Z}}{DCA_{ZMax}}\right)^2} < 1$$

The TPC-only track selection allowed to avoid ϕ phase-space (azimuthal angle phase-space) acceptance holes in ITS (Section 1.5.1), besides, those cuts criteria provided uniform quality of particle tracks and corresponded to the analysis procedure applied in ALICE p+p correlation studies at $\sqrt{s} = 2.76$ TeV.

2.1.6 Primary and Secondary Particles

Charged particles emerging from hadron-hadron interaction can be divided into two groups: **the primary particles ("primaries")** and **the secondary particles ("secondaries")**. Given below definitions of primaries and secondaries come from analysis note [47], which specifies this terminology for the ALICE data analysis.

Primaries are the particles originally produced in the collision, including all products from electromagnetic decays (i.e. $\Sigma_0 \longrightarrow \Lambda\gamma$), strong decays (i.e. $\phi \longrightarrow K^+K^-$) and weak decays of heavy flavor (containing c,b or t-quarks) hadrons (i.e. $D_0 \longrightarrow K^+\pi^-$), but excluding particles from weak decay of light flavor (u, d, s-quarks) hadrons and muons.

When it comes to secondary particles one can distinguish their two sources: (a) the daughter particles coming from weak decay of light flavor hadrons and muons, e.g., p and π^- can be secondary particles from weak decay of primary particle Λ ($\Lambda \longrightarrow p\pi^-$) and (b) secondaries from material, which include all remaining particles that are neither primaries nor secondaries from weak decays like pions from annihilation of anti-proton with proton from detector material or electrons from γ–conversion.

As for essentially any such analysis of particle production in high energy hadronic or nuclear collisions, the present analysis focuses on the characteristics of *primary* charged particle multiplicity distributions. The contribution from secondary particles, including weak decays, is regarded as an experimental artifact to be subtracted from the data.

2.1.7 Cut on multiplicity distribution

Characteristics of charged particle multiplicity distribution in Pb+Pb collisions were studied for all centrality class listed in Table 2.1 in selected pseudorapidity intervals. Figure 2.2 shows four examples of typical multiplicity distributions obtained in the analysis of the lead-lead reactions after event selection and applying track cuts on the data sample. The plotted histograms show that under the main peak of physical Pb+Pb events, widely extends an unphysical, flat background ("tail"). This tail of multiplicity distribution was present in all studied centrality classes for the entire pseudorapidity region analyzed in this thesis. Several sources of this unphysical "tail" background were proposed in the framework of the discussion induced by the present analysis, including among others remnant "pile-up" events. For the present moment this subject still requires further analysis by ALICE experts.

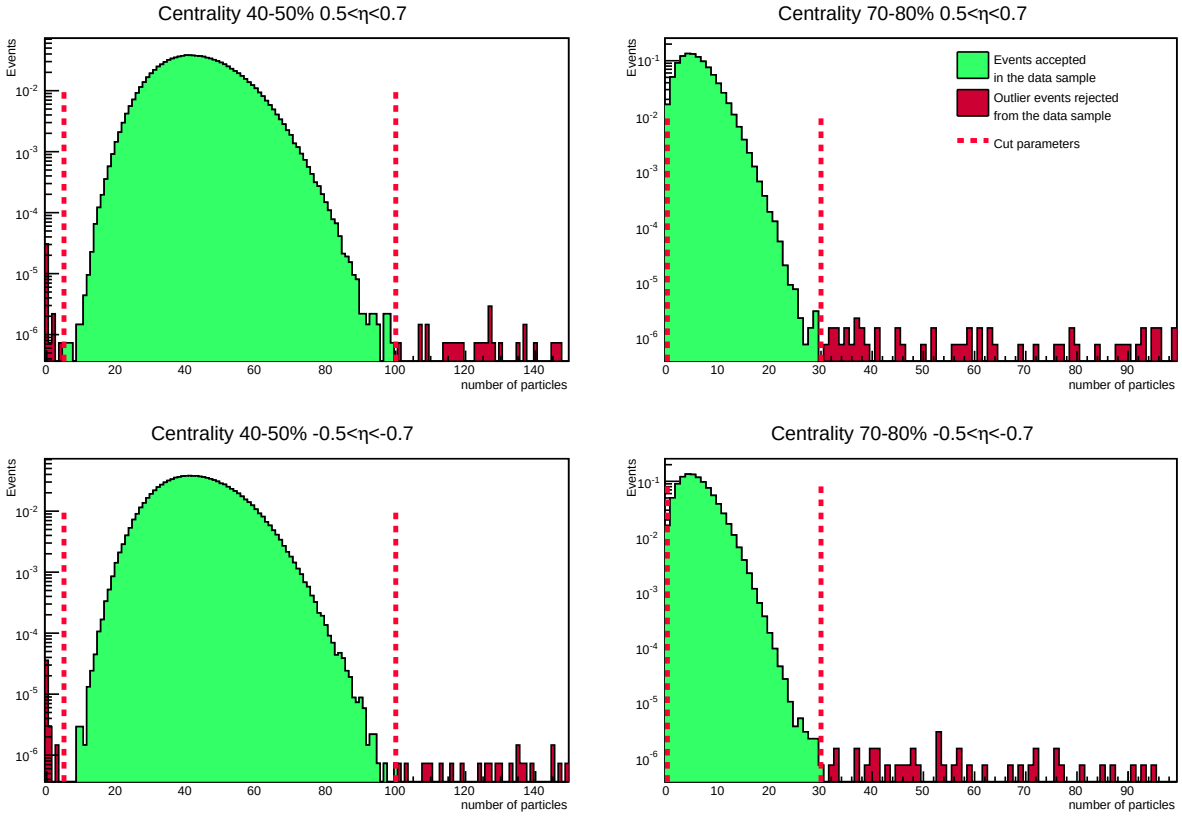

Figure 2.2: Exemplary normalized charged particle multiplicity distributions studied in this thesis. Under the multiplicity distribution (green) extends a flat background of outlier events (dark pink).

In order to remove such "outlier" events from the data sample, a set of cuts on particle multiplicity was applied. Only the events inside a given cut range were further analyzed. The cut parameters were adjusted to maximally reduce the contribution from the outliers to the measured characteristics of the multiplicity distributions and were chosen so that they were always the same for all centrality classes within one column from the Table

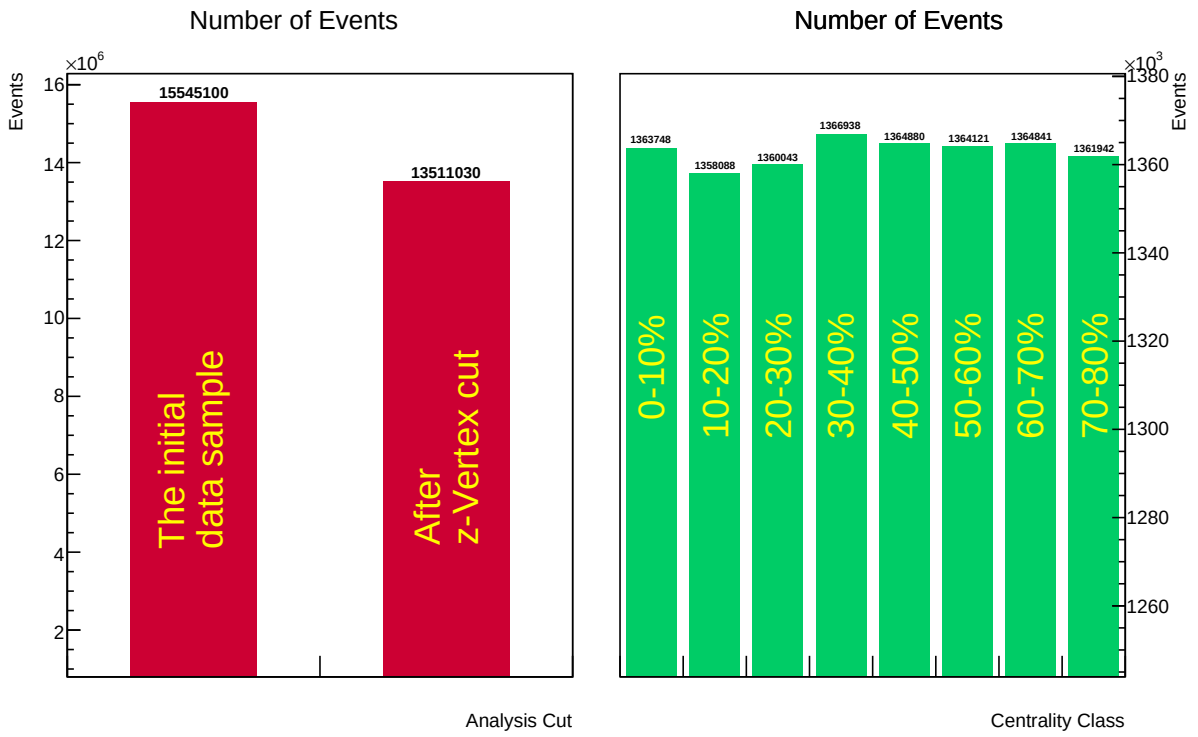

Figure 2.3: Number events in minimum-bias data sample before and after cut on z-Vertex position (left panel). The right panel shows the number of events for selected centrality classes of width 10%.

2.1. The presence of this background contaminates the physical results, distorting the values of measured multiplicity distribution characteristics. The largest contribution from the outlier events to the data sample has been observed for peripheral collisions ($70-80\%$). Further study carried out by the author has shown that the inclusion of the background events into the analysis would have resulted in overestimation of the variance of multiplicity distributions up to 14% and of the covariance and the correlation between particles produced in forward and backward pseudorapidity bins, respectively up to 13% and up to 9%. Moments of multiplicity distribution would have been less affected by the the presence of the tail, the mean maximally by 0.2% and the second order moments not more than 3.5%.

The procedure of cutting the tail described above removes the outlier events only outside the physical peak region. The remaining outliers under the main data peak are one of the sources of systematic uncertainties in this analysis; their estimation is described in Section 2.6.2.

2.1.8 Final Statistics of the data samples

The event selection criteria reduced statistics of the studied initial data sample of Pb+Pb collisions. The information about the data sample size after cutting on position of Z-component coordinate of primary vertex and centrality class selection is shown in Figure

2.3. The z-Vertex cut has reduced the number of events from 15545100 to 13511030 (left panel of Figure 2.3). Within each centrality class, the number of events varied proportionally to the width of the centrality class interval. The effect of multiplicity tail cut on the size of data samples was found insignificant.

2.2 Monte Carlo simulations

Apart from experimental data on Pb+Pb collisions also the information from Monte Carlo (MC) simulations of heavy-ion events was used in this study. The ALICE experiment simulation framework provides various event generators (like HIJING, AMPT) assigned to reproduce Pb+Pb events and emerging primary particles, as well as codes simulating the ALICE detector response to elementary particles passing through the detector material. Particle transport and detector response simulations allow to generate particles interaction inside detector elements and bring, for example, information about secondary particles resulting from such an interaction.

Monte Carlo production for this analysis covered simulation of Pb+Pb collisions at $\sqrt{s_{NN}} = 2.76$ TeV. The generator implemented for lead-lead events simulation was Heavy-Ion Jet Interaction Generator (HIJING). HIJING combines multi-string phenomenology with perturbative QCD processes of minijet production. It is widely used to simulate the particle production in proton-proton, proton-nucleus and nucleus-nucleus collisions. Monte Carlo particle transport code GEANT 3 (GEometry ANd Tracking) was applied to simulate ALICE detector response on particles traversing detector components. For the purpose of this analysis three types of MC simulation output were produced:

(a) MC Truth - providing information about primary charged particle tracks emerging from Pb+Pb collision at $\sqrt{s_{NN}} = 2.76$ TeV, with no simulation of ALICE detector;

(b) MC Primaries - providing information about primary charged particles in Pb+Pb collision at $\sqrt{s_{NN}} = 2.76$ TeV, passing the realistic simulation of the ALICE detector response. The test whether the output particle after passing real detector response was a primary one was made via the function `IsPhysicalPrimary()`, which flags as primaries all the particles produced in the collision including decay products, except for feed-down from weak decays of strange particles (this corresponded to no secondary particle production but realistic detector efficiency);

(c) MC Reconstructed - providing overall information about primary and secondary particles in the Pb+Pb collision with applied realistic simulation of ALICE detector response (primaries+secondaries, realistic detector efficiency).

Simulation output was in AOD format. To the MC results were applied the same event cuts and track selection criteria as for real experimental data.

2.3 Analysis Tools

The analysis has been carried out using specialized software AliROOT. This software is strictly dedicated to the ALICE experiment and enables simulations, reconstruction and analysis of very large amounts of data from heavy ion collisions. The foundation of

AliROOT is a developed at CERN, object-oriented environment ROOT with attached GEANT libraries, which are designed to describe particles passing through the detector material. The rich analysis framework offered by the AliROOT package allowed the author to create appropriate programs for the study of experimental and MC simulation data as well as to process the results. The study of particle multiplicity distributions (moments, variances, covariance, Pearson correlation coefficient) and also the estimation of corrections was performed with the programs written by the author in C++. A selection of experimental data and Monte Carlo simulations was performed using the global computer network GRID. Further analysis of the data was performed locally.

2.4 Analysis Method

The overriding aim of this thesis was to obtain complete information about the forward-backward correlation coefficient, the intensive quantity ω and the strongly intensive quantity Σ in Pb+Pb collisions at $\sqrt{s_{NN}} = 2.76$ TeV. Data analysis covered the studies of characteristics of the charged particle multiplicity distribution not only as a function of centrality class and centrality bin width, but also as a function of pseudorapidity.

2.4.1 Definition of pseudorapidity intervals

The region in pseudorapidity available in this analysis corresponded to the ALICE TPC uniform acceptance range $|\eta| < 0.8$. This was divided into eta bins of a width $\delta\eta = 0.2$. Pseudorapidity bins covering forward ($\eta > 0$) and backward ($\eta < 0$) hemisphere of the reaction were located symmetrically with respect to $\eta = 0$. In this thesis the measured characteristics of the charged particle multiplicity distributions are presented in function of eta gap ($\Delta\eta$). The eta gap in this thesis is determined always for a symmetrical pair of forward-backward bins and is defined as the distance between the lower edge of the forward window and the upper edge of the backward η interval. Data analysis was carried out for the following values of separation between the two intervals: $\Delta\eta$=0, 0.2, 0.4, 0.6, 0.8, 1.0, and 1.2. How do the values of an eta gap correspond to the ranges defining respective forward and backward interval is shown in Table 2.2. Figure 2.4 illustrates the definitions which were adopted in this work: a pair of forward and backward intervals symmetrical around $\eta = 0$ of a width $\delta\eta$ and an eta gap ($\Delta\eta$) as the distance between them.

2.4.2 Measured characteristics of multiplicity distributions

The procedure for data analysis included determination of low-order moments of multiplicity distributions, like **mean** $\langle n \rangle$, **second raw moment** $\langle n^2 \rangle$, **variance**, in each of pseudorapidity intervals for all centrality classes and **second cross moment** $\langle n_B n_F \rangle$ for all pairs of forward-backward pseudorapidity intervals, symmetrically located around midrapidity, in a given centrality bin. Next, values of low-order moments were used to obtain more complex variables such as the value of intensive quantity **omega** ω, **covariance** $\mathrm{Cov}(n_B, n_F)$, forward-backward **correlation coefficient** $b_{corr}(n_B, n_F)$ and strongly intensive quantity **sigma** $\Sigma(n_B, n_F)$.

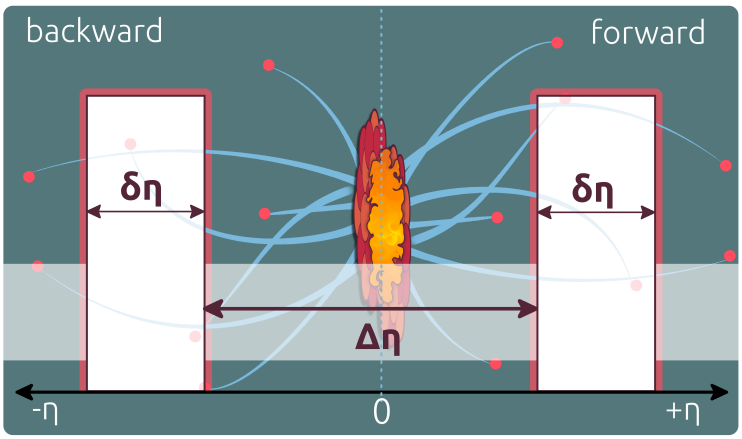

Figure 2.4: The illustration of symmetrical (with respect to $\eta = 0$) forward-backward bins in pseudorapidity of a width $\delta\eta = 0.2$. The characteristics of multiplicity distributions are often studied as a function of the distance between the forward and the backward interval $\Delta\eta$ (eta gap).

TABLE

$\Delta\eta$	Backward	Forward
0.0	-0.2< η <0.0	0.0< η <0.2
0.2	-0.3< η <-0.1	0.1< η <0.3
0.4	-0.4< η <-0.2	0.2< η <0.4
0.6	-0.5< η <-0.3	0.3< η <0.5
0.8	-0.6< η <-0.4	0.4< η <0.6
1.0	-0.7< η <-0.5	0.5< η <0.7
1.2	-0.8< η <-0.6	0.6< η <0.8

Table 2.2: The table lists ranges of pseudorapidity intervals defined for the forward and backward hemisphere of the reactions considered in this work with corresponding eta gap ($\Delta\eta$).

2.5 Data Corrections

Apart from the background "tail" discussed in Section 2.1.7, two additional detector effects may have particular importance in inducing uncontrolled systematics for charged particle measurements in the ALICE TPC. These are: **the presence of secondary particles** and **the limited efficiency of ALICE TPC detector**. Both of these factors directly distort the final number of particles registered in each Pb+Pb event. Hence, it was necessary to apply appropriate corrections for these two effects.

This was done in two steps. Firstly, the data were corrected for secondaries, and then for the reduced total efficiency. In general, the data correction was estimated for the different moments of the multiplicity distributions. Then based on the corrected values of these moments, more complex characteristics such as e.g. variance, covariance, etc., were obtained. The studied characteristics can be analyzed on three stages of correction procedure: before any correction was applied, after the correction on secondaries, and after the total correction on secondaries and reduced efficiency. In order to maintain a clear description the author introduces the following designation for studied observables:

(a) the directly measured quantities corrected neither for secondaries nor for detector reduced efficiency are denoted with placing a tilde over the symbol of the studied characteristics i.e $\widetilde{\langle n \rangle}$,$\widetilde{\langle n^2 \rangle}$, $\widetilde{\mathrm{Var}(n)}$ etc.;

(b) quantities corrected only for presence of secondary particles are denoted with placing a hat over the symbol of the studied characteristics i.e. $\widehat{\langle n \rangle}$, $\widehat{\langle n^2 \rangle}$, $\widehat{\mathrm{Var}(n)}$ etc.;

(c) quantities fully corrected, for both secondaries and reduced detector efficiency, are written without any denotation i.e. $\langle n \rangle$, $\langle n^2 \rangle$, $\mathrm{Var}(n)$ etc.

The values of corrections were determined using Monte Carlo simulation data (Section 2.2). Corrections for secondaries and reduced detector efficiency were applied for all

studied characteristics of charged particle multiplicity distributions, measured in each pseudorapidity interval in each centrality class.

2.5.1 Correction for Secondary Particles

The correction method applied for secondaries was of the "brute force" type. It was constructed under the overall assumption that the most basic properties of the multiplicity distribution of produced charged particles are reasonably well described by the MC simulation (HIJING model), with the use of the precise GEANT3 simulation of the detector response including production of secondaries in the ALICE detection system. The essence of the correction for secondaries was to scale the value of each measured moment, $\widetilde{\mathrm{M}} = \widetilde{\langle \mathrm{n} \rangle}, \widetilde{\langle \mathrm{n}^2 \rangle}$ or$\widetilde{\langle \mathrm{n_B n_F} \rangle}$, with a properly chosen factor $\mathbf{S}_{\widetilde{\mathbf{M}}}$ in order to remove from the measured characteristics the contribution coming from secondary particles:

$$\widehat{\langle \mathrm{n} \rangle} = \mathbf{S}_{\langle \widetilde{\mathbf{n}} \rangle} \widetilde{\langle \mathrm{n} \rangle} \tag{2.1}$$

$$\widehat{\langle \mathrm{n}^2 \rangle} = \mathbf{S}_{\langle \widetilde{\mathbf{n^2}} \rangle} \widetilde{\langle \mathrm{n}^2 \rangle} \tag{2.2}$$

$$\widehat{\langle \mathrm{n_B n_F} \rangle} = \mathbf{S}_{\langle \mathbf{n_B} \widetilde{\mathbf{n_F}} \rangle} \widetilde{\langle \mathrm{n_B n_F} \rangle} \tag{2.3}$$

The terms for coefficients $\mathbf{S}_{\langle \widetilde{\mathbf{n}} \rangle}, \mathbf{S}_{\langle \widetilde{\mathbf{n^2}} \rangle}$ and $\mathbf{S}_{\langle \mathbf{n_B} \widetilde{\mathbf{n_F}} \rangle}$ were derived by inverting the equations 2.1 – 2.3. The values of correction coefficient were estimated by substituting moments determined from Monte Carlo simulation, precisely from Monte Carlo Primaries (MCPrim) and Monte Carlo Reconstructed (MCRec), as seen in the following formulas:

$$\mathbf{S}_{\langle \widetilde{\mathbf{n}} \rangle} = \frac{\widehat{\langle \mathrm{n} \rangle}_{\mathrm{MCPrim}}}{\widetilde{\langle \mathrm{n} \rangle}_{\mathrm{MCRec}}} \tag{2.4}$$

$$\mathbf{S}_{\langle \widetilde{\mathbf{n^2}} \rangle} = \frac{\widehat{\langle \mathrm{n}^2 \rangle}_{\mathrm{MCPrim}}}{\widetilde{\langle \mathrm{n}^2 \rangle}_{\mathrm{MCRec}}} \tag{2.5}$$

$$\mathbf{S}_{\langle \mathbf{n_B} \widetilde{\mathbf{n_F}} \rangle} = \frac{\widehat{\langle \mathrm{n_B n_F} \rangle}_{\mathrm{MCPrim}}}{\widetilde{\langle \mathrm{n_B n_F} \rangle}_{\mathrm{MCRec}}} \tag{2.6}$$

Each of the determined correction factors $\mathbf{S}_{\langle \mathbf{n} \rangle}, \mathbf{S}_{\langle \mathbf{n^2} \rangle}$ and $\mathbf{S}_{\langle \mathbf{n_B n_F} \rangle}$ is approximately constant as a function of both the centrality class and pseudorapidity gap and only slightly fluctuates around its average:

(a) for the first moment within 0.5% around $\langle \mathrm{S}_{\widetilde{\langle \mathrm{n} \rangle}} \rangle = 0.88$;

(b) for the second moment less that 2% around $\langle \mathrm{S}_{\widetilde{\langle \mathrm{n}^2 \rangle}} \rangle = 0.78$;

(c) for the cross moment within 1% around $\langle \mathrm{S}_{\widetilde{\langle \mathrm{n_B n_F} \rangle}} \rangle = 0.78$.

Based on the values of corrected moments, more complex variables free from the contribution coming from secondary particles were obtained, like e.g.:

$$\widehat{\mathbf{Var}(\mathbf{n})} = \widehat{\langle \mathrm{n}^2 \rangle} - \widehat{\langle \mathrm{n} \rangle}^2 = \mathbf{S}_{\widehat{\langle \mathbf{n^2} \rangle}} \widetilde{\langle \mathrm{n}^2 \rangle} - \mathbf{S}^{\mathbf{2}}_{\widehat{\langle \mathbf{n} \rangle}} \widetilde{\langle \mathrm{n} \rangle}^2 \tag{2.7}$$

$$\begin{aligned} \widehat{\mathbf{Cov}(\mathbf{n_F}, \mathbf{n_B})} &= \widehat{\langle \mathrm{n_B n_F} \rangle} - \widehat{\langle \mathrm{n_B} \rangle} \widehat{\langle \mathrm{n_F} \rangle} = \\ &= \mathbf{S}_{\widetilde{\langle \mathbf{n_B n_F} \rangle}} \widetilde{\langle \mathrm{n_B n_F} \rangle} - \mathbf{S}_{\widetilde{\langle \mathbf{n_B} \rangle}} \mathbf{S}_{\widetilde{\langle \mathbf{n_F} \rangle}} \widetilde{\langle \mathrm{n_B} \rangle} \widetilde{\langle \mathrm{n_F} \rangle} \end{aligned} \tag{2.8}$$

2.5.2 Correction for Acceptance and Efficiency Losses

Real detectors, like ALICE TPC, always have only a limited capacity to measure all the products of nuclear collisions. It can happen that some particles emerging from the event are not registered by the detector.

One can distinguish two main causes of particle loss in any detector experiments: **acceptance losses** and **efficiency losses**. Acceptance losses occur when sensitive volume of the detector does not fully cover the considered kinematical phase-space for particle production. The detector acceptance is determined by its geometrical configuration and by the presence or absence of dead zones within its active volume. Acceptance losses within the TPC active volume are small and are caused by the presence of dead zones in between the readout chambers. The efficiency losses arise when the particles that pass through the sensitive volume of the detector are not registered. For the present analysis, a single, common correction has been constructed to make up for both acceptance and efficiency losses.

Determination of the Correction

This correction was determined according to the method proposed by Carsten Soegard in [45]. The correction procedure is based on the assumption that the process of particle losses in active detector volume can be approached statistically and that probability of particle being detected, $\mathbf{A}$, is equal for all particles in the studied (narrow) region of pseudorapidity phase-space. The values for this probability range from $\mathbf{0} \leq \mathbf{A} \leq \mathbf{1}$ and represent the fraction of the detection efficiency in the analyzed pseudorapidity interval, where $\mathbf{A} = \mathbf{0}$ means that the particle was not detected while $\mathbf{A} = \mathbf{1}$ corresponds to a full detection efficiency of the detector. The probability for a particle not being detected in the region of interest is $(\mathbf{1} - \mathbf{A})$.

The correction method derived in [45] does not include the effect of secondaries in the measured number of particles. Therefore, before correcting the data for the reduced efficiency of the detector, the characteristics of charged particle multiplicity distribution firstly have been corrected for the presence of secondaries using the correction method described in Section 2.5.1.

The main idea behind this correction method was to derive an expression for the moment-generating function M(t) that includes effects from reduced efficiency, in other words, the probability $\mathbf{A}$ of detecting a particle. A moment-generating function (m.g.f.) is an alternative way to describe a distribution of a random variable n, in case of multiplicity distribution this random variable n is the number of charged particles. For a distribution

characterized with a probability function P(n) m.g.f. is defined as:

$$M(t) \equiv \sum_{n=0}^{\infty} e^{nt} P(n) \tag{2.9}$$

If M(t) exists around $t = 0$ then the k-th moments of the distribution can be found by differentiating k-times of M(t) at zero:

$$M_k \equiv \frac{d^k M(t)}{dt^k}\Big|_{t=0} = \sum_{n=0}^{\infty} n^k e^{nt} P(n)\Big|_{t=0} = \langle n^k e^{nt} \rangle\Big|_{t=0} = \langle n^k \rangle \tag{2.10}$$

From the properties of joint m.g.f. one can obtain the values for cross-moment between two random variables, in particularly between n_F and n_B – the number of particles measured in a forward-backward pair of pseudorapidity bins defined with the equation:

$$M(t_B, t_F) = \sum_{n_F=0}^{\infty} \sum_{n_B=0}^{\infty} e^{n_B t_B + n_F t_F} P(n_B, n_F) \tag{2.11}$$

Hence, the second cross-moment between the pair of multiplicity distributions located symmetrically in forward and backward pseudorapidity bins can be determined by taking the second cross partial derivative of Eq. 2.11 at point $t_B = t_F = 0$:

$$M_{BF} = \frac{d^2 M(t_B, t_F)}{dt_B dt_F}\Big|_{t_B=t_F=0} = \sum_{n_F=0}^{\infty} \sum_{n_B=0}^{\infty} n_B n_F e^{n_B t_B + n_F t_F} P(n_B, n_F)\Big|_{t_B=t_F=0} =$$

$$= \langle n_B n_F e^{n_B t_B + n_F t_F} \rangle\Big|_{t_B=t_F=0} = \langle n_B n_F \rangle \tag{2.12}$$

In [45] it has been shown that the moment-generating function $\widehat{M(t)}$ of charged particle multiplicity distributions, that takes into account detector efficiency $\mathbf{A}$ can be expressed in the following form:

$$\widehat{M}(t) = \sum_{n=0}^{\infty} e^{n \ln\{\mathbf{A}e^t + (1-\mathbf{A})\}} P(n) \tag{2.13}$$

The equation 2.13 shows moment generating function of the charged particle multiplicity distribution of the probability function P(n) rewritten in terms of a new variable $n \ln\{Ae^t + (1-A)\}$. Likewise, a bi-variate moment-generating function $\widehat{M(t_B, t_F)}$ for a pair of forward-backward multiplicity distributions can be written as:

$$\widehat{M(t_B, t_F)} = \sum_{n=0}^{\infty} e^{n_B \ln\{\mathbf{A_B}e^{t_B} + (1-\mathbf{A_B})\}} e^{n_F \ln\{\mathbf{A_F}e^{t_F} + (1-\mathbf{A_F})\}} P(n_B, n_F), \tag{2.14}$$

where $\mathbf{A_B}$ and $\mathbf{A_F}$ are detection probabilities in backward and forward pseudorapidity bins. In case of perfect detector with full efficiency, $\mathbf{A} = \mathbf{1}$, the equations 2.13 and 2.14 are reduced to formulas 2.11 and 2.12.

In order to evaluate the appropriate correction factors one needs to determine how those characteristics of charged particle multiplicity distributions measured with detector of limited detection efficiency, $\widehat{M(t)}$, relate to the corresponding quantities obtained

in a measurement with a perfect detector of full detection efficiency, namely obtained from moment-generating function M(t) for detector of perfect efficiency. Differentiating function $\widehat{\mathrm{M(t)}}$ determines the following relations:

$$\widehat{\langle \mathrm{n} \rangle} = \frac{\mathrm{d}\widehat{\mathrm{M(t)}}}{\mathrm{dt}}\Big|_{\mathrm{t}=0} \quad = \langle \mathrm{n} \rangle \mathbf{A} \tag{2.15}$$

$$\widehat{\langle \mathrm{n}^2 \rangle} = \frac{\mathrm{d}^2\widehat{\mathrm{M(t)}}}{\mathrm{dt}^2}\Big|_{\mathrm{t}=0} \quad = \langle \mathrm{n}^2 \rangle \mathbf{A^2} + \langle \mathrm{n} \rangle \mathbf{A}(1 - \mathbf{A}) \tag{2.16}$$

$$\widehat{\langle \mathrm{n_B n_F} \rangle} = \frac{\mathrm{d}^2\widehat{\mathrm{M(t_B, t_F)}}}{\mathrm{dt_B dt_F}}\Big|_{\mathrm{t_b}=\mathrm{t_F}=0} = \langle \mathrm{n_B n_F} \rangle \mathbf{A_B A_F} \tag{2.17}$$

A simple transformation of the equations 2.15 – 2.17 allows to express the characteristics of charged particle multiplicity distribution defined for the full efficiency of the detector ($\mathbf{A} = \mathbf{1}$) in terms of combination of the quantities measured with the detector of reduced efficiency ($\mathbf{0} < \mathbf{A} < \mathbf{1}$) and the value of probability $\mathbf{A}$.

$$\langle \mathrm{n} \rangle = \frac{\widehat{\langle \mathrm{n} \rangle}}{\mathbf{A}} \tag{2.18}$$

$$\langle \mathrm{n}^2 \rangle = \frac{1}{\mathbf{A^2}}(\widehat{\langle \mathrm{n}^2 \rangle} - \widehat{\langle \mathrm{n} \rangle}(1 - \mathbf{A})) \tag{2.19}$$

$$\langle \mathrm{n_B n_F} \rangle = \frac{\widehat{\langle \mathrm{n_B n_F} \rangle}}{\mathbf{A_B A_F}} \tag{2.20}$$

$$\mathrm{Var(n)} = \frac{1}{\mathbf{A^2}}(\widehat{\mathrm{Var(n)}} - \widehat{\langle \mathrm{n} \rangle}(1 - \mathbf{A})) \tag{2.21}$$

$$\mathrm{Cov(n_B, n_F)} = \frac{\widehat{\mathrm{Cov(n_B, n_F)}}}{\mathbf{A_B A_F}} \tag{2.22}$$

$$\mathrm{b_{corr}} = \frac{\mathrm{Cov(n_B, n_F)}}{\sqrt{\mathrm{Var(n_B)Var(n_F)}}} = \\ = \frac{\widehat{\mathrm{Cov(n_B, n_F)}}}{\sqrt{(\widehat{\mathrm{Var(n_B)}} - \widehat{\langle \mathrm{n_B} \rangle}(1 - \mathbf{A_B}))(\widehat{\mathrm{Var(n_F)}} - \widehat{\langle \mathrm{n_F} \rangle}(1 - \mathbf{A_F}))}} \tag{2.23}$$

The detection probability $\mathbf{A}$ (total efficiency) can be determined from the formula 2.18 as a ratio of the average number of reconstructed primary particles $\widehat{\langle \mathrm{n} \rangle}_{\mathrm{MCPrim}}$ over the number of primary particles emitted from the collision and registered with the detector of a perfect total detection efficiency $\langle \mathrm{n} \rangle_{\mathrm{MCTruth}}$:

$$\mathbf{A} = \frac{\widehat{\langle \mathrm{n} \rangle}_{\mathrm{MCPrim}}}{\langle \mathrm{n} \rangle_{\mathrm{MCTruth}}} \tag{2.24}$$

The values for $\widehat{\langle n \rangle}_{\mathrm{MCPrim}}$ and $\langle n \rangle_{\mathrm{MCTruth}}$ were estimated based on Monte Carlo simulations of Pb+Pb collisions, namely MC Primaries and MC Truth described in the Section 2.2. The typical value of detection probability is $\langle \mathbf{A} \rangle = 0.83$. Deviation from typical value is no more than 0.6% in pseudorapidity and between different centrality classes.

Only after the imposition of correction procedures for secondaries and the detector acceptance and efficiency losses in the right order could the results be claimed free from the two main effects distorting the measurement.

2.5.3 Effect of total detector correction on measured quantities

In this subsection the effect of both corrections, for secondary particles (Section 2.5.1) and for total detector efficiency (Section 2.5.2), on physical data is discussed. The superposition of these two corrections (for secondaries and for total detector efficiency) is referred to as the **total detector correction** further in the text.

The total detector correction was applied on the data for Pb+Pb collisions with VZERO centrality selection. The discussion focuses on the way this correction affects the values of the three observables studied in this thesis, b_{corr}, ω and Σ. For each analyzed quantity, the values of the total detector correction depend slightly differently on centrality classes, centrality class width and pseudorapidity gap. Tables 2.3, 2.4 and 2.5 show to what extend the presence of the superimposed two corrections, for secondaries and total detector efficiency, changes the measured values of respectively:

(a) **the correlation coefficient**

For b_{corr} the overall correction factor depends on pseudorapidity and width of centrality classes.

Effect of corrections on values of b_{corr}

typical		ΔCentrality $= 1\%$	ΔCentrality $= 10\%$
4%	$0.8 \leq \Delta\eta \leq 1.2$	7%	3.3%
	$\Delta\eta = 0.0$	3.7%	2.6%

Table 2.3: The value of the effect of total detector correction on the correlation coefficient b_{corr}. Typical correction factor values are given in dependence of centrality bin width and pseudorapidity gap.

(b) **the scaled variance of multiplicity distribution ω**

For the scaled variance of charged particle multiplicity distributions, the effect of the correction changes a little with centrality class, and slightly increases with increasing size of centrality class bin.

Effect of corrections on values of ω

typical		ΔCentrality $= 1\%$	ΔCentrality $= 10\%$
1.5%	for central $(0-30\%)$ collisions	1%	3.6%
	for $(30-80\%)$ collisions	1%	2%

Table 2.4: The value of the total detector correction on the scaled variance ω. Typical values of the correction are given in dependence of centrality bin width and centrality classes.

(c) **the strongly intensive quantity Σ**

For Σ the effect of the corrections on measured quantity is quite homogeneous as a function of centrality class and width of centrality class, as well as pseudorapidity.

Effect of corrections on values of Σ

typical		ΔCentrality = 1%	ΔCentrality = 10%
1.2%	$\Delta\eta \leq 0.6$	1.1%	1.2%
	$0.8 \leq \Delta\eta \leq 1.2$	1.4%	1.2%

Table 2.5: The value of the total correction for secondary particles and total detector efficiency on the strongly intensive quantity Σ. Typical values of the correction are given in dependence on centrality bin width and pseudorapidity gap.

The three panel Figure 2.5 shows the values of b_{corr} (left panel), scaled variance ω_B (middle panel) and strongly intensive quantity Σ (right panel) determined for Pb+Pb collisions at $\sqrt{s_{NN}} = 2.76$ TeV as a function of pseudorapidity gap. In case of scaled variance ω the values are presented for the backward hemisphere of the reaction (ω_B), therefore for a given interval of width $\delta\eta = 0.2$ each value of $\Delta\eta$ explicitly corresponds to pseudorapidity window $\eta \in [-\frac{\Delta\eta}{2} - \delta\eta, \frac{\Delta\eta}{2}]$. The values in each panel are presented for three different centrality classes of width 10%. The results with applied total detector correction are marked with a solid line and without this correction with a dashed line.

For the actual situation of the present analysis the two corrections, for secondaries and total detector efficiency, seem to partially cancel out so that the overall total detector correction effect is relatively small. The lack of these two corrections for quantities obtained with centrality defined by the ZDCvsZEM estimator induces clearly an additional systematics; this will be estimated in the next section.

2.6 Error estimation

2.6.1 Statistical errors

The measured characteristics of charged particle multiplicity distributions are defined for a data sample randomly chosen from the population and are the estimators of corresponding parameters for the population distribution. The values of a sample characteristics, for example a sample mean, might fluctuate from one data sample to another. This fluctuation of a measured parameter can be described by its sampling distribution. The variance of the sampling distribution of a measured characteristics determines how much the value of the studied quantity varies due to the selection of a random data sample of a given size from the population. Therefore, the square root of the variance of the sample characteristic (like e.g. the square root of variance of a sample mean) is a measure of the statistical error of the studied sample quantity.

The values of variance and hence statistical error for sample moments, sample variance and sample covariance of charged particle multiplicity distributions were estimated using analytical formulas derived assuming that the population consists of N samples each of size N. The expressions for variances of sampling distribution for more complex variables such as the correlation coefficient, omega ω and sigma Σ were estimated using the *delta*

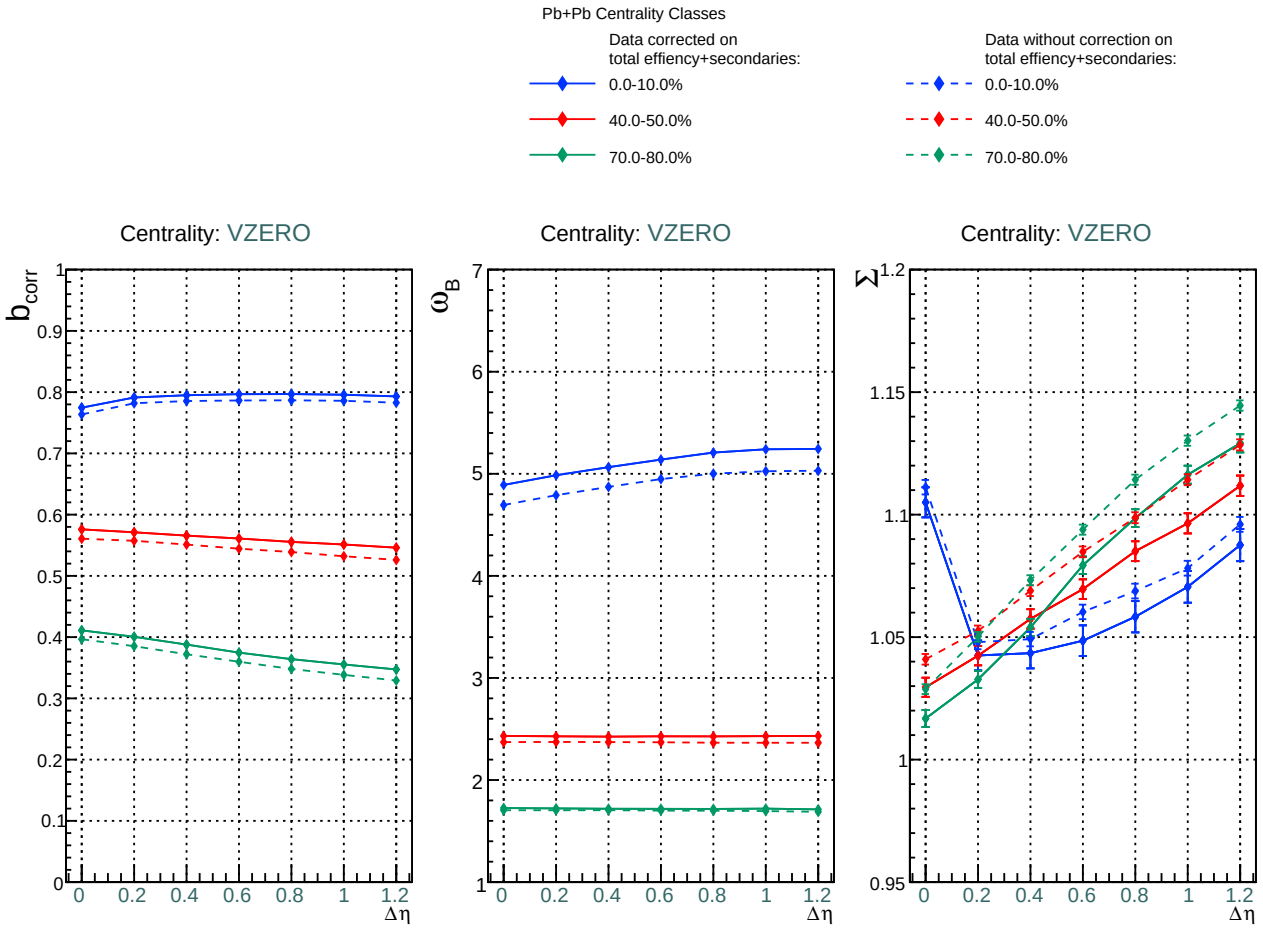

Figure 2.5: The three panel plot presents the value of the correlation coefficient b_{corr}, the scaled variance ω_B and the strongly intensive quantity Σ as a function of $\Delta\eta$ measured for Pb+Pb collisions at $\sqrt{s_{NN}} = 2.76$ TeV in ALICE experiment, for 10% width of centrality class. Results on scaled variance were obtained in the pseudorapidity intervals in the backward hemisphere of Pb+Pb collisions, namely for ω_B. In the figure the results for various centrality classes of Pb+Pb collisions are marked by different colors. The results are presented for the physical data on Pb+Pb collisions with VZERO centrality selection. In each of the three panels, the experimental values with applied total detector corrections (solid line) are compared to the values obtained without these corrections (dashed line).

method whose essence is the linear approximation of the measured quantity via a Taylor series expansion. Statistical errors were determined for both corrected and uncorrected characteristics. Complete formulas for statistical errors are given in the Appendix B.

2.6.2 Systematic errors

There were five main sources of systematic uncertainties taken into account in this analysis:

(a) **time/run dependence**
Total data sample analyzed in this thesis consisted of events collected in dozens of

continuous data taking periods (runs). It has been noticed that characteristics of multiplicity distributions determined for each data subsample defined by the events measured in one run fluctuate more than expected according to the limits of statistical uncertainty. Therefore this dependence of the value of the measured quantity on the run number (i.e., on the time when the data were collected) is considered as a source of systematics uncertainties in the present analysis.

To estimate this systematics only runs with high statistics were used in order to reduce the effects related to the statistical fluctuations. As a measure of the systematic uncertainty for each observable studied in this thesis, the author took the maximum deflection of measured quantity in a run-by-run analysis from the value obtained from the total data sample, defined with the events collected in all eighty three runs.

(b) **method of outlier events removal**
The outlier events present in the multiplicity distribution were removed by correctly adjusted cuts on charged particle multiplicity. In run-by-run studies it was observed that for charged particle multiplicity distributions defined for a few particular runs outliers were not present. Thus, the results of the analysis on the data subsample composed of the events from seven selected runs without presence of the outlier background become a cross-check for the tail removal procedure mentioned above.

Therefore, for every studied characteristics of charged particle multiplicity distributions, the systematic uncertainty associated with the tail cut method was estimated as the ratio of the studied quantity obtained with the above alternative cross-check procedure, over the value determined using the cut on charged particle multiplicity.

(c) **presence of the tail under the multiplicity distribution**
The cuts applied on charged particle multiplicity discussed above could not remove the presence of the possible flat background under the multiplicity distributions, which would be the remnant of the outlier tail apparent in Figure 2.2. To calculate the additional systematics caused by the contribution coming from outlier events that entered the data sample, each measured characteristics was studied as a function of width of the accepted interval, the range of which was defined by a two-side cut on the multiplicity distribution, removing the outlier background. The systematics was determined by a linear extrapolation of the measured quantity down to the limit where the accepted interval width was zero.

(d) **chosen data correction method**
Another source of systematics uncertainty was induced by the two-step method of data correction for detector acceptance and efficiency as well as the presence of secondary particles described in Section 2.5. This was evaluated by developing two alternative procedures for correcting the data. The first of these was addressed in Section 2.5; the alternative correction method was of the "brute force" type, based on scaling each measured raw moment of the multiplicity distribution with a coefficient defined as the ratio of corresponding moment for the total number of simulated charged particles (Monte Carlo Truth) over the moment determined for the distribution of reconstructed charged particles (Monte Carlo Reconstructed). The ratio of the two measured quantities corrected using both methods determined the systematics induced by the data correction procedure.

(e) **material budget**
A proper representation of material budget in the real detector is significant in the context of correct simulation of the detector response. If wrongly estimated, it contributes to systematics at the level of data corrections. For the present analysis, the uncertainties related to material budget were evaluated on the basis of the analysis made for p+p collisions at $\sqrt{s} = 2.76$ TeV in [45]. For the proton-proton analysis information about multiplicity distributions was provided with ALICE FMD and SPD detectors. The corresponding values of systematic uncertainties reached less than 1% for the covariance, around 3% for variance forward, less than 2% for variance backward and 2% for the correlation coefficient. Based on a private communication from an ALICE expert [46] it was determined that in case of the Time Projection Chamber, the possible uncertainties in material budget may locally reach maximum values of $\pm 2\%$, however in general they are much smaller. These uncertainties are in fact very significantly lower than these quoted in [45]. On that basis the author concludes that the resulting uncertainties induced on the correlation coefficient as well as the variance, covariance and other quantities discussed in this thesis will be negligibly small. As such, they were disregarded from the present analysis.

(f) **lack of total detector corrections for data with ZDCvsZEM centrality selection**
An additional problem was imposed by the lack of total detector corrections to be applied on quantities obtained with ZDCvsZEM centrality selection. This clearly induced an additional systematic uncertainty for all the considered quantities. For the present time, the latter uncertainty was effectively estimated on the basis of the experience gained for VZERO centrality selection-based analysis, in particular of the behavior of the corrections discussed in section 2.5.3. Pessimistic error margins were assumed to take account of possible additional differences between VZERO and ZDCvsZEM centrality selection.

Typical values of systematic errors discussed above are given in the table below. The differentiation between columns "total detector corrections (VZERO)" and "total detector corrections (ZDCvsZEM)" takes account of the issue discussed above, the latter column specifying the estimated uncertainty induced by the lack of efficiency corrections for the ZDCvsZEM centrality selection. From the Table 2.6 it becomes apparent that as it was to be expected, the lack of total detector corrections to be applied on the ZDCvsZEM centrality selection-based quantities is by far the dominant error source for the latter quantities. This gives room for significant improvement in future experimental studies but does not significantly affect the physics conclusions presented in the next chapter. For VZERO centrality selection, the partial error sources remain much smaller and typically below 2%.

The total systematic errors were obtained by adding all the considered partial error sources in quadrature, taking into account their occasionally rapid dependence on the collision centrality, centrality bin width, and particle pseudorapidity. For better clarity, the presentation of these is postponed to the discussion of physics results made in the next chapter.

quantity	total detector corrections		tail in mult. distribution		time
	VZERO	ZDCvsZEM	cut	no-outlier method	dependence
ω_B,ω_F	0.8%	$2-5$%	0.4%	1.4%	1.6%
Σ	0.9%	2%	0.3%	1.2%	1.4%
b_{corr}	1.4%	$4-16$%	0.3%	2.3%	0.6%

Table 2.6: Typical values of relative systematic errors considered in the present analysis. The minimal (maximal) limits for the error induced by lack of total detector corrections for the ZDCvsZEM centrality selection corresponds to results obtained with ΔCentrality = 1% (10%) for the case of the scaled variance ω_B, ω_F and to the region of $\Delta\eta = 0$, ΔCentrality = 10% ($\Delta\eta = 1.2$, ΔCentrality = 1%) for b_{corr}.

2.6.3 Estimation of intensive quantity ω and strongly intensive quantity Σ for p+p collisions

The values of the correlation coefficient b_{corr}, sigma Σ and scaled variance ω analyzed in this thesis for Pb+Pb collisions at $\sqrt{s_{NN}} = 2.76$ TeV were compared to measured or estimated values of these quantities for p+p reactions at the same energy. Information about p+p collisions comes from publication [20] which provides directly experimental results, only for values of the forward-backward correlation coefficient (b_{corr}^{pp}) as a function of pseudorapidity gap ($\Delta\eta$). The values of correlation coefficient in p+p collisions were measured between pairs of forward-backward intervals of width $\delta\eta = 0.2$. The distance between those two intervals, namely pseudorapidity gap $\Delta\eta$, was defined analogously to the definition given in the present study for Pb + Pb collisions.

At the moment of writing this thesis there are no available ALICE data for ω and Σ in proton-proton reactions at energy $\sqrt{s} = 2.76$ TeV. In order to compare the results for the intensive and strongly intensive quantity obtained for lead-lead collisions to those in elementary proton-proton reactions, the author had to develop a method to estimate the values of ω and Σ for p+p interactions. The estimation was based on "the model of random distribution of produced particles in pseudorapidity" [20] and on the assumption that the value of scaled variance was constant as a function of pseudorapidity.

(A) **The model** of random distribution of produced particles in pseudorapidity was tested in [20] in the context of studies of the dependence of b_{corr}^{pp} on the width of pseudorapidity windows $\delta\eta$ at $\Delta\eta = 0.0$. The model assumes the binomial distribution for the probability $P_N(n_F)$ to observe a number n_F of particles in a selected subinterval $\delta\eta$ in pseudorapidity from the total number N of charged particles produced in the total accepted pseudorapidity interval Y. The success probability p of the binomial distribution is given by $p = \frac{\delta\eta}{Y}$. Based on this model, two equivalent formulas determining the value of scaled variance for a symmetric ($\langle n_F^{pp}\rangle = \langle n_B^{pp}\rangle$) p+p collision can be determined.

(a) The first formula relates the value of scaled variance ω_1^{pp} measured in the selected subinterval $\delta\eta$ with the scaled variance determined for the whole available pseudorapidity interval Y, labeled ω_Y.

$$\omega_1^{pp} = (1-p) + p\omega_Y \tag{2.25}$$

(b) The second equation relates omega ω_2^{pp} determined for the pseudorapidity subinterval $\delta\eta$ with the value of the corresponding forward-backward correlation coefficient:

$$\omega_2^{pp} = \frac{1}{1 - b_{corr}^{pp}} \tag{2.26}$$

The publication [20] provides the experimental value of the scaled variance $\omega_{Y=1.6} = 4.25$ in the range of pseudorapidity being equal to $Y = 1.6$. Hence, for $\delta\eta = 0.2$ and Eq. 2.25, the value of scaled variance for proton-proton reactions was estimated to be $\omega_1^{pp} = 1.41$.

The value of omega derived from the second formula (Eq. 2.26) is $\omega_2^{pp} = 1.43$. This value was obtained by substituting to the equation the experimental value for b_{corr}^{pp}, measured for the pseudorapidity gap between the forward and backward pseudorapidity interval being equal to $\Delta\eta = 0$.

(B) For the purpose of this thesis, the author assumed that the estimated values of omega for p+p collisions are constant as a function of pseudorapidity. **This assumption** was based on the following arguments:

(a) The first argument comes from the experimental results obtained at RHIC. The forward-backward correlation studies made for p+p collisions at RHIC [43] indicate a constant value of the variance of multiplicity distribution and of the average number of particles as a function of pseudorapidity, and thus a constant scaled variance;
(b) An introductory and unpublished analysis of p+p reactions at ALICE energies suggests that omega would be roughly constant in the considered range of pseudorapidity.

In this thesis the author estimated the value of the scaled variance ω^{pp} of the multiplicity distribution for the 0.2-units width of pseudorapidity subinterval as the arithmetic mean of values ω_1^{pp} and ω_2^{pp} determined from equations 2.25 and 2.26. This gives $\omega^{pp} = 1.42$. Based on the above argumentation, the author also assumed that omega had the same value for all pseudorapidity sub-intervals of the same width in the region of pseudorapidity $|\eta| < 0.8$ considered in this analysis.

The intensive quantity sigma was estimated from Eq. 1.22, separately for all pseudorapidity intervals studied in this thesis. This was based on the estimated value of ω^{pp} described above, and on the experimental values of the forward-backward correlation coefficient b_{corr}^{pp} measured by ALICE in elementary p+p collisions, taken account of the relation $\Sigma^{pp} = \omega^{pp}(1 - b_{corr}^{pp})$ quoted above.

As the values of ω^{pp} and Σ^{pp} discussed above are only estimated rather than measured, it remains very difficult to provide a full estimate of the corresponding uncertainties account taken of the experimental issues in the p+p data analysis as well as the underlying assumptions. For the present moment only the uncertainty of the estimation method was determined, both for omega and sigma, as the relative deviation between the estimated values of omega obtained with the two methods addressed above (Eq. 2.25 or Eq. 2.26,

respectively). Estimated that way, the corresponding uncertainty was less then 1% both for ω^{pp} and Σ^{pp}.

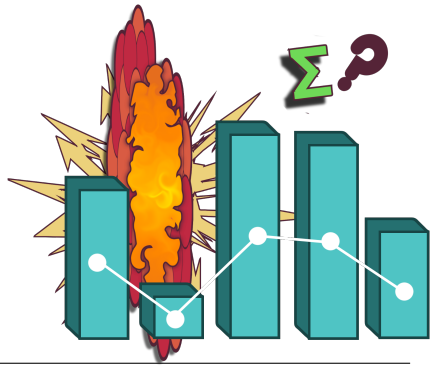

CHAPTER 3

The Experimental Results and Discussion

This chapter presents the outcome of the analysis of forward-backward correlations and fluctuations of the number of charged particles produced in Pb+Pb collisions at $\sqrt{s_{NN}} = 2.76$ TeV measured by the ALICE detector at CERN. The presented results were determined for two centrality estimators, namely for VZERO and for ZDCvsZEM. The discussion of the studies focuses on the three measured quantities: (a) the **correlation coefficient** b_{corr}, (b) the **intensive quantity** ω and (c) the **strongly-intensive quantity** Σ as a function of (1) pseudorapidity gap (2) centrality and (3) width of the centrality bin. The results for centrality selected Pb+Pb collisions (from peripheral to central) were compared to Pb+Pb Monte Carlo HIJING simulations and elementary p+p collisions at the same collision energy.

3.1 Data presentation

Unless explicitly specified, the results are presented on a "three panel" plot (e.g. Figure 3.1), where the arrangement of the figures is always as follows:

(a) the first two panels show the values measured for Pb+Pb physical data determined for ZDCvsZEM centrality estimator (left panel) and VZERO centrality estimator (middle panel), the right panel is dedicated to results of MC HIJING simulations of Pb+Pb collisions with VZERO event selection;

(b) not all the corrections were applied for the results for calorimetric centrality class selection, the measured values for data with ZDCvsZEM centrality estimator are presented without corrections for secondaries and total detector efficiency. The experimental results for VZERO centrality selection are drawn corrected for all effects, detector or systematic, which were considered in Chapter 2;

(c) the statistical errors are plotted always on the same figure as data points for the results;

(d) the three measured observables, namely the correlation coefficient b_{corr}, the intensive quantity omega ω, and the strongly intensive quantity sigma Σ, are presented either as a function of pseudorapidity gap ($\Delta\eta$) for fixed centrality class width (ΔCentrality) or as a function of ΔCentrality for fixed $\Delta\eta$. The centrality class width is given by the difference between upper range and lower range of centrality interval defining the centrality class (ΔCentrality = CentralityMax − CentralityMin);

(e) typical values of systematic errors are provided in form of tables, for each measured observable separately.

3.2 Forward-backward correlation coefficient

3.2.1 Correlation coefficient (b_{corr}) as a function of pseudorapidity

Two three panel plots, Fig. 3.1 and Fig. 3.2, show the values of forward-backward correlation coefficient (b_{corr}) of charged particle multiplicity distributions plotted as a function of pseudorapidity gap, $0.0 \leq \Delta\eta \leq 1.2$, for the selected centrality classes of, respectively, ten percent centrality bin width (ΔCentrality = 10%) and one percent centrality bin width (ΔCentrality = 1%). Observations made based on the presented results are listed below.

Correlation strength for the 10% centrality bin width

Figure 3.1 presents the results of the forward-backward correlation determined for the wide centrality class window of a 10% width. All the three panels show a large value of correlation coefficient determined for physical Pb+Pb collisions in comparison to experimental results for p+p reactions. The plotted results for b_{corr} differ according to the chosen centrality estimator. For the data with centrality defined with ZDCvsZEM, large values of forward-backward multiplicity correlation are observed for all considered centrality classes – from $0-10\%$ up to $30-40\%$. For the data with VZERO centrality selection the highest value of correlation strength, comparable to the values obtained with calorimetric centrality estimators, is apparent for most central collisions ($0-10\%$), and then decreases with decreasing centrality of the nucleus-nucleus reactions. A similar ordering of the correlation strength with centrality of the Pb+Pb collision is observed also for data with ZDCvsZEM centrality estimator, but the corresponding trend is much weaker – the magnitude of the values of b_{corr} measured for various centrality classes is almost comparable.

The correlation coefficient measured for physical data as a function of pseudorapidity gap proceeds from a flat dependence on $\Delta\eta$ in central lead-lead collisions, to a decreasing function of η gap in more peripheral Pb+Pb reactions. This is more evident especially for the results of VZERO centrality selection. This drop of the long-range component of correlation coefficient compared to short-range is similar to the behavior of b_{corr} observed in p+p interactions. The closest apparent similarity in behavior of correlation strength as a function of $\Delta\eta$ between Pb+Pb and p+p collisions is observed for peripheral ($70-80\%$) lead-lead reactions, for results for experimental data with VZERO centrality selection and the corresponding Monte Carlo simulation.

Results of MC HIJING simulation with VZERO centrality selection are in general in good agreement with experimental data with VZERO centrality estimator except for most central collisions. For $0-10\%$ centrality class the Monte Carlo does not reproduce the flat dependence noted in experimental data, instead a decrease of values of b_{corr} with $\Delta\eta$ is observed. Moreover for most central collisions the experimental data exhibit a noticeable drop of the correlation strength at $\Delta\eta = 0$, not present in MC.

The values of the correlation coefficient measured for pair of forward-backward pseudorapidity intervals in the wide 10% centrality class windows are large, around $b_{corr} \approx 0.8$

Error on b_{corr}	VZERO			ZDCvsZEM		
	ΔCentrality=			ΔCentrality=		
	1%	5%	10%	1%		10%
				$\Delta\eta$=0.0	$\Delta\eta$=1.2	
typical	6%	3%	2%	8%	17%	5%

Table 3.1: Total relative systematic errors estimated for the correlation coefficient b_{corr}. Typical error values are given in dependence of centrality estimator, centrality bin width and pseudorapidity gap.

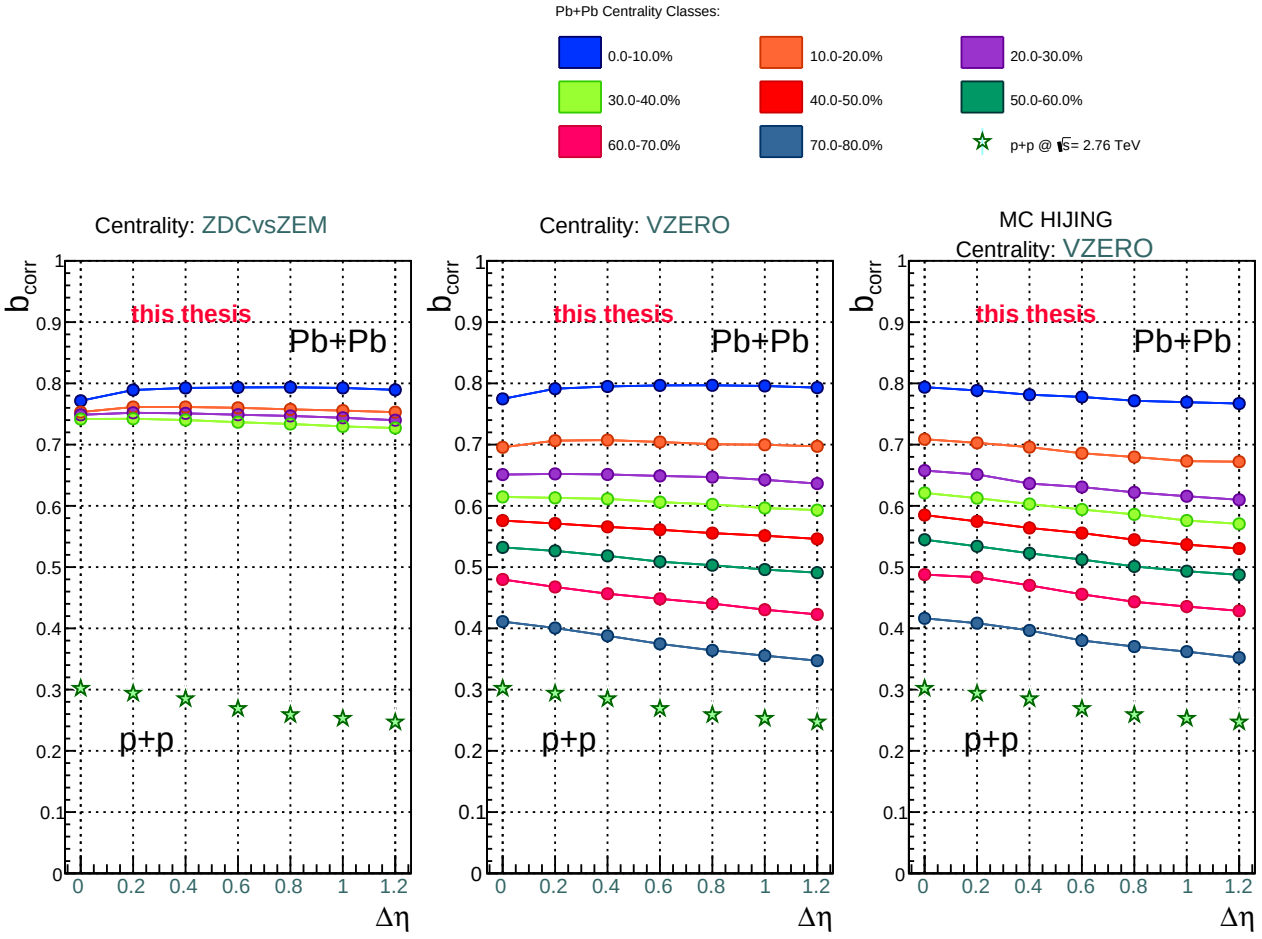

Figure 3.1: The three panel plot presents the value of the correlation coefficient b_{corr} drawn as a function of $\Delta\eta$ measured for Pb+Pb collisions at $\sqrt{s_{NN}} = 2.76$ TeV in ALICE experiment (circles) for 10% width of centrality class. The results for various centrality classes of Pb+Pb collisions, from central to peripheral reactions, are marked by different colors. The left panel shows values for experimental data with ZDCvsZEM while the middle panel for VZERO centrality selection. The right panel presents the results of MC HIJING simulation of Pb+Pb collisions for VZERO centrality estimator. On each of the three panels the same experimental values of forward-backward correlation coefficient obtained for p+p collision at $\sqrt{s} = 2.76$ TeV in the ALICE experiment [20] are plotted (stars). The statistical errors for b_{corr} are below the symbol size.

in $0-10\%$ centrality class. However, it should be remembered that the wider the width of the centrality class interval, the larger the fluctuations of geometry of Pb+Pb collisions (i.e. fluctuations of the number of participants and of the impact parameter) within the centrality class. This in turn is expected to increase particle multiplicity fluctuations. The presence of these latter non-dynamical fluctuations is expected to be responsible for a significant enhancement of the values of forward-backward correlation coefficient measured in wide centrality classes. The behavior of the obtained results on correlation coefficient determined for the ALICE Pb+Pb collision data with VZERO centrality estimator, i.e: (1) the significant decrease of the values with decreasing centrality of lead-lead collision, (2) the flat dependence of b_{corr} on $\Delta\eta$ for most central collisions, (3) the decrease of the correlation strength with increase of $\Delta\eta$ for more peripheral collisions, is qualitatively similar to that observed by the STAR experiment at RHIC, for Au+Au collisions at $\sqrt{s_{NN}} = 200$ GeV. The latter results were also measured for centrality classes of 10% width. In the STAR experiment, the centrality of nucleus-nucleus collisions was estimated based on charged particle multiplicity measurement. The main difference in the analysis performed by STAR and that presented in this thesis is the method used to eliminate the contribution coming from non-dynamical geometry fluctuations discussed above. For the STAR analysis, the corresponding procedure is based on the "profile method", described in [16, 17]. In this thesis the input from such "trivial" effects (like the fluctuation of the number of participants within the selected centrality class) will be reduced by narrowing the width of the centrality bin size.

Correlation strength for the 1% centrality bin width

The Figure 3.2 shows the value of b_{corr} determined for narrow centrality classes of the width of one percent. On each of three panels in the Fig. 3.2 a significant decline in the value of the forward-backward correlation coefficient can be seen, both for the experimental data (left and middle panels) and MC simulations (right panel), in comparison to the results obtained for ten percent centrality bin width (Fig. 3.1). This decrease of the measured value of correlation b_{corr} was to be expected because narrowing the centrality window reduces the fluctuations of Pb+Pb collision geometry within the given centrality class.

The trends observed in the left and middle panels of Figure 3.2 display an evident dependence of the value of b_{corr} on the centrality estimator. When comparing the results between experimental data determined for two different centrality estimators, the decrease of correlation strength is far greater for VZERO than for ZDCvsZEM. For data sample with calorimetric centrality selection (left panel), the measured correlations for Pb+Pb collisions are larger than values of b_{corr} obtained for proton-proton collisions at the same energy per nucleon, contrary to correlation strength determined for VZERO centrality selection (middle panel). In the data sample with ZDCvsZEM centrality estimator there is a visible ordering of the value of correlation coefficient depending on centrality class; the correlation strength decreases with increasing centrality of the collision. This ordering of b_{corr} is reversed when compared to the one observed for the wide 10% centrality class window (Fig. 3.1, left panel). In contrast, for VZERO centrality estimator (middle panel), the value of the correlation coefficient seems to be independent on centrality.

The value of the correlation coefficient in Pb+Pb reactions decreases with increasing distance between forward and backward eta intervals, in particular for VZERO centrality

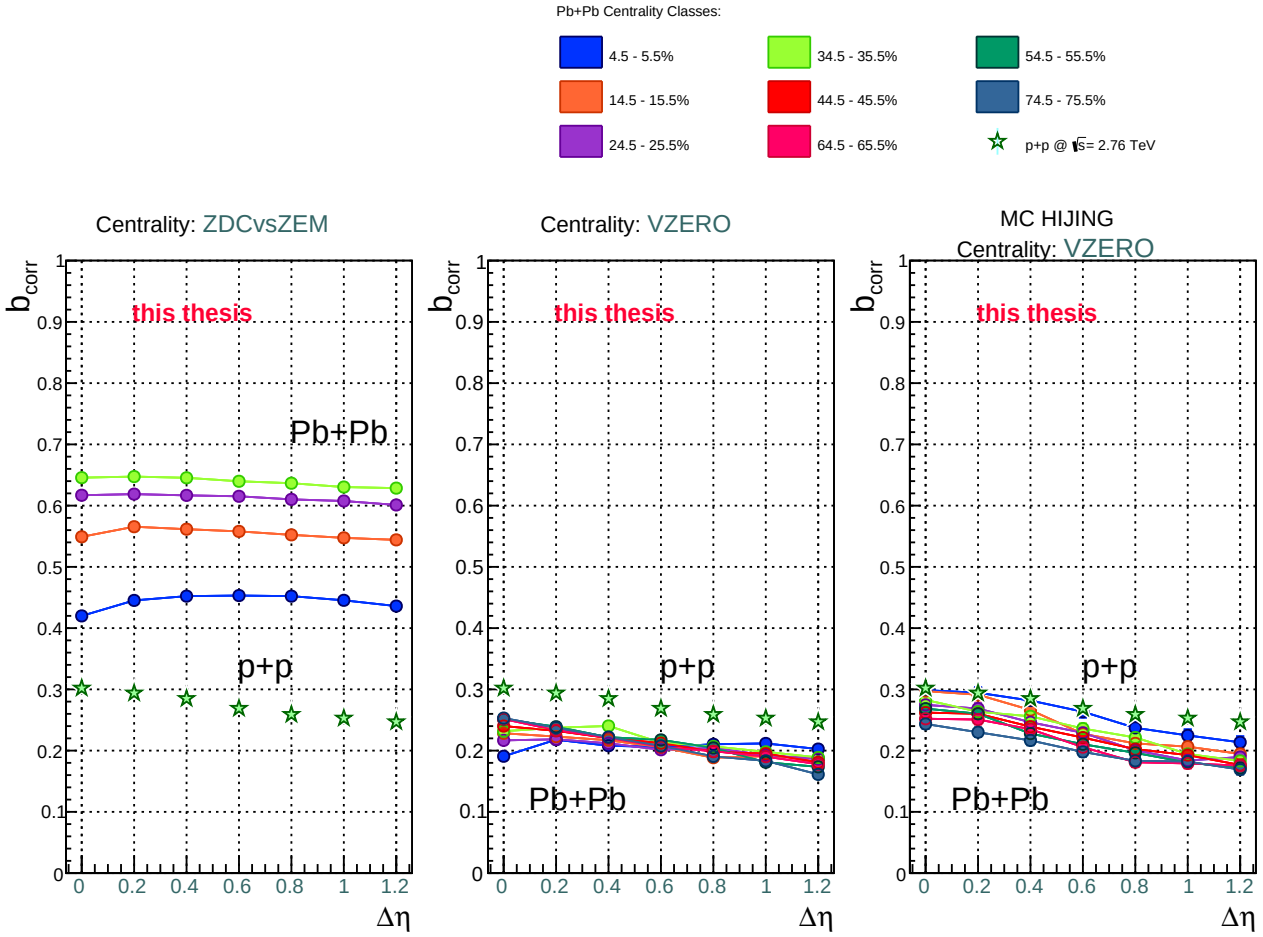

Figure 3.2: The three panel plot presents the value of the correlation coefficient b_{corr} drawn as a function of $\Delta\eta$ measured for Pb+Pb collisions at $\sqrt{s_{NN}} = 2.76$ TeV in ALICE experiment (circles) for 1% width of centrality class. The results for various centrality classes of Pb+Pb collisions, from central to peripheral reactions, are marked by different colors. The left panel shows values for experimental data with ZDCvsZEM while the middle panel for VZERO centrality selection. The right panel presents the results of MC HIJING simulation of Pb+Pb collisions for VZERO centrality estimator. On each of the three panels the same experimental values of forward-backward correlation coefficient obtained for p+p collision at $\sqrt{s} = 2.76$ TeV in the ALICE experiment [20] are plotted (stars). The statistical errors for b_{corr} are below the symbol size.

selection. This is similar to p+p reactions and was seen also for wider centrality windows with the same centrality selection, except for most central collisions.

The results determined from Monte Carlo HIJING simulations of Pb+Pb collisions with centrality selection based on VZERO (right panel) exhibit quite a similar decrease in the value of the correlation coefficient as observed in corresponding physical data (middle panel) when narrowing the centrality class window from ten to one percent. The presumable short-range component of forward-backward correlations determined from Monte Carlo HIJING slightly exceeds what is measured in the experiment. Moreover, the correlation coefficient seems to vary more between different centrality classes for a given $\Delta\eta$ for MC simulations in comparison to the experimental Pb+Pb data with VZERO

centrality selection. The correlation strength calculated based on HIJING simulations decreases almost monotonically with increasing $\Delta\eta$ and the values obtained for central Pb+Pb collisions are in a rough agreement with the experimental result measured in p+p collisions. Again, as for the wide centrality bin of 10% width so for the narrow 1% centrality bin, the decrease of b_{corr} observed in most central collisions of physical data, for both VZERO and ZDCvsZEM centrality estimators, at $\Delta\eta = 0.0$ is not reproduced with Monte Carlo HIJING simulations.

3.2.2 Correlation coefficient b_{corr} as a function of centrality bin width

Figure 3.3 summarizes the information obtained on the value of correlation coefficient b_{corr} determined for Pb+Pb collisions as a function of centrality bin size (ΔCentrality), for one fixed value of the distance between forward and backward pseudorapidity interval, $\Delta\eta = 1.2$.

The presented results reveal following trends in behavior of the values of forward-backward correlation coefficient in relation to centrality bin size:

- On all three panels, a monotonic decrease of the correlation strength with decreasing size of the centrality class interval can be seen, regardless of the chosen centrality estimator;
- Altogether there is a good overall agreement between experimental data with VZERO centrality estimator and results of MC HIJING simulations;
- The dependence of the correlation coefficient as a function of centrality bin size for a given centrality class depends strongly on centrality estimator;
- Left and middle panels of Fig. 3.3 show a similarity between values of forward-backward correlation coefficient measured in the experimental data with calorimetric centrality selection and VZERO centrality estimator for the $0-10\%$ centrality class;
- For the experimental data with both calorimetric and VZERO centrality estimators as well as for the MC HIJING simulation, a saturation-like behavior of correlation coefficient with decreasing centrality bin size can be claimed at least for the less central classes;
- The above saturation-like behavior is always least apparent for the most central Pb+Pb collisions.

The Figure 3.3 is an exemplary plot, setting out the dependence of correlation strength on centrality bin size for the largest distance between forward and backward pseudorapidity intervals available for the present analysis: $\Delta\eta = 1.2$. The changes of correlation coefficient in function of centrality class width for smaller $\Delta\eta$ manifest a similar behavior as presented above.

Remark on influence of centrality estimator

Among all the features the correlation coefficient established by the analysis presented above, it can be said that the most striking is its evidently strong dependence on the

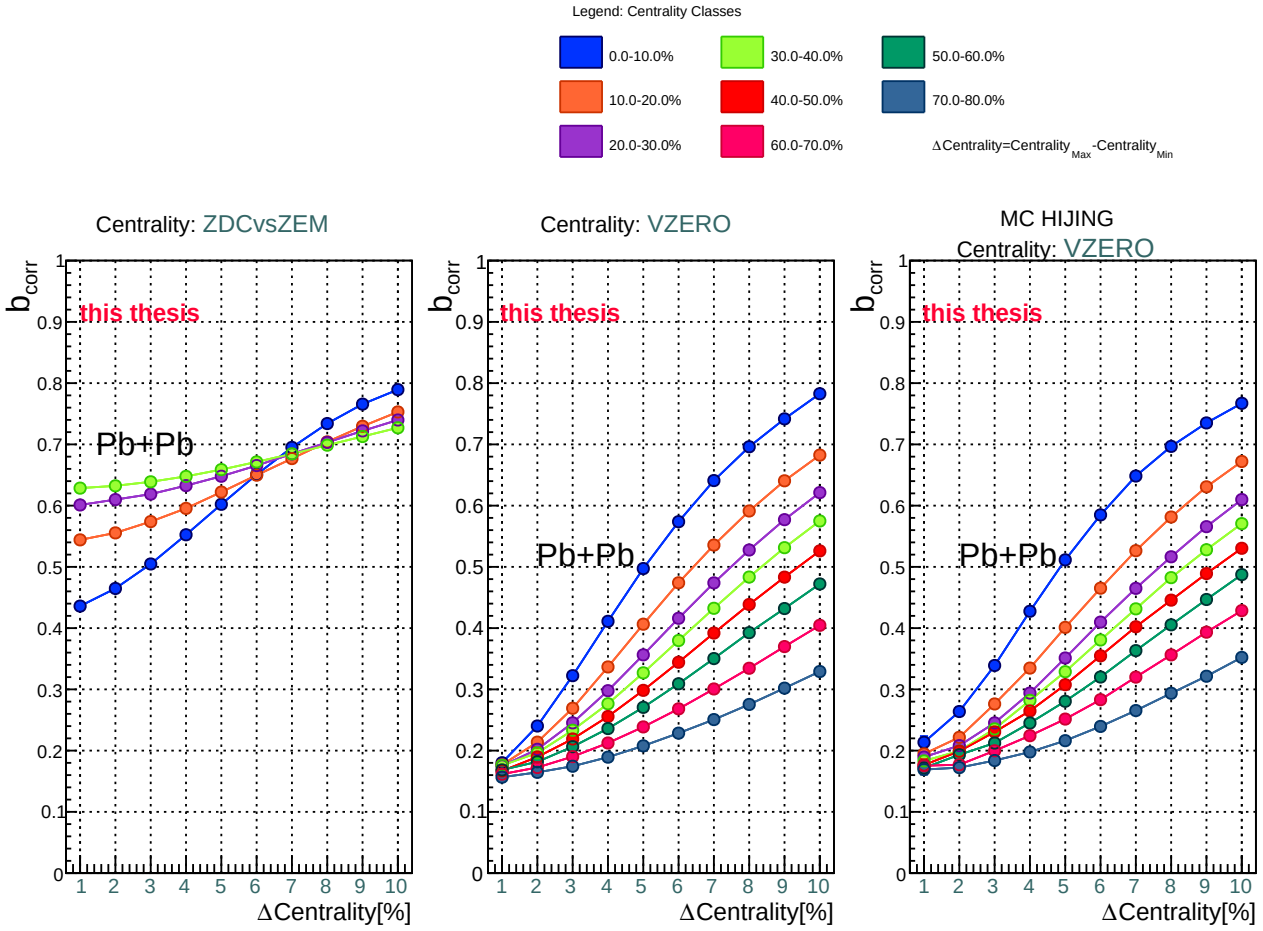

Figure 3.3: The three panel plot presents values of forward-backward correlation coefficient b_{corr} obtained for Pb+Pb collisions at $\sqrt{s_{NN}} = 2.76$ TeV and plotted as a function of the size of centrality class bin for fixed value of pseudorapidity gap $\Delta\eta = 1.2$. The width of centrality class changes from 1% to 10%. The various colors of the data point correspond to different centralities of Pb+Pb collision. The legend (right top corner) assigns colors to centrality class of Pb+Pb collision for the widest centrality window, the ranges of the centrality classes for the narrower class bins are listed in columns of the Table 2.1. Left panel presents values of correlation coefficient determined for experimental data with calorimetric centrality estimator, the middle panel with VZERO centrality estimator. The right panel presents the results of MC HIJING simulation of Pb+Pb collisions for VZERO centrality selection. The statistical errors are drawn on the plot and are smaller than the data point symbols.

centrality estimator used. While this feature cannot be claimed as unexpected on the basis of several existing analyses of this issue [31, 18], several comments are due here.

- While this problem was in principle not present in earlier studies of $e^+ + e^-$ nor p+p interactions, it is clear that the centrality selection procedure significantly influences the measured forward-backward correlations in Pb+Pb collisions. Thus a very high degree of caution and a deep understanding of the methods used for centrality estimation are necessary, whenever comparing data between different experiments or between different estimators.

- In this thesis the observed discrepancies between the values of correlation coeffi-

cient obtained using ZDCvsZEM centrality selection and VZERO centrality estimation are present regardless of the choice of the width of the centrality class interval (Fig. 3.3). Moreover these differences become even more significant when we reduce the contribution from geometrical event-by-event fluctuations, namely for the narrow 1% centrality bins. What appears as particularly puzzling is the behavior of the data with charged multiplicity (VZERO) centrality selection, for which low values of the correlation strength and no dependence on centrality class are apparent in contrast to results obtained with calorimetric centrality selection.

- This problem has evident importance for the present and future understanding of results of correlations studies; it will also show its significance for the fluctuation analysis presented in the subsequent section. According to claims [42], forward-backward correlation studies made with centrality estimation based on charged particle multiplicity (like VZERO selection) should be regarded as a "three-bin" rather then "two-bin" analysis in rapidity space. Calorimetric centrality selection is in principle more directly connected to the number of participating nucleons, but even there extreme caution is suggested in view of the "trivial" fluctuations and correlations in the system size as originating from the "forward-going" and "backward-going" nuclei. Finally, it is to be considered in future studies whether such a strong influence of the VZERO estimator on the presented results does not imply interesting correlations in particle production between VZERO rapidity and the rapidity range considered in the present analysis.

3.3 Intensive quantity omega

This section presents the values of the intensive quantity omega ω, namely the scaled variance, which is the measure of the multiplicity fluctuations. For the symmetric Pb+Pb collision $\omega_{\mathrm{B}} = \omega_{\mathrm{F}}$. Therefore the author focuses on the discussion of the results measured in the selected pseudorapidity intervals (Table 2.2) in backward hemisphere of Pb+Pb reaction, namely ω_{B}. The experimental discrepancy between the scaled variances determined for forward and backward pseudorapidity intervals is typically below 2% for VZERO centrality estimator and below 2.5% for data with ZDCvsZEM centrality selection, in agreement with the systematic errors discussed in Table 3.2.

3.3.1 Multiplicity fluctuation as a function of centrality bin width

The three panel Figure 3.4 shows the values of scaled variance (ω) plotted as a function of centrality bin width (ΔCentrality) in selected pseudorapidity interval $\eta \in [-0.2, 0.0]$. From the comparison between the values obtained for experimental data on Pb+Pb collisions with different centrality estimators and between experimental results and values from Monte Carlo simulations, the following picture emerges:

- The largest values of scaled variance (the largest multiplicity fluctuations) are observed for the widest centrality class windows, where the largest contribution from system size fluctuations is expected;
- The scaled variance decreases with decreasing width of centrality class interval for all centralities of Pb+Pb collisions since narrowing the centrality bin width reduces the input from event-by-event fluctuations of geometry within the selected centrality

Error on ω_B,ω_F	VZERO	ZDCvsZEM, $\Delta\text{Centrality} = 1\%$	ZDCvsZEM, $\Delta\text{Centrality} = 10\%$
typical	2.5%	3%	6%
central $(0-30\%)$ collisions, $\Delta\eta\approx0$, $\Delta\text{Centrality}<5\%$	$3-6\%$		

Table 3.2: Total relative systematic errors estimated for the scaled variance ω_B, ω_F. Apart from typical error values characteristic for most of the obtained data points, one specific region where the corresponding errors are larger than the average is separately considered in the Table. The maximal 6% error value quoted for that region corresponds to the most central Pb+Pb collisions at $\Delta\eta = 0$ and low values of $\Delta\text{Centrality}$.

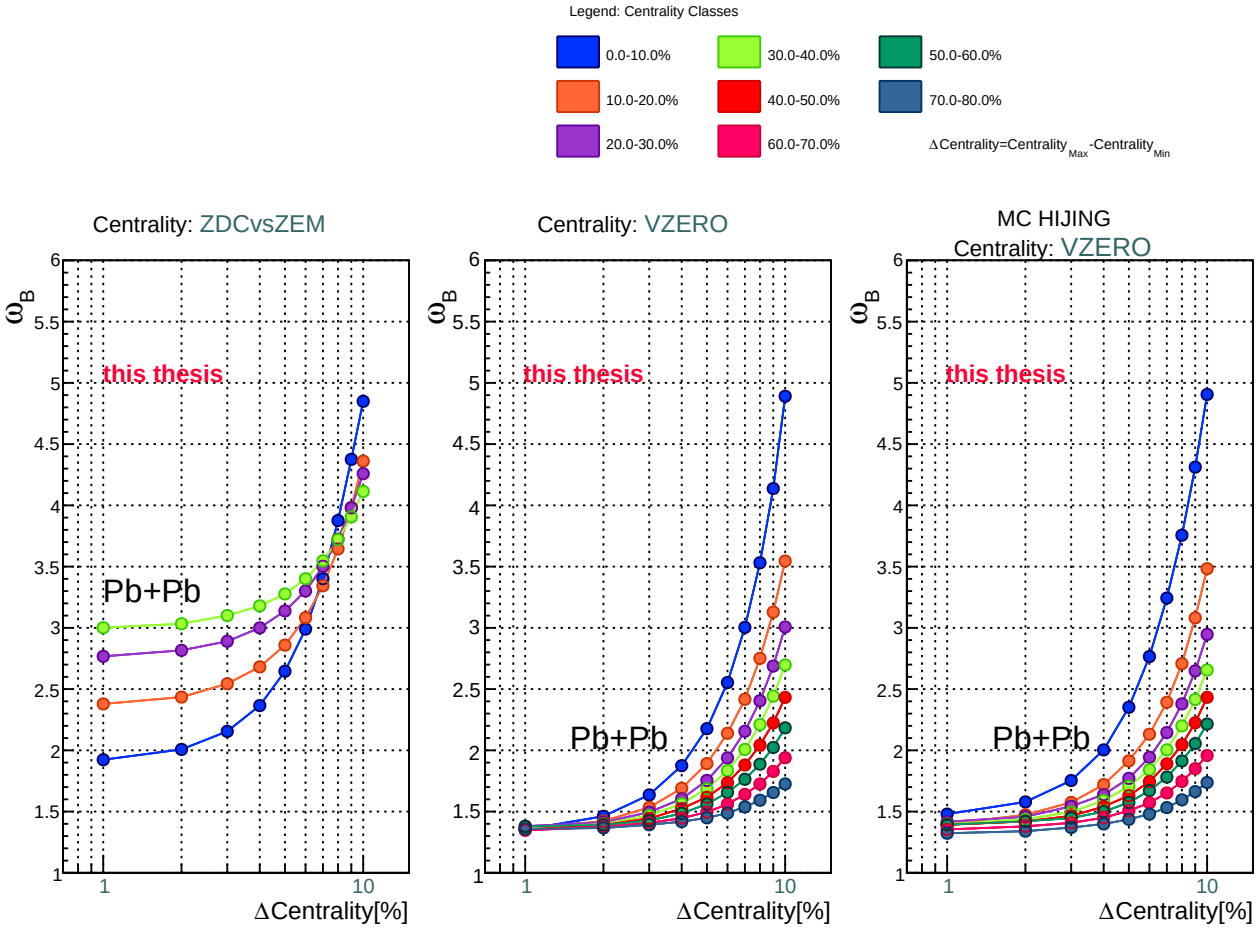

Figure 3.4: The three panel plot presents values of scaled variance ω obtained for Pb+Pb collisions at $\sqrt{s_{NN}} = 2.76$ TeV for particles at pseudorapidity $\eta \in [-0.2, 0.0]$ plotted as a function of the size of centrality class bin. The width of centrality class changes from 1% to 10%. The various colors of the data point correspond to different centralities of Pb+Pb collision. The legend (right top corner) assigns colors to centrality class of Pb+Pb collision for the widest centrality window, the ranges of the centrality classes for the narrower class bins are listed in columns of the Table 2.1. Left panel presents values of scaled variance determined for experimental data with calorimetric centrality estimator, the middle panel with VZERO centrality estimator. The right panel presents the results of MC HIJING simulation of Pb+Pb collisions for VZERO centrality selection. The statistical errors are drawn on the plot and are smaller than the data point symbols.

class;

- The evolution of the value of omega (ω) as a function of the width of centrality class appears to be strongly centrality estimator-dependent. It is different for centrality based on charged particle multiplicity measurement (VZERO, middle panel) or for the calorimetric estimator (ZDCvsZEM, left panel);
- For the results with calorimetric centrality selection, reducing centrality bin size is followed by reorganization of the order of values of scaled variance according to centrality of Pb+Pb collisions. This behavior is not observed for results with VZERO centrality estimator;
- The values of scaled variance saturate with decreasing width of centrality class for data with both calorimetric and VZERO centrality estimators. The measured multiplicity fluctuations become almost independent on the centrality bin size. This can suggest that geometrical fluctuations (i.e fluctuation of number of participants) within the centrality class window have been at least partially eliminated;
- In the region of saturation of the values of multiplicity fluctuations, i.e. for narrowest centrality bin size ΔCentrality $\sim 1\%$, there is a strong dependence of measured scaled variance on centrality class for data with ZDCvsZEM centrality selection. This is not present for data with VZERO centrality estimator, for which multiplicity fluctuations determined for different centrality classes converge to one value and seem to be independent on centrality of the Pb+Pb collision. It can be mentioned that the saturation-like behavior seen in various centrality classes defined with calorimetric centrality estimator (left panel) for ALICE Pb+Pb collisions shows clear similarities to what was observed in the NA49 experiment at $\sqrt{s_{NN}} = 17.3$ GeV [39];
- For the Poisson distribution its variance is equal to its mean value, hence $\omega = 1$. A Poissonian multiplicity distribution indicates independent production of particles, implying no correlations. In the present analysis of Pb+Pb collisions the measured values of the multiplicity fluctuations exceed those given by the Poisson distribution. The scaled variance is greater than one ($\omega > 1$) for each of the two centrality estimators (calorimetric and VZERO) in every studied centrality class of the lead-lead collision, whatever the width of the centrality class is.

  For the narrowest centrality class windows, where the geometrical fluctuations are most suppressed, a substantial deviation from Poissonian fluctuations is still observed for results with ZDCvsZEM centrality selection. Here $\omega = 3.0$ for centrality class $34.5 - 35.5\%$; it decreases with increasing centrality of the collision down to the value $\omega = 1.92$ for most central Pb+Pb reactions ($4.5 - 5.5\%$). The values of scaled variance for data with VZERO centrality estimator at ΔCentrality $= 1\%$ are much lower; they are around $\omega \approx 1.35$ for all centrality classes of Pb+Pb collisions.

Dependence of multiplicity fluctuations on the number of participant nucleons

Figure 3.5 presents the values of scaled variance of charged particle multiplicity distribution, plotted as a function of the number of participating projectile nucleons, obtained for the present analysis (ALICE, this thesis) for the pseudorapidity bin $[-0.2, 0.0]$. The experimental results are presented for both chosen centrality estimators (ZDCvsZEM, VZERO) while the results coming from HIJING are presented only with VZERO centrality selection. In each case the minimum centrality bin width (ΔCentrality $= 1\%$) is

taken for the presented data in order to maximally reduce the inherent geometry fluctuations. The number of participating projectile nucleons is, for the case of the present analysis of symmetric Pb+Pb collisions, simply the number of participants belonging to one incoming nucleus, i.e. $\frac{\mathrm{N_{Total\ Number\ of\ Participants}}}{2}$. For the centrality-selected data samples considered here, this quantity is approximately evaluated on the basis of studies on the Pb+Pb centrality measurement procedure reported by the ALICE Collaboration in [24]. The latter publication gives information about geometrical parameters of the collision (like the average number of participants in corresponding centrality class) from the fit of Negative Binomial Distribution-Glauber to the VZERO signal amplitude. It is to be underlined that possible minor uncertainties in the adaptation of this information to the present analysis do not affect any of the conclusions presented below. The results of the present analysis of Pb+Pb collisions are compared to the value of omega obtained for p+p collisions for the same energy $\sqrt{s} = 2.76$ TeV (see discussion made in Section 2.6.3). Additionally, they are being superimposed with a partially similar analysis of charged particle fluctuations at forward rapidity made by the NA49 experiment at the CERN SPS at $\sqrt{s_{NN}} = 17.3$ GeV, that is, more than two orders of magnitude below in energy [39], together with various model simulations included therein. It should be underlined that unlike for the present analysis, the number of projectile participants obtained for the NA49 analysis was determined based exclusively on the energy of projectile spectators deposited in a forward calorimeter.

Account taken of the relatively weak pseudorapidity dependence of omega as discussed in the next section, the results from the ALICE detector obtained in this thesis and presented in Fig. 3.5 can be claimed as representative for the whole region of central pseudorapidity addressed in this dissertation, namely $-0.8 < \eta < 0.8$. The scaled variance in Pb+Pb collisions at $\sqrt{s_{NN}} = 2.76$ TeV manifests a clear non-monotonic behaviour with increasing system size, with omega increasing very significantly from p+p to least central Pb+Pb collisions ($34.5 - 35.5\%$ centrality), and then slowly decreasing towards most central Pb+Pb reactions. This is contrary to values of scaled variance determined with the VZERO charged multiplicity centrality estimator which appear not to depend on the number of projectile participants. On the other hand, the corresponding NA49 results display a qualitatively very similar non-monotonic behavior as a function of centrality, although quantitative values of scaled variance are smaller at the lower collision energy.

Several comments should be made here. As apparent in Fig. 3.5 and claimed in [39], the non-monotonic centrality-dependence of the scaled variance measured by NA49 escapes interpretation made by means of model simulations included therein. There exist two independent explanations, at least known to the author at the moment of writing this thesis, that have been proposed to interpret this non-monotonic change of multiplicity fluctuations with centrality. In the first scenario [39, 40] it is postulated that the origin of this characteristic dependence of scaled variance on the system size might be the correlations between produced particles. In order to reproduce the observed behavior those correlations should be positive at small distances (attractive interaction) and negative at larger ones (repulsive interaction). Hypotheses for such mechanisms are presented in [40]. Even if criticized as being to some extent *ad hoc* [42], it is worthwhile to mention that one such interpretation would claim that the effect would arise from superposition of two potentials: electrostatic (Debye potential) and nuclear (Yukawa potential).

Other possible explanations have been discussed in [41], including in particular different degrees of mixing in longitudinal phase space. Monte Carlo studies imply that

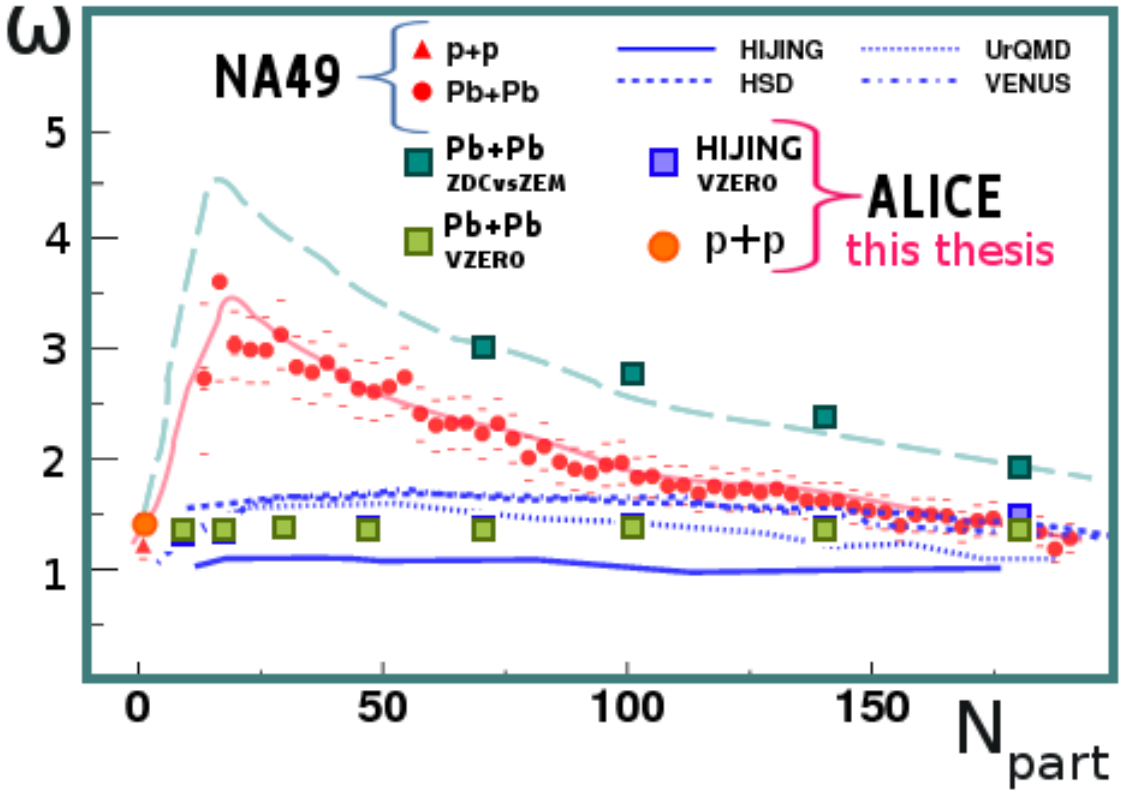

Figure 3.5: The scaled variance of the charged particle multiplicity distribution plotted as a function of the number of participating projectile nucleons ($\mathrm{N_{part}}$). The figure compares values of ω obtained in the ALICE experiment and the NA49 experiment. **ALICE**: the figure shows results for Pb+Pb collisions at $\sqrt{\mathrm{s_{NN}}} = 2.76$ TeV determined for the pseudorapidity bin $\eta \in [-0.2, 0.0]$ for centrality classes of 1% centrality bin width. The experimental results for Pb+Pb collisions are presented for two centrality estimators: ZDCvsZEM (dark green squares) and VZERO (light green squares), while the results of MC HIJING simulations are shown only for VZERO centrality selection (light blue squares). The data points for MC HIJING overlap with these presenting experimental values determined with VZERO centrality selection. The estimated result for scaled variance of the multiplicity distribution in p+p collisions at $\sqrt{\mathrm{s}} = 2.76$ TeV is marked with an orange circle. Systematic and statistical errors are smaller than data point markers. **NA49**: The results for NA49 were redrawn from [39]. The plot shows the scaled variance of multiplicity distribution obtained for Pb+Pb (red circles) and p+p (red triangle) collisions at energy $\sqrt{\mathrm{s_{NN}}} = 17.3$ GeV. Experimental results were measured in forward rapidity interval $1.1 < \mathrm{y_{c.m.}} < 2.6$. The centrality of presented data sample of NA49 Pb+Pb collisions was determined based on energy of projectile spectators deposited in calorimeter. The experimental results are compared to Monte Carlo simulations of NA49 events (blue lines). On the plot dashed light blue and pink curves serve to guide the eye.

fluctuations in the number of target participants for fixed projectile participants strongly and non-monotonically depend on the centrality of the collision which results in strong dependence of multiplicity fluctuations on the system size in target hemisphere and weak

in projectile hemisphere. The interpretation of the non-monotonic dependence of multiplicity fluctuations measured in NA49 experiment in forward rapidity interval in terms of the transport models might suggest stronger mixing between longitudinal flows of the projectile and target production sources than previously assumed.

It would be premature to make any firm claim on the basis of the evidently suggestive similarity of the non-monotonic behaviour of omega with centrality for the present analysis and for the NA49 experiment, in particular also by practical reasons like different particle rapidity range and different approach to centrality estimation. It is nevertheless tempting to consider whether this similarity could be an indication of similar processes at work over a factor of 160 in c.m.s. collision energy, and a possible hint on correlations between produced particles at the LHC. The author leaves this issue to further theoretical studies and detailed model simulations.

3.3.2 Multiplicity fluctuations as a function of pseudorapidity

Figures 3.6 and 3.7 show the dependence of the measured values of scaled variance (ω_{B}) of charged particle multiplicity distributions on particle pseudorapidity. On the presented plots the results for intensive quantity ω_{B} are drawn as a function of $\Delta\eta$, where each value of eta gap corresponds to a pseudorapidity interval of a width $\delta\eta = 0.2$ and range $\eta \in [-\frac{\Delta\eta}{2} - \delta\eta, -\frac{\Delta\eta}{2}]$ in the backward hemisphere of the collision (see also Table 2.2).

Fig. 3.6 corresponds to the width of the centrality bin being equal to ΔCentrality = 10%, while Fig. 3.7 to ΔCentrality = 1%. The measured value of ω_{B} is roughly constant as a function of pseudorapidity for a given class of centrality of Pb+Pb collisions. This is valid for experimental data determined for both calorimetric and VZERO centrality estimators, irrespective of the width of centrality class. The only exceptions are the values of physical results for 0−10% centrality Pb+Pb collisions, for which scaled variance increases by no more than about 7% with increasing pseudorapidity. Monte Carlo HIJING simulations describe well the behavior of the experimental data for VZERO centrality selection at ΔCentrality = 10%, excluding the most central collisions for which MC values of scaled variance remain constant as a function of pseudorapidity, while the data exhibit an increase with $\Delta\eta$. The situation is somewhat less clear for ΔCentrality = 1%.

A detailed comparison of Figure 3.1 with Figure 3.6, as well as Figure 3.2 with Figure 3.7, respectively, shows a clear similarity in the behavior of the scaled variance as a function of centrality class and size of centrality bin (but also in reference to results estimated for p+p reactions) with what was observed for the correlation coefficient in Section 3.2.1.

3.4 Strongly intensive quantity sigma

This section is dedicated to results obtained for ALICE Pb+Pb collisions on the strongly intensive quantity sigma (Σ). As explained in the introduction (Section 1.4), the advantage of measuring Σ is that this observable does not depend on system size nor on system size fluctuations. Sigma Σ is defined by a combination of selected characteristics of multiplicity distributions measured in a pair of forward-backward pseudorapidity intervals (Eq. 1.22) which for symmetric collisions, like p+p and Pb+Pb reactions discussed here, reduces to formula $\Sigma = \omega(1 - \mathrm{b}_{\mathrm{corr}})$ expressing the interplay between the information

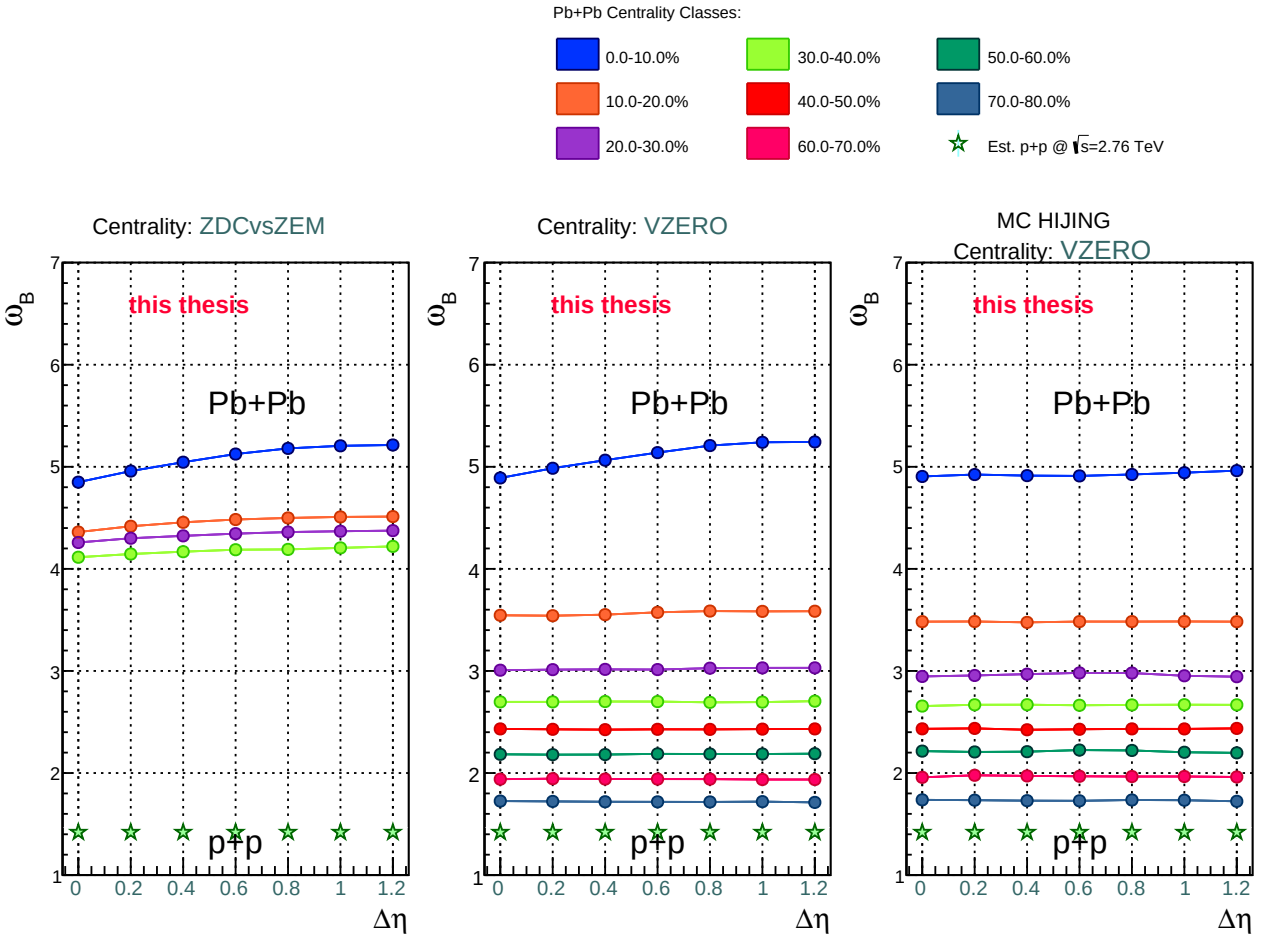

Figure 3.6: The three panel plot presents the value of the scaled variance as a function of $\Delta\eta$ measured for Pb+Pb collisions at $\sqrt{s_{NN}} = 2.76$ TeV in ALICE experiment (circles) for 10% width of centrality class. Results are presented for the values of scaled variance obtained in the pseudorapidity intervals of the backward hemisphere of Pb+Pb collisions, namely ω_B. On the figure the results for various centrality classes of Pb+Pb collisions, from central to peripheral reactions, are marked by different colors. The first two panels show values for experimental data for two different centrality estimators: the left panel for ZDCvsZEM, the middle panel for VZERO. The right panel presents the results of MC HIJING simulation of Pb+Pb collisions for VZERO centrality selection. On each of three panels the experimental values of respectively b_{corr}, ω_B and Σ for Pb+Pb collisions were compared to the same estimated values of scaled variance in p+p collision at $\sqrt{s} = 2.76$ TeV (stars). The statistical errors are drawn in the plot and are below the symbol size, as well as uncertainties of the estimation of the values of ω in p+p reactions.

carried by omega and b_{corr}. Bearing in mind that values of scaled variance determined in this thesis seem to be approximately constant in the studied pseudorapidity range (Section 3.3.2), it can be expected that the strongly intensive quantity sigma will be sensitive mostly to the changes of b_{corr} as a function of pseudorapidity.

Figure 3.8 presents the values of sigma as a function of the distance between forward and backward pseudorapidity intervals $\Delta\eta$ for ten percent centrality bin width. From the comparison between values presented on the left and middle panels, one can see that

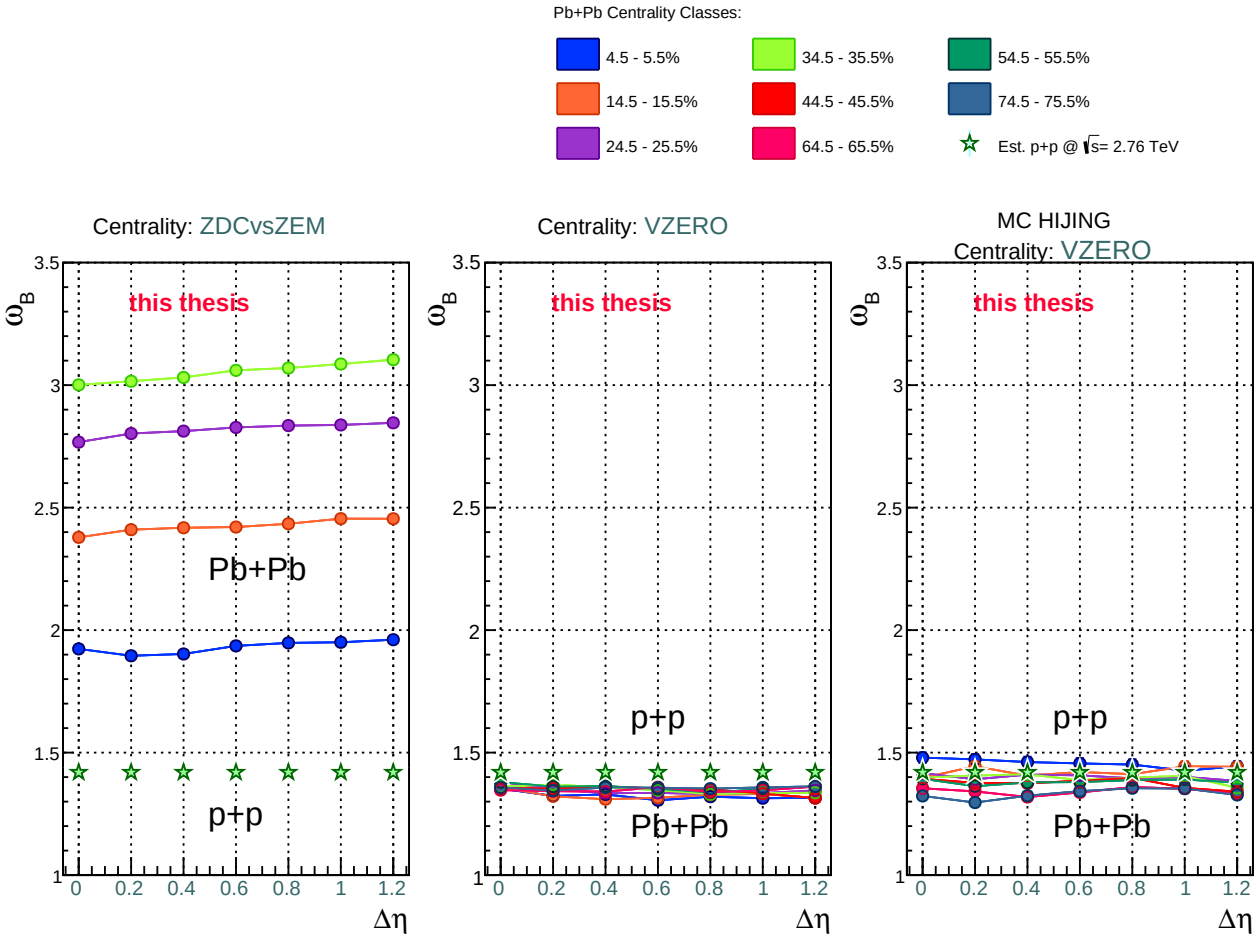

Figure 3.7: The three panel plot presents the value of the scaled variance as a function of $\Delta\eta$ measured for Pb+Pb collisions at $\sqrt{s_{NN}} = 2.76$ TeV in ALICE experiment (circles) for 1% width of centrality class. Results are presented for the values of scaled variance obtained in the pseudorapidity intervals of the backward hemisphere of Pb+Pb collisions, namely ω_B. On the figure the results for various centrality classes of Pb+Pb collisions, from central to peripheral reactions, are marked by different colors. The first two panels show values for experimental data for two different centrality estimators: the left panel for ZDCvsZEM, the middle panel for VZERO. The right panel presents the results of MC HIJING simulation of Pb+Pb collisions for VZERO centrality selection. On each of three panels the experimental values of ω_B for Pb+Pb collisions were compared to the same estimated values of scaled variance in p+p collision at $\sqrt{s} = 2.76$ TeV (stars). The statistical errors are drawn in the plot and are below the symbol size, as well as uncertainties of the estimation of the values of ω in p+p reactions.

there is no significant qualitative nor quantitative difference between results for data with calorimetric centrality selection (left panel) and for centrality based on multiplicity measurement (middle panel). Thus the measured values appear basically independent of centrality estimator. This confirms, on the practical example of the present analysis, the applicability of Σ as a strongly intensive quantity.

The principal effect apparent in Figure 3.8 is the growth of the strongly intensive quantity Σ in Pb+Pb collisions with increasing η gap between forward and backward pseudorapidity intervals (for all the three panels). This behavior is at least partially

similar to what is observed for the estimated values of Σ in p+p collisions.

The quantity Σ is normalized in such a way that it becomes equal to one in case of no correlation between produced particles. The obtained experimental values and results of Monte Carlo HIJING simulation are greater than one ($\Sigma > 1$) across all pseudorapidity phase-space covered in this analysis, for all centrality classes of Pb+Pb collisions. They also surpass the estimated results for Σ in p + p reactions.

The ordering of the values of Σ as a function of the centrality class – the more central collision the smaller value of the strongly intensive quantity – is observed to be the same for data with two different centrality estimators, namely VZERO and ZDCvsZEM. From the comparison of Figure 3.8 with Figures 3.1 and 3.6 results that the ordering of the values of Σ with centrality classes is consistent with the behavior seen for physical results on the correlation coefficient b_{corr} and the scaled variance ω in narrow centrality class bins (ΔCentrality = 1%) of lead-lead collisions, but only for data with calorimetric centrality selection. For Σ ordering of the values with centrality of Pb+Pb collisions is more evident for larger values of pseudorapidity gap.

It is worth to point out here, that some phenomenological models predict ordering of the values of long-range correlation with centrality; in the Color Glass Condensate model the magnitude of correlation strength should increase with centrality of the collision [30], a contrary scenario is provided by string percolation models where a decrease of values of forward-backward correlations is expected for more central collisions [48] (see also discussion in Section 1.3.3 and references therein). From the latter, and on the basis of the following facts:

(a) the strongly intensive quantity Σ in the framework of Independent Source Model does not depend on geometry fluctuations, it is sensitive to the fluctuations arising from a single source (like one wounded nucleon),

(b) sigma carries information which is an interplay of the signals from particle correlations and multiplicity fluctuations,

(c) there is a consistency in ordering with centrality class, observed between sigma, b_{corr} and ω with calorimetric centrality selection,

the following question arises: could the same ordering observed in values of sigma Σ and in values of b_{corr} and ω, as a function of centrality class have the same origin? Might this ordering of the values of measured quantities with centrality be a signal of some universal mechanism related, for example, to the dynamics of the reaction or it is caused by more "trivial" effects related for instance to the centrality estimation method? Why the ordering is not observed explicitly for results on b_{corr} and on ω for the data with VZERO centrality estimator, but is present for the values of the strongly intensive quantity Σ obtained for the data with VZERO centrality selection? These questions open the door for further analysis.

From the comparison of the values of sigma Σ measured in ALICE experiment (Fig. 3.8 and Fig. 3.9, middle panel) to those determined from the Monte Carlo simulations (Fig. 3.8 and Fig. 3.9, right panel), it results that the HIJING Monte Carlo simulation describes the experimental data reasonably well. There are three main differences between the MC model and the experimental data worth mentioning:

Error on Σ	VZERO	ZDCvsZEM, $\Delta\text{Centrality} = 1\%$	ZDCvsZEM, $\Delta\text{Centrality} = 10\%$
typical	2.5%	2%	3%
central $(0-20\%)$ and peripheral $(70-80\%)$ collisions, $\Delta\eta\approx 0$	$4-7\%$		

Table 3.3: Total systematic errors estimated for the strongly intensive Σ variable. Apart from typical error values characteristic for most of the obtained data points, two specific regions where the corresponding errors are larger than the average are considered in the table. The maximal 7% error value quoted therein for that region corresponds to the most central Pb+Pb collisions at $\Delta\eta = 0.0$.

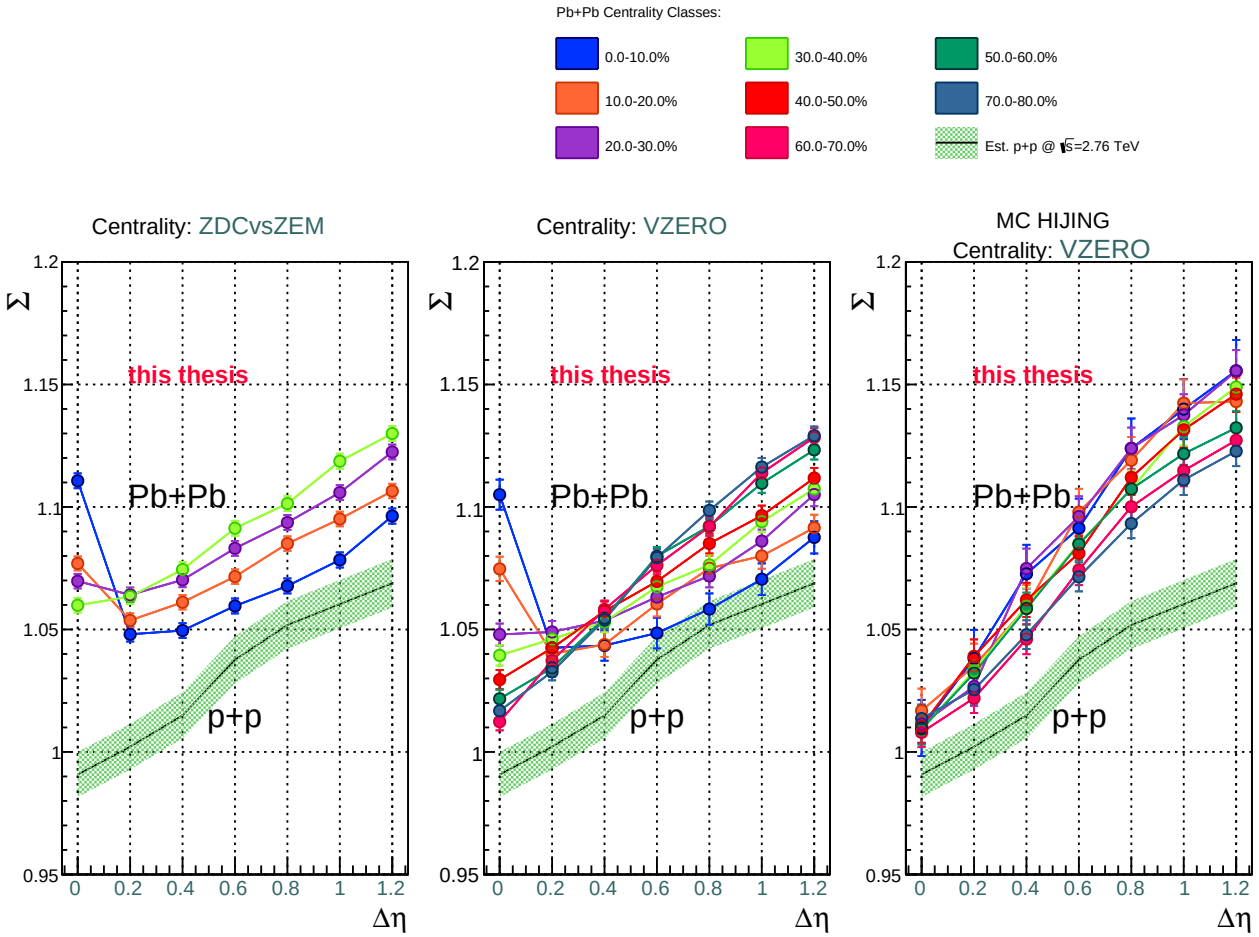

Figure 3.8: The value of the strongly intensive quantity sigma Σ obtained for Pb+Pb collisions at $\sqrt{s_{NN}} = 2.76$ TeV in the ALICE experiment (circles) for 10% width of centrality class, plotted as a function of $\Delta\eta$. In the figure, the results for various centrality classes of Pb+Pb collisions, from central to peripheral reactions, are marked by different colors. The first two panels show values for experimental data for two different centrality estimators: the left panel for ZDCvsZEM, the middle panel for VZERO. The right panel presents the results of MC HIJING simulation of Pb+Pb collisions for VZERO centrality selection. On each of the three panels, the values of Σ obtained for Pb+Pb collisions were compared to the same estimated values of strongly intensive quantity sigma in p+p collisions at $\sqrt{s} = 2.76$ TeV (black line). The statistical errors for Σ are plotted in the same figure as the data points. Uncertainties of the estimation of the values of Σ in p+p collisions are marked with a green shaded area.

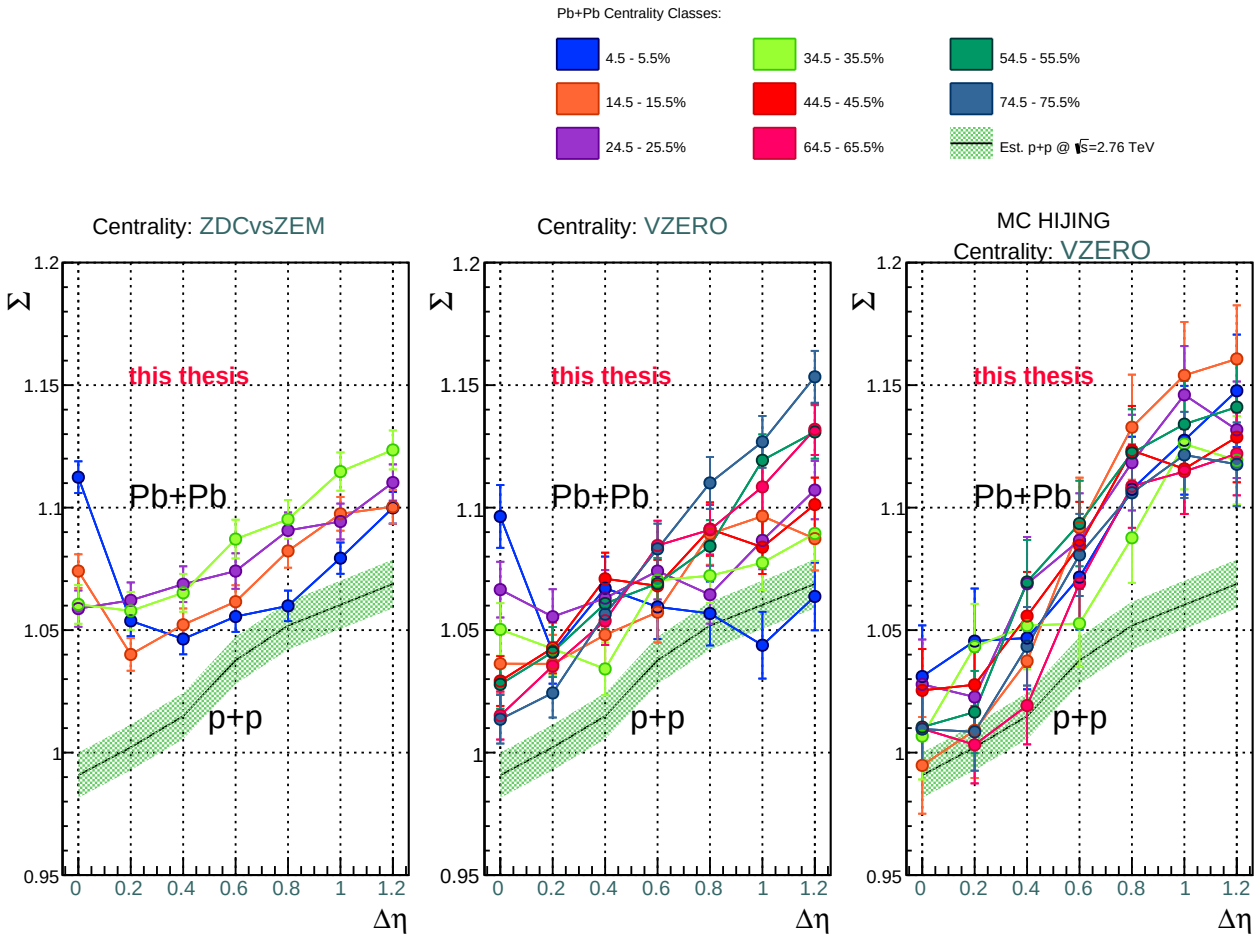

Figure 3.9: The value of the strongly intensive quantity sigma Σ obtained for Pb+Pb collisions at $\sqrt{s_{NN}} = 2.76$ TeV in the ALICE experiment (circles) for 1% width of centrality class, plotted as a function of $\Delta\eta$. In the figure, the results for various centrality classes of Pb+Pb collisions, from central to peripheral reactions, are marked by different colors. The first two panels show values for experimental data for two different centrality estimators: the left panel for ZDCvsZEM, the middle panel for VZERO. The right panel presents the results of MC HIJING simulation of Pb+Pb collisions for VZERO centrality selection. On each of three panels, the values of Σ obtained for Pb+Pb collisions were compared to the same estimated values of strongly intensive quantity sigma in p+p collisions at $\sqrt{s} = 2.76$ TeV (black line). The statistical errors for Σ are plotted in the same figure as data points. Uncertainties of the estimation of the values of Σ in p+p collisions are marked with a green shaded area.

- the values for the strongly intensive quantity Σ obtained from the simulations of Pb+Pb collisions seems to increase steeper with the growth of pseudorapidity gap ($\Delta\eta$) than those measured in physical Pb+Pb collisions; this behavior also results in apparently larger deviations of MC HIJING results from the estimated values of Σ in the p+p collisions;
- there is a no clear dependence of the values of the strongly intensive quantity sigma on centrality classes seen for Monte Carlo simulations;
- there is an increase of the value of sigma for small pseudorapidity gap $\Delta\eta = 0.0$ present for the experimental data with calorimetric and VZERO centrality selection

which is not observed in Monte Carlo results. The disagreement between values of Σ obtained for MC and experimental data at $\Delta\eta = 0.0$ in most central collisions is observed also for the values of the correlation coefficient (Fig. 3.2) and suggest that some short-range effects present in physical Pb+Pb collisions might not be reproduced by Monte Carlo HIJING simulations. However, the systematic errors are relatively large for central collisions at $\Delta\eta = 0.0$, therefore the behavior of the data points in this kinematic region must be interpreted with caution.

Figure 3.9 presents the values of the strongly intensive quantity Σ, plotted as a function of $\Delta\eta$ for the narrow centrality class interval of a width 1%. There are no significant differences in the behavior observed for sigma Σ between the results obtained for 10% and 1% centrality bin width, both for the experimental data and for Monte Carlo HIJING simulations.

Altogether, the results of measurement of values of Σ in Pb+Pb collisions at $\sqrt{s_{NN}} = 2.76$ TeV show that this observable is insensitive to centrality bin size and to the method used for centrality class selection (centrality estimator) in the experiment. Indeed it exhibits the behavior characteristic for a strongly intensive quantity in terms of the Independent Source Model.

CHAPTER 4

Summary and outlook

This chapter constitutes an attempt to summarize the experimental results obtained in this thesis. A first set of conclusions as well as emerging questions are presented as well.

1. New experimental information has been obtained on the forward-backward correlation coefficient b_{corr}, the intensive quantity ω and the strongly intensive quantity Σ in Pb+Pb collisions at the energy $\sqrt{s_{NN}} = 2.76$ TeV recorded by the ALICE experiment at the CERN LHC. The observables b_{corr}, ω, and Σ were studied for charged particle multiplicity distributions in two symmetric pseudorapidity windows, as a function of pseudorapidity gap, collision centrality and centrality bin width. The analysis of Pb+Pb collisions was carried out for two centrality estimators using different observables to determine the initial geometry of Pb+Pb collisions, namely: (a) the ZDCvsZEM estimator for which centrality was defined through the energy of the spectator system deposited in the calorimeter (in a somewhat naive picture directly related to the number of participant nucleons), and (b) the VZERO estimator providing the information about centrality based on measurement of charged particle multiplicity.

2. A strong dependence of the measured magnitude of forward-backward correlation, and of the size of multiplicity fluctuations, is observed as a function of the applied centrality estimator and as a function of the size of centrality window. A dominant impact of geometrical fluctuations on the values of b_{corr} and ω is evident for wide centrality class windows. The measured strength of correlations and size of multiplicity fluctuations decreases significantly when reducing the width of centrality class bin. For narrow centrality classes, the values of scaled variance and the correlation coefficient become almost independent on the centrality bin size, for data with both calorimetric and VZERO centrality estimators. This saturation-like behavior can suggest that such geometrical fluctuations have been at least partially eliminated for most narrow centrality classes considered here. For this analysis of Pb+Pb collisions at ALICE energies, the Σ observable exhibits the properties of a strongly intensive quantity in terms of the Independent Source Model. It has been verified that the obtained values of Σ do not depend on centrality estimator and are basically insensitive to geometrical fluctuations.

3. Even after suppression of the contribution from geometrical fluctuations in narrow centrality class intervals, the measured values of multiplicity fluctuations defined by the scaled variance ω exceed Poissonian fluctuations ($\omega > 1$). The deviation from the inde-

pendent emission scenario is also observed for Σ in all the analyzed pseudorapidity range. This behavior suggests the presence of correlation phenomena acting on short and long ($\Delta\eta > 1$) pseudorapidity range, of a different origin than geometrical fluctuations. For ω a substantial deviation from Poissonian fluctuations is observed for results with ZDCvsZEM centrality selection.

4. Clearly, further studies need to be performed to determine the precise contribution coming from geometrical fluctuations, and to extract more complete information about dynamical correlations. A natural extension of the presented study is to analyze the correlation coefficient and the scaled variance in the context of fluctuation of number of sources (like number of participant nucleons) in terms of the Independent Source Model. Such an analysis is currently in the implementation phase in the framework of Monte Carlo EPOS simulations [49]. Particularly interesting seems to extract information about forward-backward correlation strength emerging from a single source in Pb+Pb reactions and to compare it to results from elementary p+p collisions.

5. A limitation for the present study was the lack of detector corrections for results obtained with the ZDCvsZEM centrality estimator. These corrections are planned to be applied in a subsequent, more refined analysis. However, the contribution to the systematic error due to the absence of these corrections was carefully evaluated. Based on the latter evaluation the author concludes that the lack of detector corrections to be applied in this part of the analysis does not change the conclusions arising from this work.

6. In general as a function of pseudorapidity, the values of the correlation coefficient measured for Pb+Pb collisions reveal a slight decrease with increasing distance between forward and backward pseudorapidity intervals ($\Delta\eta$), regardless of the centrality estimator and centrality bin size. This behavior is interpreted as a drop of the short range component of the correlation coefficient and it is with agreement to what was observed in other experiments (like STAR) as well as in p+p collisions. The magnitude of the multiplicity fluctuations ω for each centrality class is quite constant as a function of pseudorapidity, while the values of the strongly intensive quantity Σ increase with increasing pseudorapidity gap.

7. Another limitation of the presented analysis was the narrow pseudorapidity coverage of the ALICE TPC detector, $-0.8 < \eta < 0.8$. In order to examine long-range correlations in a wider pseudorapidity range as well as in more than two pseudorapidity intervals, in the future the extension of the present analysis to new information obtained from other ALICE detectors should be considered.

8. Another area of future research is to study b_{corr} not only as a function of the pseudorapidity gap $\Delta\eta$ but also of the gap in azimuthal angle $\Delta\phi$.

There are also several questions resulting from this analysis which remain still unanswered and require further studies:

- The values of scaled variance of charged particle multiplicity distribution deter-

mined for Pb+Pb data with calorimetric centrality selection manifest a clear non-monotonic dependence on centrality of the collision. Such behavior is in not seen for the Pb+Pb data with VZERO (charged multiplicity) centrality estimator, for which values of scaled variance do not depend on the centrality . A similar non-monotonic dependence of the scaled variance on system size was measured by the NA49 experiment. What is the origin of this non-monotonic dependence of scaled variance of multiplicity distribution on centrality? Might the mechanisms responsible for the non-monotonic behavior of ω As a function of centrality observed in NA49 and ALICE data be the same in spite of the very large difference in collision energy? Could this possibly be a hint for correlations between produced particles as postulated for the case of SPS data?

- An extremely strong dependence of the values of the correlation coefficient and of multiplicity fluctuations on the VZERO with respect to ZDCvsZEM centrality estimator is observed. It should be tested whether this behavior could emerge from correlations in particle production between VZERO rapidity and the rapidity range considered in the present analysis.

- For narrow centrality classes the values of the correlation coefficient b_{corr} and the scaled variance ω are the smaller the central the collision is - for Pb+Pb data with ZDCvsZEM centrality selection. The same ordering of the values is observed for the strongly intensive quantity Σ, regardless of the chosen centrality selection. Does the same ordering observed for values of b_{corr} and ω as a function of centrality class have the same origin? Might this ordering be a signal of some mechanism related to the dynamics of the reaction or is it caused by more "trivial" effects related for instance to the centrality estimation method? Why the ordering is not observed explicitly for results on b_{corr} and on ω for the data with VZERO centrality estimator but it is present for the values of the strongly intensive quantity obtained for the data with VZERO centrality selection?

The work presented in this dissertation is the first analysis known to the author that provides accumulated information on, simultaneously, the forward-backward correlation coefficient, the multiplicity fluctuation and the strongly intensive quantity sigma obtained at the LHC energy scale, not only as a function of centrality bin size but also for two different types of centrality estimators and for several pseudorapidity intervals in the forward and the backward hemisphere of Pb+Pb collisions. The estimation of values of ω and Σ for p+p collisions allowed a complete, and at the moment unique, comparative study of the above results in Pb+Pb collisions at $\sqrt{s_{NN}} = 2.76$ TeV with elementary proton-proton reactions at the same energy. In the opinion of the author, the major advantage of this work was this simultaneous study of these three different quantities, as each of them appears to carry a complementary information on particle correlations and multiplicity fluctuations in heavy ion collisions.

Acknowledgements

I would like to express my deepest gratitude to my supervisor Andrzej Rybicki. Thank you Andrzej for introducing me to the field of heavy ion physics, for your inspiring guidance and for continuous support of my Ph.D study and research, and knowledge you shared with me. I appreciate immensely your help and patience in correcting and bringing this thesis to its final version. Thank you your for kindness and understanding. Work with you since my master studies formed me as a scientist. I hope that one day I will be as good a physicist as you are.

My sincere thanks also goes to Marek Kowalski for his friendly encouragement, support and invaluable advice at every stage of the work presented in this thesis. Thank you Marek for always believing in me and for allowing me to fulfill one of my dreams – working at CERN.

None of this work would have been possible without help from my secondary supervisor Christoph Mayer. Thank you Chris for your patience while introducing me to the ALICE software, and for your help and advice in the data analysis process.

I have been lucky to work with an amazing research group and most friendly people at the Department of Ultrarelativistic Nuclear Physics and Hadronic Interactions (NZ23). I would like to express my warmest thanks to all my colleagues in the department for their support and for creating a joyous workplace by their daily attitude.

I would like to thank my family for their love, for giving me the opportunity and endless moral encouragement to follow my dreams. Especially I want to thank my aunt, this thesis would have never been written if not you.

I am indebted to all my friends for their understanding, support, patience and not abandoning me.

Last but not least I want to thank my cat Parys for always cheering me up, even though he probably will not appreciate it.

This work was supported by the National Science Centre, Poland
(grants no. 2014/14/E/ST2/00018 and 2013/08/M/ST2/00598).

Bibliography

[1] W. Florkowski *Phenomenology of Ultra-relativistic Heavy-ion Collisions*,World Scientific, (2010)

[2] W. Braunschweig *et al.* [TASSO Collaboration], Z. Phys. C **45** (1989) 193.

[3] R. Akers *et al.* [OPAL Collaboration], Phys. Lett. B **320** (1994) 417.

[4] P. Abreu *et al.* [DELPHI Collaboration], Z. Phys. C **52** (1991) 271.

[5] V.V. Aivazian *et al.* [NA22 Collaboration], Z. Phys. C **42** (1989) 533.

[6] V. V. Aivazian *et al.* [NA22 Collaboration], Z. Phys. C **42**, 533 (1989).

[7] S. Uhlig, I. Derado, R. Meinke, H. Preissner Nuc. Phys. B **132** (1978) 15

[8] K. Alpgard *et al.* Phys. Lett. B **123** (1983) 5, 361

[9] T. Alexopoulos *et al.* [E735 Collaboration], Phys. Lett. B **353** (1995) 155.

[10] G.A. Feofilov,R.S. Kolevatov ,V.P. Kondratiev ,P.A. Naumenko ,V.V. Vechernin [NA49 collaboration] Proc. XVII ISHEPP, JINR, vol.1 (2005) 222-231

[11] S. Ahmad, A. Khatun, S. Khan, A. Ahmad and M. Irfan, Adv. High Energy Phys. **2015**, 615458 (2015)

[12] B. K. Srivastava, Eur. Phys. J. A **31**, 862 (2007)

[13] B. K. Srivastava [STAR Collaboration], Int. J. Mod. Phys. E **16**, 3371 (2007)

[14] T. J. Tarnowsky, *Long-Range Multiplicity Correlations in Relativistic Heavy-Ion Collisions and the Signal for Dense Partonic Matter* Ph.D. Thesis, Purdue University (2008)

[15] T. J. Tarnowsky [STAR Collaboration],

[16] B. I. Abelev *et al.* [STAR Collaboration], Phys. Rev. Lett. **103**, 172301 (2009)

[17] S. De, T. Tarnowsky, T. K. Nayak, R. P. Scharenberg and B. K. Srivastava, Phys. Rev. C **88**, no. 4, 044903 (2013)

[18] Y. L. Yan, D. M. Zhou, B. G. Dong, X. M. Li, H. L. Ma and B. H. Sa, Phys. Rev. C **81**, 044914 (2010)

[19] G. Feofilov *et al.* [ALICE Collaboration], PoS Baldin -ISHEPP-XXI (2012) 075.

[20] J. Adam *et al.* [ALICE Collaboration], JHEP **1505**, 097 (2015)

[21] K. Aamodt *et al.* [ALICE Collaboration], JINST **3** (2008) S08002.

[22] B. B. Abelev *et al.* [ALICE Collaboration], Int. J. Mod. Phys. A **29** (2014) 1430044

[23] P. G. Kuijer, Nucl. Phys. A **830**, 81C (2009)

[24] B. Abelev *et al.* [ALICE Collaboration], Phys. Rev. C **88** (2013) 4, 044909

[25] A. Capella and A. Krzywicki, Phys. Rev. D **18**, 4120 (1978).

[26] A. Capella,J. Tran Thanh Van, Phys. Rev. D **29** 11 (1984) 2512

[27] N. Armesto, E. G. Ferreiro, C. Pajares and M. A. Braun,

[28] L. Cunqueiro, E. G. Ferreiro and C. Pajares, PoS CFRNC **2006**, 019 (2006)

[29] Y. V. Kovchegov, E. Levin and L. D. McLerran, Phys. Rev. C **63**, 024903 (2001)

[30] N. Armesto, L. McLerran and C. Pajares, Nucl. Phys. A **781**, 201 (2007)

[31] V. P. Konchakovski, M. Hauer, G. Torrieri, M. I. Gorenstein and E. L. Bratkovskaya, Phys. Rev. C **79**, 034910 (2009)

[32] A. Bzdak, Phys. Rev. C **80**, 024906 (2009)

[33] A. Bialas and K. Zalewski, Nucl. Phys. A **860**, 56 (2011)

[34] A. Bialas and K. Zalewski, Phys. Rev. C **82**, 034911 (2010) Erratum: [Phys. Rev. C **85**, 029903 (2012)]

[35] M. I. Gorenstein and M. Gazdzicki, Phys. Rev. C **84**, 014904 (2011)

[36] M. Gazdzicki, M. I. Gorenstein and M. Mackowiak-Pawlowska, Phys. Rev. C **88**, no. 2, 024907 (2013)

[37] A. Bialas, M. Bleszynski and W. Czyz, Nucl. Phys. B **111**, 461 (1976).

[38] A. Adare *et al.* [PHENIX Collaboration], Phys. Rev. C **78**, 044902 (2008)

[39] C. Alt *et al.* [NA49 Collaboration], Phys. Rev. C **75**, 064904 (2007)

[40] M. Rybczynski and Z. Wlodarczyk, J. Phys. Conf. Ser. **5**, 238 (2005)

[41] V. P. Konchakovski, S. Haussler, M. I. Gorenstein, E. L. Bratkovskaya, M. Bleicher and H. Stoecker, Phys. Rev. C **73**, 034902 (2006)

[42] Broniowski private communication.

[43] B. K. Srivastava [STAR Collaboration], Int. J. Mod. Phys. E **16**, 3371 (2007)

[44] K. Aamodt *et al.* [ALICE Collaboration], Eur. Phys. J. C **68**, 89 (2010)

[45] C. Søgaard *Measurement of Forward-Backward Charged Particle Correlations with ALICE.* Doctoral thesis, Faculty of Science, University of Copenhagen (2012)

[46] Marek Kowalski private communication.

[47] Analysis Note:
https://aliceinfo.cern.ch/Notes/sites/aliceinfo.cern.ch.Notes/files/notes/analysis/akalweit/2013-Nov-27-analysis_note-PrimaryParticle.pdf

[48] V. Kovalenko and V. Vechernin, EPJ Web Conf. **66**, 04015 (2014)

[49] Vitalii Ozvenchuk, private communication.

APPENDIX A

The b_{corr}, ω, Σ expressed in terms of correction factors

The formulas for b_{corr}, scaled variance ω and strongly intensive quantity Σ corrected for total detector correction (superposed corrections for secondaries and total detector efficiency) are rewritten in terms of correction factors for secondaries ($\mathbf{S}_{\widetilde{\langle n_F \rangle}}$,$\mathbf{S}_{\widetilde{\langle n_B \rangle}}$,$\mathbf{S}_{\widetilde{\langle n_F^2 \rangle}}$,...) and for total detector efficiency ($\mathbf{A_F}$, $\mathbf{A_B}$). The designation of the observables is the same as introduced in Section 2.5, i.e. (a) quantities not corrected neither for secondaries nor for detector efficiency are denoted with placing a tilde over the symbol, (b) quantities corrected only for presence of secondary particles are denoted with placing a hat over the their symbol, (c) fully corrected quantities, for both secondaries and detector reduced efficiency, are written without any denotation.

Correlation coeffient

$$
\begin{aligned}
b_{corr} &= \frac{Cov(n_F, n_B)}{\sqrt{Var(n_F)Var(n_B)}} = \qquad (A.1)\\
&= \frac{\frac{1}{A_F A_B}\widehat{Cov(n_F, n_B)}}{\frac{1}{A_F A_B}\sqrt{\left[\widehat{Var(n_F)} - \widehat{\langle n_F \rangle}(1 - A_F)\right]\left[\widehat{Var(n_B)} - \widehat{\langle n_B \rangle}(1 - A_B)\right]}} = \\
&\frac{S_{\widetilde{\langle n_B n_F \rangle}}\widetilde{Cov(n_B n_F)} + \left(S_{\widetilde{\langle n_B n_F \rangle}} - S_{\widetilde{\langle n_B \rangle}} S_{\widetilde{\langle n_F \rangle}}\right)\widetilde{\langle n_B \rangle}\widetilde{\langle n_F \rangle}}{\sqrt{\left[S_{\widetilde{\langle n_F^2 \rangle}}\widetilde{Var(n_F)} + \left(S_{\widetilde{\langle n_F^2 \rangle}} - S^2_{\widetilde{\langle n_F \rangle}}\right)\widetilde{\langle n_F \rangle}^2 - S_{\widetilde{\langle n_F \rangle}}\widetilde{\langle n_F \rangle}(1 - A_F)\right]}} \times \\
&\times \frac{1}{\sqrt{\left[S_{\widetilde{\langle n_B^2 \rangle}}\widetilde{Var(n_B)} + \left(S_{\widetilde{\langle n_B^2 \rangle}} - S^2_{\widetilde{\langle n_B \rangle}}\widetilde{\langle n_B \rangle}^2\right) - S_{\widetilde{\langle n_B \rangle}}\widetilde{\langle n_B \rangle}(1 - A_B)\right]}}
\end{aligned}
$$

Scaled variance ω

$$\omega = \frac{\mathrm{Var(n)}}{\langle \mathrm{n} \rangle} = \frac{\frac{1}{\mathrm{A}^2}\left[\widehat{\mathrm{Var(n)}} - \widehat{\langle \mathrm{n} \rangle}(1-\mathrm{A})\right]}{\frac{1}{\mathrm{A}}\widehat{\langle \mathrm{n} \rangle}} = \tag{A.2}$$

$$= \frac{\frac{1}{\mathrm{A}}\left[\mathrm{S}_{\widetilde{\langle \mathrm{n}^2 \rangle}}\widetilde{\langle \mathrm{n}^2 \rangle} - \mathrm{S}^2_{\widetilde{\langle \mathrm{n} \rangle}}\widetilde{\langle \mathrm{n} \rangle}^2 - \mathrm{S}_{\widetilde{\langle \mathrm{n} \rangle}}\widetilde{\langle \mathrm{n} \rangle}(1-\mathrm{A})\right]}{\mathrm{S}_{\widetilde{\langle \mathrm{n} \rangle}}\widetilde{\langle \mathrm{n} \rangle}} =$$

$$= \frac{\frac{1}{\mathrm{A}}\left[\mathrm{S}_{\widetilde{\langle \mathrm{n}^2 \rangle}}\widetilde{\mathrm{Var(n)}} + (\mathrm{S}_{\widetilde{\langle \mathrm{n}^2 \rangle}} - \mathrm{S}^2_{\widetilde{\langle \mathrm{n} \rangle}})\widetilde{\langle \mathrm{n} \rangle}^2 - \mathrm{S}_{\widetilde{\langle \mathrm{n} \rangle}}\widetilde{\langle \mathrm{n} \rangle}(1-\mathrm{A})\right]}{\mathrm{S}_{\widetilde{\langle \mathrm{n} \rangle}}\widetilde{\langle \mathrm{n} \rangle}}$$

Strongly intensive quantity

For a symmetric collision like Pb+Pb $\omega_\mathrm{F} = \omega_\mathrm{B}$ and $\langle \mathrm{n_F} \rangle = \langle \mathrm{n_B} \rangle$ the strongly intensive quantity Σ is expresed by fomula:

$$\Sigma = \frac{(< \mathrm{n_F} > \omega_\mathrm{B} + < \mathrm{n_B} > \omega_\mathrm{F} - 2\mathrm{Cov(n_B, n_F)})}{< \mathrm{n_B} > + < \mathrm{n_F} >} = \omega_\mathrm{F}(1 - \mathrm{b_{corr}}) = \tag{A.3}$$

$$= \frac{\frac{1}{\mathrm{A_F}}\left[\mathrm{S}_{\widetilde{\langle \mathrm{n}_\mathrm{F}^2 \rangle}}\widetilde{\mathrm{Var(n_F)}} + (\mathrm{S}_{\widetilde{\langle \mathrm{n}_\mathrm{F}^2 \rangle}} - \mathrm{S}^2_{\widetilde{\langle \mathrm{n_F} \rangle}})\widetilde{\langle \mathrm{n_F} \rangle}^2 - \mathrm{S}_{\widetilde{\langle \mathrm{n_F} \rangle}}\widetilde{\langle \mathrm{n_F} \rangle}(1-\mathrm{A_F})\right]}{\mathrm{S}_{\widetilde{\langle \mathrm{n_F} \rangle}}\widetilde{\langle \mathrm{n_F} \rangle}} \times$$

$$\times \left\{1 - \frac{\frac{\mathrm{A_F}}{\mathrm{A_B}}\left[\mathrm{S}_{\widetilde{\langle \mathrm{n_B n_F} \rangle}}\widetilde{\mathrm{Cov(n_B n_F)}} + \left(\mathrm{S}_{\widetilde{\langle \mathrm{n_B n_F} \rangle}} - \mathrm{S}_{\widetilde{\langle \mathrm{n_B} \rangle}}\mathrm{S}_{\widetilde{\langle \mathrm{n_F} \rangle}}\right)\widetilde{\langle \mathrm{n_B} \rangle}\widetilde{\langle \mathrm{n_F} \rangle}\right]}{\left[\mathrm{S}_{\widetilde{\langle \mathrm{n}_\mathrm{F}^2 \rangle}}\widetilde{\mathrm{Var(n_F)}} + (\mathrm{S}_{\widetilde{\langle \mathrm{n}_\mathrm{F}^2 \rangle}} - \mathrm{S}^2_{\widetilde{\langle \mathrm{n_F} \rangle}})\widetilde{\langle \mathrm{n_F} \rangle}^2 - \mathrm{S}_{\widetilde{\langle \mathrm{n_F} \rangle}}\widetilde{\langle \mathrm{n_F} \rangle}(1-\mathrm{A_F})\right]}\right\}$$

APPENDIX B

Statistical errors

The statistical errors were estimated for measured quantities, namely correlation coefficient, scaled variance and intensive quantity sigma, without taking into account the experimental corrections and for the corresponding formulas including both corrections for secondaries and total detector efficiency.

In this thesis statical errors σ of the studied quantities b_{corr}, ω, Σ were estimated as a square root of the variance of the sample quantity: $\sigma_{b_{corr}} = \sqrt{Var(b_{corr})}$, $\sigma_{\omega} = \sqrt{Var(\omega)}$, $\sigma_{\Sigma} = \sqrt{Var(\Sigma)}$.

The estimation of the variances of correlation coefficient, scaled variance and strongly intensive quantity sigma was based on the *delta method*. In the first step a linear approximation of the each measured quantity was obtained by expanding it into first order Taylor-series, then the variance of the resulting simpler linear function was computed.

Example

Let $f(x, y)$ be a function of two random variables x and y. The first-order Taylor series expansion of two variable function $f(x, y)$ around $x = x_0$ and $y = y_0$ is given by:

$$f(x, y) \approx f(x_0, y_0) + \alpha_1(x - x_0) + \alpha_2(y - y_0)$$

. The $\alpha_{i=1,2}$ are the coefficient of Taylor series expansion and equal $\alpha_1 = \frac{\partial f(x,y)}{\partial x}$, $\alpha_2 = \frac{\partial f(x,y)}{\partial y}$ Hence, the variance of $f(x, y)$ can be approximated by following formula:

$$Var(f(x, y)) \approx Var(f(x_0, y_0)+\alpha_1(x-x_0)+\alpha_2(y-y_0)) = \alpha_1^2 Var(x)+\alpha_2^2 Var(y)+2\alpha_1\alpha_2 Cov(x, y)$$

The complete formulas for the variances of each quantity, correlation coefficient, scaled variance and strongly intensive quantity with and without total detector correction are given below.

Estimation of statistical errors for correlation coefficient

Correlation coefficient without total detector correction

The forward-backward correlation coefficient $\widetilde{b_{corr}}$ without corrections is considered as a function of three variables:

$$\widetilde{b_{corr}} = \frac{\widetilde{Cov(n_F, n_B)}}{\sqrt{\widetilde{Var(n_F)}\widetilde{Var(n_B)}}} = f\left(\widetilde{Cov(n_F, n_B)}, \widetilde{Var(n_F)}, \widetilde{Var(n_B)}\right)$$

The variance of $\widetilde{b_{corr}}$ was approximated by following formula:

$$\begin{aligned} Var(\widetilde{b_{corr}}) \approx & \widetilde{\alpha_1}^2 Var(\widetilde{Cov(n_B, n_F)}) + \widetilde{\alpha_2}^2 Var(\widetilde{Var(n_B)}) + \widetilde{\alpha_3}^2 Var(\widetilde{Var(n_F)}) + \\ & 2\widetilde{\alpha_1}\widetilde{\alpha_2} Cov(\widetilde{Cov(n_B, n_F)}, \widetilde{Var(n_B)}) + 2\widetilde{\alpha_1}\widetilde{\alpha_3} Cov(\widetilde{Cov(n_B, n_F)}, \widetilde{Var(n_F)}) + \\ & 2\widetilde{\alpha_2}\widetilde{\alpha_3} Cov(\widetilde{Var(n_B)}, \widetilde{Var(n_F)}) \end{aligned} \tag{B.1}$$

where the $\widetilde{\alpha_{i=1,2,3}}$ are the coefficients of the Taylor series:

$$\widetilde{\alpha_1} = \frac{\partial b_{corr}}{\partial \widetilde{Cov(n_B, n_F)}} = \frac{1}{\sqrt{\widetilde{Var(n_B)}\widetilde{Var(n_F)}}} \tag{B.2}$$

$$\widetilde{\alpha_2} = \frac{\partial b_{corr}}{\partial \widetilde{Var(n_B)}} = \frac{-\widetilde{Cov(n_B, n_F)}}{2\widetilde{Var(n_B)}\sqrt{\widetilde{Var(n_B)}\widetilde{Var(n_F)}}} \tag{B.3}$$

$$\widetilde{\alpha_3} = \frac{\partial b_{corr}}{\partial \widetilde{Var(n_F)}} = \frac{-\widetilde{Cov(n_B, n_F)}}{2\widetilde{Var(n_F)}\sqrt{\widetilde{Var(n_B)}\widetilde{Var(n_F)}}} \tag{B.4}$$

The statistical error for correlation coefficient is estimated as the square root of the variance of the sampling correlation coefficient $\sigma_{\widetilde{b_{corr}}} = \sqrt{\widetilde{Var(b_{corr})}}$, where $\widetilde{Var(b_{corr})}$ was determined by the expression B.1

Correlation coefficient with total detector correction

In order to expand in Taylor series the formula for correlation coefficient with applied total detector correction, the b_{corr} is considered as a function of twelve variables (Eq. A.1):

$$b_{corr} = f\left(\widetilde{Cov(n_F, n_B)}, \widetilde{Var(n_F)}, \widetilde{Var(n_B)}, \widetilde{\langle n_B \rangle}, \widetilde{\langle n_F \rangle}, S_{\widetilde{\langle n_B \rangle}}, S_{\widetilde{\langle n_F \rangle}}, S_{\widetilde{\langle n_B^2 \rangle}}, S_{\widetilde{\langle n_F^2 \rangle}}, S_{\widetilde{\langle n_F n_B \rangle}}, A_F, A_B\right)$$

The Taylor series coefficients $\alpha_{i=1,2,3,\ldots,12}$ are given by following derivatives:

$$\alpha_1 = \frac{\partial b_{corr}}{\partial \widetilde{Cov(n_F, n_B)}} = \frac{S_{\widetilde{\langle n_F n_B \rangle}}}{(\sqrt{Var(n_f)Var(n_B)}A_F A_B)} \tag{B.5}$$

$$\alpha_2 = \frac{\partial b_{corr}}{\partial \widetilde{Var(n_B)}} = -\frac{1}{{A_B}^2}\frac{Cov(n_F, n_B)S_{\widetilde{\langle n_B^2 \rangle}}}{(2Var(n_B)\sqrt{Var(n_f)Var(n_B)})} \tag{B.6}$$

$$\alpha_3 = \frac{\partial b_{corr}}{\partial \widetilde{Var(n_F)}} = -\frac{1}{{A_F}^2}\frac{Cov(n_F, n_B)S_{\widetilde{\langle n_F^2 \rangle}}}{(2Var(n_F)\sqrt{Var(n_f)Var(n_B)})} \tag{B.7}$$

$$\alpha_4 = \frac{\partial b_{corr}}{\partial \widetilde{\langle n_B \rangle}} = \Big\{(S_{\widetilde{\langle n_F n_B \rangle}} - S_{\widetilde{\langle n_B \rangle}}S_{\widetilde{\langle n_F \rangle}})\widetilde{\langle n_F \rangle} - \tag{B.8}$$

$$- \frac{1}{2Var(n_B)}\frac{1}{A_B^2}\big[2(S_{\widetilde{\langle n_B{}^2 \rangle}} - S^2_{\widetilde{\langle n_B \rangle}})\widetilde{\langle n_B \rangle} - (1 - A_B)S_{\widetilde{\langle n_B \rangle}}\big]\widehat{Cov(n_F, n_B)}\Big\}\frac{1}{A_F A_B Var(n_B)Var(n_F)}$$

$$\alpha_5 = \frac{\partial b_{corr}}{\partial \widetilde{\langle n_F \rangle}} = \Big\{(S_{\widetilde{\langle n_F n_B \rangle}} - S_{\widetilde{\langle n_B \rangle}}S_{\widetilde{\langle n_F \rangle}})\widetilde{\langle n_B \rangle} - \tag{B.9}$$

$$- \frac{1}{2Var(n_F)}\frac{1}{A_F^2}\big[2(S_{\widetilde{\langle n_F{}^2 \rangle}} - S^2_{\widetilde{\langle n_F \rangle}})\widetilde{\langle n_F \rangle} - (1 - A_F)S_{\widetilde{\langle n_F \rangle}}\big]\widehat{Cov(n_F, n_B)}\Big\}\frac{1}{A_F A_B Var(n_B)Var(n_F)}$$

$$\alpha_6 = \frac{\partial b_{corr}}{\partial S_{\widetilde{\langle n_B \rangle}}} = \Big\{ - S_{\widetilde{\langle n_F \rangle}}\widetilde{\langle n_B \rangle}\widetilde{\langle n_F \rangle}\sqrt{Var(n_B)Var(n_F)} - \tag{B.10}$$

$$- \frac{\sqrt{Var(n_B)Var(n_F)}}{2Var(n_B)}\frac{1}{A_B^2}\big[- 2S_{\widetilde{\langle n_B \rangle}}\widetilde{\langle n_B \rangle}\widetilde{\langle n_B \rangle} - (1 - A_B)\widetilde{\langle n_B \rangle}\big]\widehat{Cov(n_F, n_B)}\Big\}\frac{1}{A_F A_B Var(n_B)Var(n_F)}$$

$$\alpha_7 = \frac{\partial b_{corr}}{\partial S_{\widetilde{\langle n_F \rangle}}} = \Big\{ - S_{\widetilde{\langle n_B \rangle}}\widetilde{\langle n_B \rangle}\widetilde{\langle n_F \rangle}\sqrt{Var(n_F)Var(n_B)} - \tag{B.11}$$

$$- \frac{\sqrt{Var(n_F)Var(n_B)}}{2Var(n_F)}\frac{1}{A_F^2}\big[- 2S_{\widetilde{\langle n_F \rangle}}\widetilde{\langle n_F \rangle}\widetilde{\langle n_F \rangle} - (1 - A_F)\widetilde{\langle n_F \rangle}\big]\widehat{Cov(n_F, n_B)}\Big\}\frac{1}{A_F A_B Var(n_B)Var(n_F)}$$

$$\alpha_8 = \frac{\partial b_{corr}}{\partial S_{\widetilde{\langle n_B{}^2 \rangle}}} = \frac{-\widehat{Cov(n_F, n_B)}\frac{1}{A_B^2}(\widetilde{Var(n_B)} + \widetilde{\langle n_B \rangle}^2)}{2A_F A_B Var(n_B)\sqrt{Var(n_F)Var(n_B)}} \tag{B.12}$$

$$\alpha_9 = \frac{\partial b_{corr}}{\partial S_{\widetilde{\langle n_F{}^2 \rangle}}} = \frac{-\widehat{Cov(n_F, n_B)}\frac{1}{A_F^2}(\widetilde{Var(n_F)} + \widetilde{\langle n_F \rangle}^2)}{2A_F A_B Var(n_F)\sqrt{Var(n_F)Var(n_B)}} \tag{B.13}$$

$$\alpha_{10} = \frac{\partial b_{corr}}{\partial S_{\widetilde{\langle n_B n_F \rangle}}} = \frac{\widetilde{Cov(n_F, n_B)} + \widetilde{\langle n_F \rangle}\widetilde{\langle n_B \rangle}}{A_F A_B\sqrt{Var(n_F)Var(n_B)}} \tag{B.14}$$

$$\alpha_{11} = \frac{\partial b_{corr}}{\partial A_B} = \frac{-(\widehat{Cov(n_F, n_B)}\widehat{\langle n_B \rangle}S_{\widetilde{\langle n_B \rangle}})}{2A_F A_B^3 Var(n_B)\sqrt{Var(n_F)Var(n_B)}} \tag{B.15}$$

$$\alpha_{12} = \frac{\partial b_{corr}}{\partial A_F} = \frac{-(\widehat{Cov(n_F, n_B)}\widehat{\langle n_F \rangle}S_{\widetilde{\langle n_F \rangle}})}{2A_B A_F^3 Var(n_F)\sqrt{Var(n_F)Var(n_B)}} \tag{B.16}$$

For correlation coefficient including full detector correction:

$$\begin{aligned}
&\mathrm{Var}(b_{corr}) \approx \alpha_1^2\mathrm{Var}(\mathrm{Cov}(\widetilde{n_F}, n_B)) + \alpha_2^2\mathrm{Var}(\widetilde{\mathrm{Var}(n_B)}) + \alpha_3^2\mathrm{Var}(\widetilde{\mathrm{Var}(n_F)}) + \alpha_4^2\mathrm{Var}(\widetilde{\langle n_B\rangle})+\\
&\alpha_5^2\mathrm{Var}(\widetilde{\langle n_F\rangle}) + \alpha_6^2\mathrm{Var}(S_{\widetilde{n_B}}) + \alpha_7^2\mathrm{Var}(S_{\widetilde{n_F}}) + \alpha_8^2\mathrm{Var}(S_{\widetilde{n_B{}^2}}) + \alpha_9^2\mathrm{Var}(S_{\widetilde{n_F{}^2}}) + \alpha_{10}^2\mathrm{Var}(S_{\widetilde{n_{BF}}})+\\
&\alpha_{11}^2\mathrm{Var}(A_B) + \alpha_{12}^2\mathrm{Var}(A_F) + 2\alpha_1\alpha_2\mathrm{Cov}(\mathrm{Cov}(\widetilde{n_F}, n_B), \widetilde{\mathrm{Var}(n_B)})+\\
&2\alpha_1\alpha_3\mathrm{Cov}(\mathrm{Cov}(\widetilde{n_F}, n_B), \widetilde{\mathrm{Var}(n_F)}) + 2\alpha_1\alpha_4\mathrm{Cov}(\widetilde{\langle n_B\rangle}, \mathrm{Cov}(n_F, n_B))+\\
&2\alpha_1\alpha_5\mathrm{Cov}(\widetilde{\langle n_F\rangle}, \mathrm{Cov}(n_F, n_B)) + 2\alpha_2\alpha_3\mathrm{Cov}(\widetilde{\mathrm{Var}(n_B)}, \widetilde{\mathrm{Var}(n_F)})+\\
&2\alpha_2\alpha_4\mathrm{Cov}(\widetilde{\langle n_B\rangle}, \widetilde{\mathrm{Var}(n_F)}) + 2\alpha_2\alpha_5\mathrm{Cov}(\widetilde{\langle n_F\rangle}, \widetilde{\mathrm{Var}(n_B)}) + 2\alpha_3\alpha_4\mathrm{Cov}(\widetilde{\langle n_B\rangle}, \widetilde{\mathrm{Var}(n_F)})+\\
&2\alpha_3\alpha_5\mathrm{Cov}(\widetilde{\langle n_F\rangle}, \widetilde{\mathrm{Var}(n_F)}) + 2\alpha_4\alpha_5\mathrm{Cov}(\widetilde{\langle n_F\rangle}, \widetilde{\langle n_B\rangle}) + 2\alpha_6\alpha_7\mathrm{Cov}(S_{\widetilde{\langle n_B\rangle}}, S_{\widetilde{\langle n_F\rangle}})+\\
&2\alpha_6\alpha_8\mathrm{Cov}(S_{\widetilde{\langle n_B\rangle}}, S_{\widetilde{\langle n_B^2\rangle}}) + 2\alpha_6\alpha_9\mathrm{Cov}(S_{\widetilde{\langle n_B\rangle}}, S_{\widetilde{\langle n_F^2\rangle}}) + 2\alpha_6\alpha_{10}\mathrm{Cov}(S_{\widetilde{\langle n_B\rangle}}, S_{\widetilde{\langle n_Fn_B\rangle}})+\\
&2\alpha_6\alpha_{11}\mathrm{Cov}(A_B, S_{\widetilde{\langle n_B\rangle}}) + 2\alpha_6\alpha_{12}\mathrm{Cov}(A_F, S_{\widetilde{\langle n_B\rangle}}) + 2\alpha_7\alpha_8\mathrm{Cov}(S_{\widetilde{\langle n_F\rangle}}, S_{\widetilde{\langle n_B^2\rangle}})+\\
&2\alpha_7\alpha_9\mathrm{Cov}(S_{\widetilde{\langle n_F\rangle}}, S_{\widetilde{\langle n_F^2\rangle}}) + 2\alpha_7\alpha_{10}\mathrm{Cov}(S_{\widetilde{\langle n_F\rangle}}, S_{\widetilde{\langle n_Fn_B\rangle}}) + 2\alpha_7\alpha_{11}\mathrm{Cov}(A_B, S_{\widetilde{\langle n_F\rangle}})+\\
&2\alpha_7\alpha_{12}\mathrm{Cov}(A_F, S_{\widetilde{\langle n_F\rangle}}) + 2\alpha_8\alpha_9\mathrm{Cov}(S_{\widetilde{\langle n_B^2\rangle}}, S_{\widetilde{\langle n_F^2\rangle}}) + 2\alpha_8\alpha_{10}\mathrm{Cov}(S_{\widetilde{\langle n_B^2\rangle}}, S_{\widetilde{\langle n_Fn_B\rangle}})+\\
&2\alpha_8\alpha_{11}\mathrm{Cov}(A_B, S_{\widetilde{\langle n_B^2\rangle}}) + 2\alpha_8\alpha_{12}\mathrm{Cov}(A_F, S_{\widetilde{\langle n_B^2\rangle}}) + 2\alpha_9\alpha_{10}\mathrm{Cov}(S_{\widetilde{\langle n_F^2\rangle}}, S_{\widetilde{\langle n_Fn_B\rangle}})+\\
&2\alpha_9\alpha_{11}\mathrm{Cov}(A_B, S_{\widetilde{\langle n_F^2\rangle}}) + 2\alpha_9\alpha_{12}\mathrm{Cov}(A_F, S_{\widetilde{\langle n_F^2\rangle}}) + 2\alpha_{10}\alpha_{11}\mathrm{Cov}(A_B, S_{\widetilde{\langle n_Fn_B\rangle}})+\\
&2\alpha_{10}\alpha_{12}\mathrm{Cov}(A_F, S_{\widetilde{\langle n_Fn_B\rangle}}) + 2\alpha_{11}\alpha_{12}\mathrm{Cov}(A_B, A_F) \qquad \text{(B.17)}
\end{aligned}$$

For the correlation coefficient corrected for total detector effects (for secondaries and total detector efficiency) the statistical error was estimated as $\sigma_{b_{corr}} = \sqrt{\mathrm{Var}(b_{corr})}$, where $\mathrm{Var}(b_{corr})$ was determined by the expression B.17.

Estimation of statistical error of scaled variance ω

Scaled variance $\widetilde{\omega}$ without total detector correction

The scaled variance $\widetilde{\omega}$ without corrections is a function of two variables:

$$\widetilde{\omega} = f(\widetilde{\mathrm{Var}(n)}, \widetilde{\langle n\rangle})$$

The variance of $\widetilde{\omega}$ was approximated by formula:

$$\mathrm{Var}(\widetilde{\omega}) \approx \widetilde{\beta_1}^2\mathrm{Var}(\widetilde{\langle n\rangle}) + \widetilde{\beta_2}^2\mathrm{Var}(\widetilde{\mathrm{Var}(n)}) + 2\widetilde{\beta_1}\widetilde{\beta_2}\mathrm{Cov}(\widetilde{\langle n\rangle}, \widetilde{\mathrm{Var}(n)}); \qquad \text{(B.18)}$$

where the $\widetilde{\beta_{i=1,2}}$ are the coefficients of Taylor series expansion:

$$\widetilde{\beta_1} = \frac{\partial\widetilde{\omega}}{\partial\widetilde{\langle n\rangle}} = \frac{-\widetilde{\mathrm{Var}(n)}}{\widetilde{\langle n\rangle}^2} \qquad \text{(B.19)}$$

$$\widetilde{\beta_2} = \frac{\partial\widetilde{\omega}}{\partial\widetilde{\mathrm{Var}(n)}} = \frac{1}{\widetilde{\langle n\rangle}} \qquad \text{(B.20)}$$

The statistical error of scaled variance $\widetilde{\omega}$ without corrections for secondaries and total detector efficiency was estimated as $\sigma_{\widetilde{\omega}} = \sqrt{\mathrm{Var}(\widetilde{\omega})}$, where $\mathrm{Var}(\widetilde{\omega})$ was determined from the formula B.18.

Scaled variance ω with total detector correction

The scaled variance ω with applied total detector correction is a function of five variables (Eq. A.2):

$$\omega = f(\widetilde{\mathrm{Var}(n)}, \widetilde{\langle n\rangle}, A, S_{\widetilde{\langle n^2\rangle}}, S_{\widetilde{\langle n\rangle}})$$

Variance of the scaled variance (ω) of multiplicity distribution is given by:

$$\begin{aligned}\mathrm{Var}(\omega) = {} & \beta_1^2\mathrm{Var}(\widetilde{\mathrm{Var}(n)}) + \beta_2^2\mathrm{Var}(\widetilde{n}) + \beta_3^2\mathrm{Var}(A) + \beta_4^2\mathrm{Var}(S_{\widetilde{\langle n^2\rangle}}) + \\ & \beta_5^2\mathrm{Var}(S_{\widetilde{\langle n\rangle}}) + 2\beta_1\beta_2\mathrm{Cov}(\widetilde{\mathrm{Var}(n)}, \widetilde{\langle n\rangle}) + 2\beta_3\beta_4\mathrm{Cov}(A, \widetilde{\langle n^2\rangle}) + 2\beta_3\beta_5\mathrm{Cov}(A, \widetilde{\langle n\rangle}) + \\ & 2\beta_4\beta_5\mathrm{Cov}(\widetilde{\langle n\rangle}, \widetilde{\langle n^2\rangle})\end{aligned} \tag{B.21}$$

where $\beta_{i=1,2,3,\ldots,5}$ are the following Taylor series coefficients:

$$\beta_1 = \frac{\partial\omega}{\partial\widetilde{\mathrm{Var}(n)}} = \frac{1}{A}\frac{S_{\widetilde{\langle n^2\rangle}}}{S_{\widetilde{\langle n\rangle}}\langle n\rangle} \tag{B.22}$$

$$\beta_2 = \frac{\partial\omega}{\partial\widetilde{\langle n\rangle}} = \frac{1}{A}\left[(-1)\frac{S_{\widetilde{\langle n^2\rangle}}}{S_{\widetilde{\langle n\rangle}}}\frac{\mathrm{Var}(n)}{\langle n\rangle^2} + \frac{(S_{\widetilde{\langle n^2\rangle}} - S^2_{\widetilde{\langle n\rangle}})}{S_{\widetilde{\langle n\rangle}}}\right] \tag{B.23}$$

$$\beta_3 = \frac{\partial\omega}{\partial A} = -\frac{1}{A^2}\frac{\left[S_{\widetilde{\langle n^2\rangle}}\mathrm{Var}(n) + (S_{\widetilde{\langle n^2\rangle}} - S^2_{\widetilde{\langle n\rangle}})\langle n\rangle^2\right]}{S_{\widetilde{\langle n\rangle}}\langle n\rangle} + \frac{1}{A^2} \tag{B.24}$$

$$\beta_4 = \frac{\partial\omega}{\partial S_{\widetilde{\langle n^2\rangle}}} = \frac{1}{A}\left(\frac{\mathrm{Var}(n)}{S_{\widetilde{\langle n\rangle}}\langle n\rangle} + \frac{\langle n\rangle}{S_{\widetilde{\langle n\rangle}}}\right) \tag{B.25}$$

$$\beta_5 = \frac{\partial\omega}{\partial S_{\widetilde{\langle n\rangle}}} = \frac{1}{A}\left(-\frac{S_{\widetilde{\langle n^2\rangle}}}{S^2_{\widetilde{\langle n\rangle}}}\frac{\mathrm{Var}(n)}{\langle n\rangle} - \frac{S_{\widetilde{\langle n^2\rangle}}}{S^2_{\widetilde{\langle n\rangle}}\langle n\rangle} - \langle n\rangle\right) \tag{B.26}$$

The statistical error of scaled variance ω was estimated as $\sigma_\omega = \sqrt{\mathrm{Var}(\omega)}$, where $\mathrm{Var}(\omega)$ was determined from the formula B.21.

Estimation of statistical error of strongly intensive quantity Σ

Strongly intensive quantity $\widetilde{\Sigma}$ without total detector correction

For the symmetric Pb+Pb collision the strongly intensive quantity $\widetilde{\Sigma}$ can be considered as a function of three variables:

$$\widetilde{\Sigma} = \widetilde{\omega_F}(1 - \widetilde{b_{corr}}) = \frac{\widetilde{\mathrm{Var}(n_F)}}{\widetilde{\langle n_F\rangle}}\left[1 - \frac{\widetilde{\mathrm{Cov}(n_F, n_B)}}{\widetilde{\mathrm{Var}(n_F)}}\right] = f(\widetilde{\mathrm{Cov}(n_F, n_B)}, \widetilde{\mathrm{Var}(n_F)}, \widetilde{\langle n_F\rangle})$$

The variance of strongly intensive quantity $\widetilde{\Sigma}$ is given by:

$$\begin{aligned}\mathrm{Var}(\widetilde{\Sigma}) = {\widetilde{\gamma_1}}^2\mathrm{Var}(\widetilde{\mathrm{Var}(\mathrm{n_F})}) + {\widetilde{\gamma_2}}^2\mathrm{Var}(\widetilde{\mathrm{Cov}(\mathrm{n_F},\mathrm{n_B})}) + {\widetilde{\gamma_3}}^2\mathrm{Var}(\widetilde{\langle \mathrm{n_F}\rangle})+ \\ + 2\widetilde{\gamma_1}\widetilde{\gamma_2}\mathrm{Cov}(\widetilde{\mathrm{Cov}(\mathrm{n_F},\mathrm{n_B})},\widetilde{\mathrm{Var}(\mathrm{n_F})}) + 2\widetilde{\gamma_1}\widetilde{\gamma_3}\mathrm{Cov}(\widetilde{\langle \mathrm{n_F}\rangle},\widetilde{\mathrm{Var}(\mathrm{n_F})})+ \\ + 2\widetilde{\gamma_2}\widetilde{\gamma_3}\mathrm{Cov}(\widetilde{\langle \mathrm{n_F}\rangle},\mathrm{Cov}(\mathrm{n_F},\mathrm{n_B}));\end{aligned} \tag{B.27}$$

The $\widetilde{\gamma_{i=1,2,3}}$ are the Taylor series coefficients defined by following expressions:

$$\widetilde{\gamma_1} = \frac{\partial\widetilde{\Sigma}}{\partial\widetilde{\mathrm{Var}(\mathrm{n_F})}} = \frac{1}{\widetilde{\langle \mathrm{n_F}\rangle}} \tag{B.28}$$

$$\widetilde{\gamma_2} = \frac{\partial\widetilde{\Sigma}}{\partial\widetilde{\mathrm{Cov}(\mathrm{n_F},\mathrm{n_B})}} = -\frac{1}{\widetilde{\langle \mathrm{n_F}\rangle}} \tag{B.29}$$

$$\widetilde{\gamma_3} = \frac{\partial\widetilde{\Sigma}}{\partial\widetilde{\langle \mathrm{n_F}\rangle}} = \frac{\widetilde{\mathrm{Cov}(\mathrm{n_F},\mathrm{n_B})} - \widetilde{\mathrm{Var}(\mathrm{n_F})}}{{\widetilde{\langle \mathrm{n_F}\rangle}}^2} \tag{B.30}$$

The statistical error of the strongly intensive quantity $\widetilde{\Sigma}$ was estimated as $\sigma_{\widetilde{\Sigma}} = \sqrt{\mathrm{Var}(\widetilde{\Sigma})}$.

Strongly intensive quantity $\widetilde{\Sigma}$ with total detector correction

Strongly intensive quantity Σ corrected for secondaries and total detector efficiency (total detector correction), for a symmetric Pb+Pb collision due to Eq. A.3 is a function of ten variables, namely:

$$\Sigma = f(\widetilde{\mathrm{Var}(\mathrm{n})},\widetilde{\mathrm{Cov}(\mathrm{n_F},\mathrm{n_B})},\widetilde{\langle \mathrm{n_F}\rangle},\widetilde{\langle \mathrm{n_B}\rangle},\mathrm{A_F},\mathrm{A_B},\mathrm{S}_{\widetilde{\langle \mathrm{n_F^2}\rangle}},\mathrm{S}_{\widetilde{\langle \mathrm{n_F n_B}\rangle}},\mathrm{S}_{\widetilde{\langle \mathrm{n_F}\rangle}},\mathrm{S}_{\widetilde{\langle \mathrm{n_B}\rangle}})$$

Hence, the variance of Σ is given by:

$$\begin{aligned}&\mathrm{Var}(\Sigma) \approx \gamma_1^2\mathrm{Var}(\mathrm{Var}(\mathrm{n_F})) + \gamma_2^2\mathrm{Var}(\mathrm{Cov}(\mathrm{n_F},\mathrm{n_B})) + \gamma_3^2\mathrm{Var}(\langle \mathrm{n_F}\rangle) + \gamma_4^2\mathrm{Var}(\langle \mathrm{n_B}\rangle)+ \\ &\gamma_5^2\mathrm{Var}(\mathrm{A_F}) + \gamma_6^2\mathrm{Var}(\mathrm{A_B}) + \gamma_7^2\mathrm{Var}(\mathrm{S}_{\widetilde{\langle \mathrm{n_F^2}\rangle}}) + \gamma_8^2\mathrm{Var}(\mathrm{S}_{\widetilde{\langle \mathrm{n_F n_B}\rangle}}) + \gamma_9^2\mathrm{Var}(\mathrm{S}_{\widetilde{\langle \mathrm{n_F}\rangle}}) + \gamma_{10}^2\mathrm{Var}(\mathrm{S}_{\widetilde{\langle \mathrm{n_B}\rangle}})+ \\ &2\gamma_1\gamma_2\mathrm{Cov}(\mathrm{Cov}(\mathrm{n_F},\mathrm{n_B}),\mathrm{Var}(\mathrm{n_F})) + 2\gamma_1\gamma_3\mathrm{Cov}(\mathrm{Var}(\mathrm{n_F}),\langle \mathrm{n_F}\rangle) + 2\gamma_1\gamma_4\mathrm{Cov}(\mathrm{Var}(\mathrm{n_F}),\langle \mathrm{n_B}\rangle)+ \\ &2\gamma_2\gamma_3\mathrm{Cov}(\mathrm{Cov}(\mathrm{n_F},\mathrm{n_B}),\langle \mathrm{n_F}\rangle) + 2\gamma_2\gamma_4\mathrm{Cov}(\mathrm{Cov}(\mathrm{n_F},\mathrm{n_B}),\langle \mathrm{n_B}\rangle) + 2\gamma_3\gamma_4\mathrm{Cov}(\langle \mathrm{n_B}\rangle,\langle \mathrm{n_F}\rangle)+ \\ &2\gamma_5\gamma_6\mathrm{Cov}(\mathrm{A_F},\mathrm{A_B}) + 2\gamma_5\gamma_7\mathrm{Cov}(\mathrm{A_F},\mathrm{S}_{\widetilde{\langle \mathrm{n_F^2}\rangle}}) + 2\gamma_5\gamma_8\mathrm{Cov}(\mathrm{A_F},\mathrm{S}_{\widetilde{\langle \mathrm{n_F n_B}\rangle}}) + 2\gamma_5\gamma_9\mathrm{Cov}(\mathrm{A_F},\mathrm{S}_{\widetilde{\langle \mathrm{n_F}\rangle}})+ \\ &2\gamma_5\gamma_{10}\mathrm{Cov}(\mathrm{A_F},\mathrm{S}_{\widetilde{\langle \mathrm{n_B}\rangle}}) + 2\gamma_6\gamma_7\mathrm{Cov}(\mathrm{A_B},\mathrm{S}_{\widetilde{\langle \mathrm{n_B^2}\rangle}}) + 2\gamma_6\gamma_8\mathrm{Cov}(\mathrm{A_B},\mathrm{S}_{\widetilde{\langle \mathrm{n_F n_B}\rangle}}) + 2\gamma_6\gamma_9\mathrm{Cov}(\mathrm{A_B},\mathrm{S}_{\widetilde{\langle \mathrm{n_F}\rangle}})+ \\ &2\gamma_6\gamma_{10}\mathrm{Cov}(\mathrm{A_B},\mathrm{S}_{\widetilde{\langle \mathrm{n_B}\rangle}}) + 2\gamma_7\gamma_8\mathrm{Cov}(\mathrm{S}_{\widetilde{\langle \mathrm{n_F^2}\rangle}},\mathrm{S}_{\widetilde{\langle \mathrm{n_F n_B}\rangle}}) + 2\gamma_7\gamma_9\mathrm{Cov}(\mathrm{S}_{\widetilde{\langle \mathrm{n_F^2}\rangle}},\mathrm{S}_{\widetilde{\langle \mathrm{n_F}\rangle}})+ \\ &2\gamma_7\gamma_{10}\mathrm{Cov}(\mathrm{S}_{\widetilde{\langle \mathrm{n_F^2}\rangle}},\mathrm{S}_{\widetilde{\langle \mathrm{n_B}\rangle}}) + 2\gamma_8\gamma_9\mathrm{Cov}(\mathrm{S}_{\widetilde{\langle \mathrm{n_B n_F}\rangle}},\mathrm{S}_{\widetilde{\langle \mathrm{n_F}\rangle}}) + 2\gamma_8\gamma_{10}\mathrm{Cov}(\mathrm{S}_{\widetilde{\langle \mathrm{n_B n_F}\rangle}},\mathrm{S}_{\widetilde{\langle \mathrm{n_B}\rangle}})+ \\ &2\gamma_9\gamma_{10}\mathrm{Cov}(\mathrm{S}_{\widetilde{\langle \mathrm{n_B}\rangle}},\mathrm{S}_{\widetilde{\langle \mathrm{n_F}\rangle}})\end{aligned} \tag{B.31}$$

The $\gamma_{i=1,2,3,\ldots,10}$ are the Taylor series coefficients defined as:

$$\gamma_1 = \frac{\partial\Sigma}{\partial\widetilde{\mathrm{Var}(n)}} = \frac{S_{\widetilde{\langle n_F^2\rangle}}}{(A_F S_{\widetilde{\langle n_F\rangle}}\langle n_F\rangle)} \tag{B.32}$$

$$\gamma_2 = \frac{\partial\Sigma}{\partial\widetilde{\mathrm{Cov}(n_F, n_B)}} = (-1)\frac{S_{\widetilde{\langle n_F n_B\rangle}}}{(A_B S_{\widetilde{\langle n_F\rangle}}\langle n_F\rangle)} \tag{B.33}$$

$$\gamma_3 = \frac{\partial\Sigma}{\partial\widetilde{\langle n_F\rangle}} = \frac{1}{(S_{\widetilde{\langle n_F\rangle}}\langle n_F\rangle^2)}\left(\frac{(S_{\widetilde{\langle n_F n_B\rangle}}\widetilde{\mathrm{Cov}(n_F, n_B)}}{A_B} - \frac{S_{\widetilde{\langle n_F^2\rangle}}\widetilde{\mathrm{Var}(n_F)}}{A_F}\right) + \frac{(S_{\widetilde{\langle n_F^2\rangle}} - S^2_{\widetilde{\langle n_F\rangle}})}{(A_F S_{\widetilde{\langle n_F\rangle}})} \tag{B.34}$$

$$\gamma_4 = \frac{\partial\Sigma}{\partial\widetilde{\langle n_B\rangle}} = \frac{-1}{A_B}\frac{(S_{\widetilde{\langle n_F n_B\rangle}} - S_{\widetilde{\langle n_F\rangle}}S_{\widetilde{\langle n_B\rangle}})}{S_{\widetilde{\langle n_F\rangle}}}$$

$$\gamma_5 = \frac{\partial\Sigma}{\partial A_F} = (-1)\frac{S_{\widetilde{\langle n_F^2\rangle}}\widetilde{\mathrm{Var}(n_F)}}{A_F^2\langle n_F\rangle S_{\widetilde{\langle n_F\rangle}}} - \frac{(S_{\widetilde{\langle n_F^2\rangle}} - S^2_{\widetilde{\langle n_F\rangle}})\langle n_F\rangle}{A_F^2 S_{\widetilde{\langle n_F\rangle}}} + \frac{1}{A_F^2} \tag{B.35}$$

$$\gamma_6 = \frac{\partial\Sigma}{\partial A_B} = \frac{1}{A_B^2}\frac{S_{\widetilde{\langle n_F n_B\rangle}}\widetilde{\mathrm{Cov}(n_F, n_B)} + (S_{\widetilde{\langle n_F n_B\rangle}} - S_{\widetilde{\langle n_B\rangle}}S_{\widetilde{\langle n_F\rangle}})\langle n_F\rangle\langle n_B\rangle}{S_{\widetilde{\langle n_F\rangle}}\langle n_F\rangle} \tag{B.36}$$

$$\gamma_7 = \frac{\partial\Sigma}{\partial S_{\widetilde{\langle n_F^2\rangle}}} = \frac{1}{(A_F S_{\widetilde{\langle n_F\rangle}}\langle n_F\rangle)}(\widetilde{\mathrm{Var}(n_F)} + \langle n_F\rangle^2) \tag{B.37}$$

$$\gamma_8 = \frac{\partial\Sigma}{\partial S_{\widetilde{\langle n_F n_B\rangle}}} = \frac{-1}{(A_B S_{\widetilde{\langle n_F\rangle}}\langle n_F\rangle)}(\widetilde{\mathrm{Cov}(n_F, n_B)} + \langle n_F\rangle^2) \tag{B.38}$$

$$\gamma_9 = \frac{\partial\Sigma}{\partial S_{\widetilde{\langle n_F\rangle}}} = -\frac{(S_{\widetilde{\langle n_F^2\rangle}}\widetilde{\mathrm{Var}(n_F)})}{(S^2_{\widetilde{\langle n_F\rangle}}A_F\langle n_F\rangle)} - \frac{(S_{\widetilde{\langle n_F^2\rangle}} - S^2_{\widetilde{\langle n_F\rangle}})\langle n_F\rangle}{(A_F S^2_{\widetilde{\langle n_F\rangle}})} + \frac{(S_{\widetilde{\langle n_F n_B\rangle}}\widetilde{\mathrm{Cov}(n_F, n_B)})}{(S^2_{\widetilde{\langle n_F\rangle}}A_B\langle n_F\rangle)} - \tag{B.39}$$
$$\frac{(S_{\widetilde{\langle n_F n_B\rangle}} - S_{\widetilde{\langle n_B\rangle}}S_{\widetilde{\langle n_F\rangle}})\langle n_B\rangle}{A_B S^2_{\widetilde{\langle n_F\rangle}}} - \frac{2\langle n_F\rangle}{A_F} + \frac{S_{\widetilde{\langle n_B\rangle}}\langle n_B\rangle}{A_B S_{\widetilde{\langle n_F\rangle}}}$$

$$\gamma_{10} = \frac{\partial\Sigma}{\partial S_{\widetilde{\langle n_B\rangle}}} = \frac{\langle n_B\rangle}{A_B} \tag{B.40}$$

The statistical error of Σ was defined as a square root of variance of this strongly intensive quantity (Eq. B.31), namely $\sigma_\Sigma = \sqrt{\mathrm{Var}(\Sigma)}$.